Understanding subaqueous landslides and their morphology: From qualitative to quantitative analysis

DISSERTATION

zur Erlangung des Doktorgrades

an der Mathematisch-Naturwissenschaftlichen Fakultät

der Christian-Albrechts-Universität zu Kiel

vorgelegt von

Rachel Siân Barrett

Kiel, 2020

Erster Gutachter: Prof. Dr. Sebastian Krastel-Gudegast

Zweiter Gutachter: Prof. Dr. Christian Berndt

Tag der mündlichen Prüfung: 10.11.2020

Zum Druck genehmigt: 10.11.2020

.....

Der Dekan

Hiermit erkläre ich, dass ich die vorliegende Dissertation selbständig, abgesehen von der Beratung durch die Betreuer, und nur mit den angegebenen Hilfsmitteln angefertigt habe. Weder diese noch eine ähnliche Arbeit wurde und wird an anderer Stelle im Rahmen eines Prüfungsverfahrens vorgestellt. Teile der Arbeit wurden bereits als Manuskripte in internationalen Fachzeitschriften veröffentlicht oder zur Veröffentlichung eingereicht. Die Details dazu befinden sich auf der Titelseite der einzelnen Kapitel. Die Arbeit ist unter Einhaltung der Regeln guter wissenschaftlicher Praxis der Deutschen Forschungsgemeinschaft entstanden. Des Weiteren wurde mir kein akademischer Grad entzogen.

Kiel, den 07.10.2020

Rachel Barrett

Abstract

Subaqueous landslides are globally widespread – occurring on continental margins, in lakes, fjords and river deltas, and at volcanic islands – and can destroy critical seafloor infrastructure and marine habitats. Furthermore, they can result in tsunami waves that can have a devastating impact on coastal communities and infrastructure, can transport organic material and pollutants into the deep sea, impact upon hydrocarbon systems, and play a role in defining national economic boundaries. Thus, understanding how subaqueous landslides are emplaced and their potential impact is important both from a hazard mitigation and an economic perspective. The morphology and geometry of a landslide deposit provides key information about how it was emplaced, but our understanding of these factors depends heavily on data coverage and resolution. This thesis makes use of a variety of types of data from different settings and of different resolutions in order to both qualitatively and quantitatively investigate the morphology of mass transport deposits. In particular, I explore the relationship between morphology and the process of emplacement. Some morphological features, such as elongated ridges related to lateral-margin compression, toe compression, and extension (spreading), form through entirely different processes, but appear to have similar geomorphology. As geomorphology is widely used to infer information about the formative process, it is important that it is correctly interpreted. This poses a particular problem in areas of low data coverage, or for very large landslides, which may have failed in multiple stages. Here, we develop and test a quantitative method for distinguishing between different types of ridges in subaqueous landslide deposits. Our results demonstrate a quantitative link between the morphology and formative processes responsible for spreading, toe-compression, and lateral-margin compressional ridges. The application of quantitative methodology such as this represents an important step towards reducing the subjectivity that is often inherent in the analysis of subaqueous landslide deposits. Furthermore, the morphology and emplacement of two end-member cases – a volcanic flank-collapse (the Monte Amarelo flank-collapse of the island of Fogo in the Cape Verdes), and a submarine megaslide on a passive continental margin (the Tampen Slide, offshore Norway) – are examined in detail. The Monte Amarelo flank-collapse deposits offshore Fogo are investigated using a combination of high-resolution sub-bottom profiles, sediment gravity cores, and bathymetric data. These data reveal that the lateral extent of the Monte Amarelo debris avalanche deposits is more than twice what it was previously thought to be. Moreover, we find that the deposition of the debris avalanche deposits triggered the multi-phase failure

of pre-existing seafloor sediments – similar to what has been documented for flank-collapses in the Lesser Antilles (Caribbean). We also find evidence for numerous small volume, previously unobserved, mass transport deposits on the submerged slopes south of the island of Fogo. The second end-member case, the buried Tampen Slide offshore Norway, is investigated using laterally extensive, high-resolution 3D seismic data. We find that the prodigious volume of the Tampen Slide (>1,000 km^3) is largely the result of a single failure along a single glide plane. This differs significantly from other megaslides, whose large total volumes seem to be the result of numerous small volume retrogressive failures, and has important implications for our understanding of how large landslides may fail. Furthermore, the high resolution of the data enables the morphology of the Tampen Slide to be investigated in detail, and we identify regions of spreading and compression (cross-slope ridges), as well as longitudinal (down-slope orientated) chutes and ridges that are >40 m higher than the surrounding deposits – the first time that longitudinal ridges of this scale have been identified in a deep marine setting. The findings for both these end-member subaqueous landslides have important implications for understanding how other such landslides may be emplaced, as well as their corresponding hazards.

Zusammenfassung

Subaquatische Hangrutschungen sind global weit verbreitet – sie treten an Kontinentalrändern, in Seen, Fjorden und Flussdeltas sowie auf vulkanischen Inseln auf – und können wichtige Infrastrukturen am Meeresboden, marine Ökosysteme und Habitate zerstören. Darüber hinaus können sie Tsunamis auslösen, die verheerende Auswirkungen auf Küstenregionen und Infrastruktur haben, organisches Material und Schadstoffe in die Tiefsee transportieren, sich auf Kohlenwasserstoffsysteme auswirken und bei der Festlegung nationaler Grenzen und wirtschaftlicher Zonen eine Rolle spielen können. Daher ist das Verständnis von Mechanismen dieser subaquatischer Hangrutschungen und ihrer potenziellen Auswirkungen, sowohl aus der Sicht der Gefahrenminderung, als auch aus wirtschaftlicher Sicht, essentiell. Die Morphologie und Geometrie einer Hangrutschung liefert wichtige Informationen darüber, wie diese abgelagert wurde. Jedoch hängt die Analyse dieser Faktoren stark von der Art der Datenaufnahme und -auflösung ab. Um die Morphologie von Massentransportablagerungen sowohl qualitativ als auch quantitativ zu untersuchen, wird in dieser Arbeit eine Vielzahl von Datentypen aus unterschiedlichen Regionen und unterschiedlicher Auflösungen verwendet. In dieser Arbeit werden insbesondere die Beziehungen zwischen Morphologie und deren zugrunde liegenden Prozesse untersucht. Strukturen ähnlicher Ausprägung können durch ganz unterschiedliche Prozesse entstehen. Ein gutes Beispiel dafür sind Kämme, die als Folge von Dehnung (Spreizung) im proximalen Bereich, Kompression im distalen Bereich, oder durch laterale Randkompressionen entstehen können. Da die Geomorphologie weithin zur Ableitung von Informationen über den Entstehungsprozess verwendet wird, ist es wichtig, dass diese korrekt interpretiert wird. Dies stellt ein besonderes Problem in Gebieten mit geringer Datendichte oder bei sehr großen Hangrutschungen dar, die möglicherweise in mehreren Phasen abgerutscht sind. Hier werden quantitative Methoden zur Differenzierung zwischen lateraler Randkompression, distaler Ridge Kompression und Dehnungskämmen in Ablagerungen von subaquatischer Hangrutschungen untersucht und getestet. Die Ergebnisse dieser Analyse zeigen einen quantitativen Zusammenhang zwischen der Morphologie und den Formgebungsprozessen, die für die Spreizung, die distale Kompressions-Kämme und die Kompression der seitlichen Ränder verantwortlich sind. Die Anwendung einer solchen quantitativen Methodik stellt einen wichtigen Schritt zur Verringerung der Subjektivität dar, die der Analyse subaquatischer Hangrutschablagerungen oft innewohnt. Darüber hinaus wird die Morphologie und räumliche Lage von zwei Fallbeispielen im Detail untersucht: der vulkanischer Monte-Amarelo-Flankenkollaps der Insel Fogo, Kapverden, und die riesige

Tampen subaquatische Hangrutschung an dem passiven Kontinentalhang vor zentral Norwegen. Die Ablagerungen des Monte-Amarelo Flankenkollapses vor der vulkanischen Insel Fogo wurden mit einer Kombination aus hochauflösenden Sedimentecholot-, Fächerecholot- und Sedimentkerndaten untersucht. Die Daten zeigen, dass die laterale Ausdehnung der Monte-Amarelo Schuttlawine mehr als doppelt so groß ist wie bisher angenommen. Zudem konnte gezeigt werden, dass die Ablagerungen der Schuttlawine das mehrphasige Rutschen von bereits abgelagerten Sedimenten auslöste. Dieser Prozess ist bereits von Flankenabbrüchen auf den Kleinen Antillen (Karibik) bekannt. An Fogos subaquatischen Vulkanhängen konnten außerdem zahlreiche kleinvolumige Massentransportablagerungen nachgewiesen werden. Als zweites Fallbeispiel wurden die Ablagerungen der Tampen-Rutsunchung mit einem Gesamtvolumen von >1,000 km^3 untersucht. Unter Verwendung eines großen, hochauflösenden reflektions-seismischen 3D Datensatzes der Sediment bedeckten Abbruchkante der Tampen-Rutschung konnte festgestellt werden, dass die Massenumlagerung weitgehend während eines einzigen Ereignises entlang einer Gleitebene stattfand. Diese Beobachtung unterscheidet sich erheblich von anderen Megarutschungen, deren großes Gesamtvolumen das Ergebnis zahlreicher retrogressiver, kleinvolumiger Hangrutschungen ist. Dies hat wichtige Auswirkungen auf das Verständnis von Abläufen, die während einer großen Hangrutschung stattfinden können. Die hohe Datenauflösung ermöglicht es die Morphologie der Tampen-Rutschung im Detail zu untersuchen. So konnten Spreizungs- und Kompressionsregionen, die quer zum Streichen verlaufen, sowie hangabwärts orientierte Rutschungsbahnen und Kämme, die bis zu 40 m höher sind als die sie umgebenden Ablagerungen identifiziert werden. Dies ist das erste Mal, dass diese longitudinalen Kämme in dieser Wassertiefe gefunden wurden. Die Erkenntnisse, die durch diese beiden Fallbeispiele gewonnen wurden, haben wichtige Implikationen für das Verständnis wie derartige Hangrutschungen abgelagert werden, und welche Gefahren mit ihnen einhergehen können.

Contents

Chapter 1

Motivation and Outline

1.1 Motivation

Subaqueous landslides are globally widespread and occur in a variety of different settings, including in alpine lakes and fjords, at volcanic islands, and on active and passive continental margins (e.g. Hampton et al., 1996, Talling et al., 2014, Blahut et al., 2018, Sammartini et al., 2019). Additionally, they can be orders of magnitude larger than their terrestrial counterparts (Korup et al., 2007, Masson et al., 2010). For example, the submarine Storegga Slide offshore Norway that occurred 8,200 years ago involved 2,500 - 3,500 km^3 of material and ran out for over 800 km (Haflidason et al., 2005, Kvalstad et al., 2005). In comparison, the 1980 flank collapse of Mt St Helens involved $\sim$3 km^3 (Glicken, 1996), while the collapse of Mt Shasta, the largest known Quaternary terrestrial landslide, incorporated a volume of $\sim$26 km^3 (Crandell et al., 1984).

Moreover, subaqueous landslides can have devastating consequences – damaging critical offshore infrastructure such as wind farms, oil rigs, and submarine telecommunication cables that carry >95% of global data traffic (e.g. Heezen and Ewing, 1952, Thomas et al., 2010, Clare et al., 2017), as well as generating tsunami waves that can destroy coastal community infrastructure and result in significant loss of life (e.g. Harbitz et al., 2014, Ramalho et al., 2015, Nakata et al., 2020). Furthermore, submarine landslides can transport pollutants, such as microplastics, as well as organic matter to the deep sea (Korup et al., 2007, Azpiroz-Zabala et al., 2017, Kane and Clare, 2019). Buried subaqueous landslides also play an important role in hydrocarbon systems – controlling their distribution and geometry; acting as (or disrupting) seals; or even acting as hydrocarbon reservoirs (Weimer et al., 2007, Clare et al., 2018).

However, in spite of the hazards they pose and the environmental changes that can result from them, subaqueous landslides remain poorly understood. Furthermore, there are remarkably few direct observations of the development and failure of subaqueous landslides, and so understanding how past landslides have failed is critical in order to understand the risks posed by future landsliding events.

The morphology of a landslide provides critical information about the process of failure, which can then be used to understand the associated hazard. An interpretation of the morphology, however, is closely tied to the resolution and coverage of the data, and variations in these make it difficult to compare landslides in different settings. In this thesis, I employ both qualitative and quantitative methods to explore the relationship between subaqueous landslide morphology and the process of emplacement, using a variety of data from multiple settings.

1.2 Outline of this thesis

In **Chapter 2**, I provide an overview of subaqueous landslides, including their classification; morphology; and preconditioning and triggering factors; before outlining the main objectives of this thesis.

In **Chapter 3**, the results of a survey of the Monte Amarelo flank-collapse of Fogo Island in the Cape Verdes are presented. These show that the flank-collapse deposits extend across a much larger area than previously thought. Furthermore, we suggest that the deposition of the volcanic debris avalanche deposits triggered the failure of pre-existing seafloor sediments, as has been proposed previously for the islands of Montserrat and Martinique in the Lesser Antilles (Watt et al., 2012, Le Friant et al., 2015). We also document, for the first time, multiple landslides on the slopes south of Fogo, which may be unrelated to volcanic processes and instead indicative of ongoing tectonic activity in the region. This chapter is published as

> **Barrett, R.**, Lebas, E., Ramalho, R., Klaucke, I., Kutterolf, S., Klügel, A., Lindhorst, K., Gross, F., and Krastel, S. (2019). Revisiting the tsunamigenic volcanic flank collapse of Fogo Island in the Cape Verdes, offshore West Africa. *In* Geological Society of London Special Publications, 500, https://doi.org/10.1144/SP500-2019-187.

In **Chapter 4**, I present the results of the analysis of high resolution, 3D seismic data from the Tampen Slide, offshore Norway, which indicate that not all submarine megaslides form through the process of retrogression. In fact, they may fail as a single mass along a single glide plane – a variation in the failure mechanism that may have significant implications for

the resulting hazard potential (particularly the generation of tsunami waves). Furthermore, the high resolution of the data enables us to characterize the Tampen Slide headwall region at a high level of detail. We identify extensional and compressional (cross-slope) ridges, as well as longitudinal (downslope, movement-parallel) chutes and ridges that are up-to-40 m high. This is the first time longitudinal ridges of this size have been imaged in a deep marine setting. This chapter was submitted to the *Journal of Geophysical Research: Solid Earth* on 23.07.2020, and we received positive reviews for it on 25.09.2020. The revised manuscript will be resubmitted soon.

In **Chapter 5**, I compare the geomorphological signature of extensional and compressional ridges in subaqueous landslides, using data from the Tampen and Storegga Slides offshore Norway; the Malta Escarpment in the central Mediterranean Sea; and Lakes Lucerne and Zurich in Switzerland. Extensional and compressional ridges are common in subaqueous landslide deposits, but are geomorphically similar. This means that they can be difficult to distinguish where the data resolution is low or the full extent of the slide is not covered. This is particularly a problem for megaslides and landslide complexes, where failure often involves multiple phases that can be difficult to distinguish from one another due to the scale of sliding. Here, I compare the geomorphic signature of extensional and compressional ridges using spectral and principal component analysis, with the aim of finding whether they can be distinguished based solely on their geomorphology. At the time of submission of this thesis, this chapter is in preparation for submission to the *Journal of Geophysical Research: Earth Surface*.

In **Chapter 6**, the results of the previous chapters are brought together. I also discuss ongoing and future steps for this work.

References

Azpiroz-Zabala, M., Cartigny, M. J. B., Talling, P. J., Parsons, D. R., Sumner, E. J., Clare, M. A., Simmons, S. M., Cooper, C., and Pope, E. L. (2017). Newly recognized turbidity current structure can explain prolonged flushing of submarine canyons. *Science Advances*, 3(10).

Blahut, J., Klimeš, J., Rowberry, M., and Kusák, M. (2018). Database of giant landslides on volcanic islands – first results from the Atlantic Ocean. *Landslides*, 15(4):823–827.

Clare, M., Chaytor, J., Dabson, O., Gamboa, D., Georgiopoulou, A., Eady, H., Hunt, J., Jackson, C., Katz, O., Krastel, S., León, R., Micallef, A., Moernaut, J., Moriconi, R., Moscardelli, L., Mueller, C., Normandeau, A., Patacci, M., Steventon, M., Urlaub, M., Völker, D., Wood, L., and Jobe, Z. (2018). A consistent global approach for the morphometric characterization of subaqueous landslides. In Lintern, G., Mosher, D., Moscardelli, L., Bobrowsky, P., Campbell, C., Chaytor, J., Clague, J., Georgiopoulou, A., Lajeunesse, P., Normandeau, A., Piper, D., Scherwath, M., Stacey, C., and Turmel, D., editors, *Subaqueous Mass Movements and Their Consequences*, pages 455–477. Geological Society of London Special Publications, London, 477 edition.

Clare, M. A., Vardy, M. E., Cartigny, M. J., Talling, P. J., Himsworth, M. D., Dix, J. K., Harris, J. M., Whitehouse, R. J., and Belal, M. (2017). Direct monitoring of active geohazards: Emerging geophysical tools for deep-water assessments. *Near Surface Geophysics*, 15(4):427–444.

Crandell, D., Miller, C., Glicken, H., Christiansen, R., and Newhall, C. (1984). Catastrophic debris avalanche from ancestral Mount Shasta volcano, California. *Geology*, 12(3):143–146.

Glicken, H. (1996). Rockslide-debris avalanche of the May 18, 1980, Mount St. Helens Volcano, Washington. *U.S. Geological Survey Open-File*, 96(677).

Haflidason, H., Lien, R., Sejrup, H. P., Forsberg, C. F., and Bryn, P. (2005). The dating and morphometry of the Storegga Slide. *Marine and Petroleum Geology*, 22:123–136.

Hampton, M., Lee, H., and Locat, J. (1996). Submarine landslides. *Reviews of Geophysics*, 34(1):33–59.

Harbitz, C. B., Løvholt, F., and Bungum, H. (2014). Submarine landslide tsunamis: how extreme and how likely? *Natural Hazards*, 72:1341–1374.

Heezen, B. C. and Ewing, M. (1952). Turbidity currents and submarine slumps, and the 1929 Grand Banks Earthquake. *American Journal of Science*, 250:849–873.

Kane, I. A. and Clare, M. A. (2019). Dispersion, accumulation, and the ultimate fate of microplastics in deep-marine environments: A review and future directions. *Frontiers in Earth Science*, 7(80):1–27.

Korup, O., Clague, J. J., Hermanns, R. L., Hewitt, K., Strom, A., and Weidinger, J. (2007). Giant landslides, topography, and erosion. *Earth and Planetary Science Letters*, 261(3-4):578–589.

Kvalstad, T. J., Andresen, L., Forsberg, C. F., Berg, K., Bryn, P., and Wangen, M. (2005). The Storegga slide: Evaluation of triggering sources and slide mechanics. *Marine and Petroleum Geology*, 22(1-2):245–256.

Le Friant, A., Ishizuka, O., Boudon, G., Palmer, M., Talling, P., Villemant, B., Adachi, T., Aljahdali, M., Breitkreuz, C., Brunet, M., Caron, B., Coussens, M., Deplus, C., Endo, D., Feuillet, N.,

Fraas, A., Fujinawa, A., Hart, M., Hatfield, R., Hornbach, M., Jutzeler, M., Kataoka, K., Komorowski, J.-C., Lebas, E., Lafuerza, S., Maeno, F., Manga, M., Martnez-Colon, M., McCanta, M., Morgan, S., Saito, T., Slagle, A., Sparks, S., Stinton, A., Stroncik, N., Subramanyam, K., Tamura, Y., Trofimovs, J., Voight, B., Wall-Palmer, D., Wang, F., and Watt, S. (2015). Submarine record of volcanic island construction and collapse in the Lesser Antilles arc: First scientific drilling of submarine volcanic island landslides by IODP Expedition 340. *Geochemistry Geophysics Geosystems*, 16:420–442.

Masson, D. G., Wynn, R. B., and Talling, P. J. (2010). Large Landslides on Passive Continental Margins: Processes, Hypotheses and Outstanding Questions. In Mosher, D. C., Moscardelli, L., Shipp, R., Chaytor, J., Baxter, C., Lee, H., and Urgeles, R., editors, *Submarine Mass Movements and Their Consequences: Advances in Natural and Technological Hazards Research*, volume 28, pages 153–165. Springer, Dordrecht, Netherlands.

Nakata, K., Katsumata, A., and Muhari, A. (2020). Submarine landslide source models consistent with multiple tsunami records of the 2018 Palu tsunami, Sulawesi, Indonesia. *Earth, Planets and Space*, 72(44):1–16.

Ramalho, R. S., Winckler, G., Madeira, J., Helffrich, G. R., Hipólito, A., Quartau, R., Adena, K., and Schaefer, J. M. (2015). Hazard potential of volcanic flank collapses raised by new megatsunami evidence. *Science Advances*, 1(9):1–11.

Sammartini, M., Moernaut, J., Anselmetti, F. S., Hilbe, M., Lindhorst, K., Praet, N., and Strasser, M. (2019). An atlas of mass transport deposits in lakes. *Geophysical Monograph Series*, 246:201–226.

Talling, P., Clare, M., Urlaub, M., Pope, E., Hunt, J., and Watt, S. (2014). Large Submarine Landslides on Continental Slopes: Geohazards, Methane Release, and Climate Change. *Oceanography*, 27(2):32–45.

Thomas, S., Hooper, J., and Clare, M. (2010). Constraining geohazards to the past: impact assessment of submarine mass movements on seabed developments. In Mosher, D., Moscardelli, L., Shipp, R., Chaytor, J., Baxter, C., Lee, H., and Urgeles, R., editors, *Submarine Mass Movements and Their Consequences: Advances in Natural and Technological Hazards Research*. Springer, Cham, Switzerland, 28 edition.

Watt, S. F., Talling, P. J., Vardy, M. E., Masson, D. G., Henstock, T. J., Hühnerbach, V., Minshull, T. A., Urlaub, M., Lebas, E., Le Friant, A., Berndt, C., Crutchley, G. J., and Karstens, J. (2012). Widespread and progressive seafloor-sediment failure following volcanic debris avalanche emplacement: Landslide dynamics and timing offshore Montserrat, Lesser Antilles. *Marine Geology*, 323-325:69–94.

Weimer, P., Slatt, R. M., and Bouroullec, R. (2007). Introduction to the petroleum geology of deepwater settings. *AAPG Studies in Geology*, 57:419–455.

Chapter 2

Introduction

Subaqueous landslides[1] are ubiquitous features of both active and passive continental margins, as well as volcanic islands, fjords and lake environments (e.g. Hampton et al., 1996, Hühnerbach and Masson, 2004, Harbitz et al., 2014b, Blahut et al., 2018, Bellwald et al., 2019a, Sammartini et al., 2019). One of the largest known submarine landslides, the Agulhas Slide offshore South Africa, ran out across 750 km and involved a volume of ∼20,000 km^3 (Dingle, 1977), but such a large and extensive landslide is by no means unique in the submarine realm (Table 2.1). The 2,500-3,500 km^3 Storegga Slide offshore Norway (Haflidason et al., 2004), perhaps one of the best studied and understood subaqueous landslides worldwide, resulted in a tsunami that ran up to heights of up to 15-25 metres in the Shetland Islands and Norway, and its deposits are found as far away as the southern North Sea (Bondevik et al., 2005, Weninger et al., 2008). Landslides around volcanic islands can also involve prodigious volumes – for example, the Nuuanu landslide offshore Oahu in Hawaii involved 5,000 km^3 of volcanic material (Moore et al., 1989). Moreover, even comparatively small subaqueous landslides can generate catastrophic tsunami waves. The September 2018 flank collapse of Anak Krakatau in Indonesia, which involved a volume of 0.22-0.3 km^3 (Grilli et al., 2019, Zengaffinen et al., 2020), triggered a tsunami that ran up to 13 m above sea level, and claimed the lives of more than 400 people (Muhari et al., 2019). Several months later, in December 2018, a pair of small submarine landslides (0.02 and 0.07 km^3) triggered by a large earthquake (M_w 7.5) in Palu Bay (Sulawesi, Indonesia) led to a tsunami that ran up to heights of 10 m, resulting in the deaths of 2,000 people and causing significant damage to coastal infrastructure (Omira et al., 2019, Nakata et al., 2020).

The volume, geometry, and failure mechanism of subaqueous landslides are key parameters that determine the magnitude of associated hazards, including the generation of tsunami

[1] In this thesis, the term *subaqueous* includes both oceanic and lake environments, while *submarine* refers to the oceanic (marine) realm.

waves (Harbitz et al., 2014b). However, it should be noted that not all subaqueous landslides generate tsunami waves. For example, the Traenadjupet Slide offshore Norway, which involved a total volume of 500-1,000 km^3, is thought to have failed too slowly, and too far from the coast, to generate a tsunami (Laberg and Vorren, 2000, Løvholt et al., 2017).

Submarine landslides also pose a risk to critical offshore infrastructure, such as telecommunications cables that now carry >95% of global data traffic (e.g. Carter et al., 2014, Clare et al., 2017). This is most famously documented by the 1929 Grand Banks (Newfoundland) earthquake-triggered slump and the resulting turbidity current, which systematically broke all the seafloor cables within 500 km downslope of the slump (Heezen and Ewing, 1952). A repetition of this event today – where there are many more seafloor cables linking North America and Europe, and the global economy and connectivity between people and nations depends so heavily on the Internet – would wreck havoc. The downslope termination of submarine landslide deposits on the continental shelf also influences the location of international economic boundaries as defined by the United Nations Convention on the Law of the Sea (Mosher et al., 2016, Clare et al., 2018a).

Submarine landslides can also transport pollutants, such as microplastics, as well as organic matter to the deep sea (Korup et al., 2007, Azpiroz-Zabala et al., 2017, Kane and Clare, 2019). While the failure itself can destroy seafloor habitats, both the upper surface of the deposits and the evacuation zone have been shown to subsequently become rich habitats for seafloor biological communities (e.g. Okey, 1997, Panieri et al., 2012, Savini et al., 2016). Furthermore, submarine landslides play an important role in hydrocarbon systems: when buried, they can act as seals or barriers to fluid migration; create and modify fluid migration pathways; control the distribution of reservoirs on the continental slope; and even act as reservoirs (Weimer et al., 2007, Clare et al., 2018a, and references therein).

However, in spite of their obvious and multi-fold hazard potential, subaqueous landslides remain poorly understood, and questions relating to their distribution in space and time, preconditioning and triggering factors, and process of failure remain unanswered. In the following sections, I outline the different types of subaqueous landslide (**Section 2.1**), before discussing how their morphology helps us to understand how they failed (**Section 2.2**), and their preconditioning and triggering factors (**Section 2.3**). I conclude by outlining the objectives of this thesis (**Section 2.4**).

Table 2.1: Examples of some large volume submarine landslides in a variety of settings

	Area (km^2)	**Volume (km^3)**	**Reference**
Agulhas Slide, offshore SE Africa	79,500	20,000	Dingle (1977)
Ayabacas Formation, southern Peru	>80,000	>10,000	Callot et al. (2008)
Nuuanu Landslide, offshore NE Oahu, Hawaii	23,000	5,000	Moore et al. (1989)
Ruatoria Debris Avalanche, offshore New Zealand	3,400	3,150	Collot et al. (2001)
Storegga Slide, offshore Norway	95,000	2,500-3,500	Haflidason et al. (2004)
Cape Fear Slide Complex, US Atlantic margin	>25,000	1,700	Hornbach et al. (2007), Hill et al. (2019)
Hinlopen/Yermak Slide, northern Svalbard margin	10,000	1,350	Vanneste et al. (2006), Winkelmann et al. (2008)
Tampen Slide, offshore Norway	>25,500	>1,000	Nygård et al. (2005), Barrett et al. (in review)
Combined Orotava, Icod and Roques de García debris avalanches, Tenerife, Canary Islands	5,500	1,000	Watts and Masson (1995), Teide Group (1997)
Israel Slump Complex, Levant Basin, offshore Israel	4,800	1,000	Frey-Martínez et al. (2005)
Mauritania Slide, offshore NW Africa	34,000	700	Antobreh and Krastel (2007)
Sahara Slide, offshore NW Africa	70,000	600	Embley (1982), Georgiopoulou et al. (2010)

2.1 Types of subaqueous landslide

Subaqueous landslides are gravitationally-driven mass wasting deposits that have previously been classified in several different ways in attempts to capture variations in their transport and relation to the source area, morphology, and sedimentary properties (e.g. Dott, 1963, Nardin et al., 1979, Hampton et al., 1996, Shanmugam, 2000, Mulder and Alexander, 2001, Moscardelli and Wood, 2008, Clare et al., 2018a). Their classification is somewhat complicated by the fact that a single event can occur in multiple phases that are separated in time, and the deposits of those phases can both fail in different manners, and have different properties (Nardin et al., 1979, Moscardelli and Wood, 2008). In this thesis, the following terminology is used to describe the different types of subaqueous landslides (Figure 2.1):

- *Slide* refers to the purely translational failure of material or blocks along a single glide plane, and involves little or no internal deformation or rotation (Locat and Lee, 2000, Moscardelli and Wood, 2008). The blocks can also disintegrate into smaller blocks as they translate downslope.
- A *slump* describes a mass transport deposit (MTD) whose translation along a shear surface is accompanied by rotation along discrete shear surfaces and some internal deformation (Moscardelli and Wood, 2008). The failure surface beneath such a rotational slide is typically upwardly-concave (Hampton et al., 1996).
- When shear is distributed throughout the deformed mass, and the mass remains cohesive, the MTD is referred to as a *debris flow* (Mulder and Alexander, 2001, Moscardelli and Wood, 2008). Such mass transport deposits are highly mobile, and the failed mass usually completely evacuates from the headwall area (Locat and Lee, 2000).
- *Turbidity currents* occur when the flow has a very low concentration by volume and the particles are transported by fluid turbulence (Bagnold, 1962, Mulder and Alexander, 2001). When associated with subaqueous landslides, turbidity currents develop at the leading edge of the landslide (the *toe*), and can run out over hundreds of kilometers even when the slope gradient is minimal ($<1°$) (e.g. Heezen and Ewing, 1952, Nisbet and Piper, 1998, Talling et al., 2012). Turbidity currents can also occur independently of subaqueous landslides; for example, as a result of earthquakes, river flooding, and storms, or even without an external trigger (Talling et al., 2013, Paull et al., 2018).

Note the progressive sense of this classification system – it should be clear that subaqueous landslides can also develop into other types during the course of failure. Understanding how failure occurs and develops is critical for constraining the associated hazards (Locat and Lee, 2000, Harbitz et al., 2014b).

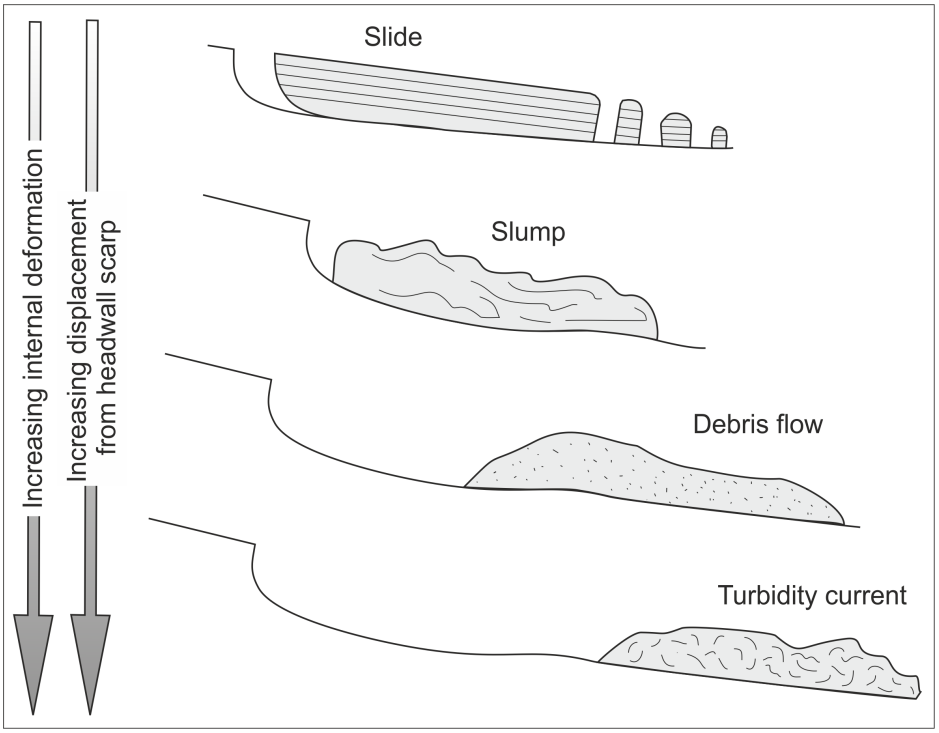

Figure 2.1: Schematic showing the different types of subaqueous landslides (modified after Moscardelli and Wood, 2008).

Furthermore, subaqueous landslides can either be *frontally emergent* or *frontally confined* (Figure 2.2). Following the classification of Frey-Martínez et al. (2006), a frontally emergent landslide ramps up from the failed basal surface and can then translate freely across the undeformed sediments. In contrast, the deposits of a frontally confined landslide are confined by a frontal ramp, and do not progress beyond the original failed basal surface.

Large cracks in the unfailed sediment upslope of, or adjacent to, the headwall (referred to as *crown cracks*) have been documented in numerous settings (e.g. Micallef et al., 2007b, Li et al., 2017, Normandeau et al., 2019). Crown cracks are indicative of instability and can develop further into headwalls, resulting in the upslope migration of failure in a process known as *retrogression* (Hampton et al., 1996). Retrogression is commonly associated with large submarine landslide complexes (where there are many smaller failures within the same headwall area) and megaslides (submarine landslides of prodigious volume; defined here as landslides with a volume larger than 1,000 km^3, following Hjelstuen et al., 2007), and is widely thought to account for the large volume of megaslides on passive continental margins (Laberg and Vorren, 2000, Kvalstad et al., 2005, Vanneste et al., 2006, Antobreh and Krastel, 2007, Georgiopoulou et al., 2010, Masson et al., 2010, Hill et al., 2019). Crown cracks can also develop into *spreading* – a region of extension that is characterized by a series of repetitive ridges and troughs parallel to the headwall scarp (Figure 2.3, Micallef et al., 2007b). Spreading is thought to result from seismic loading and loss of basal support,

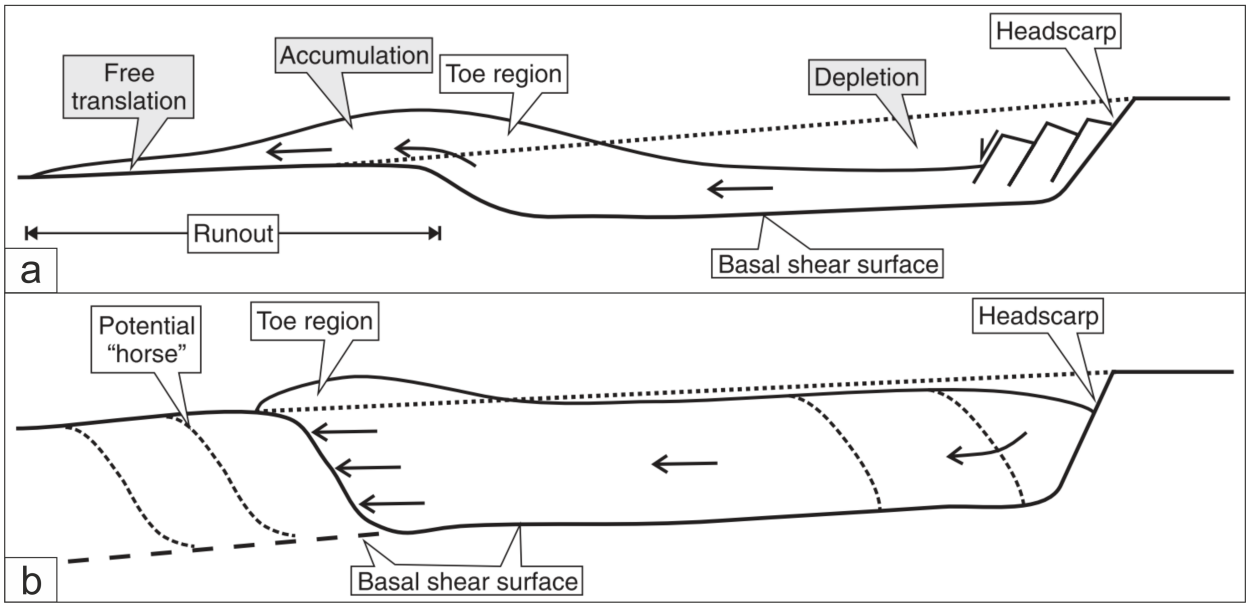

Figure 2.2: Schematic highlighting the difference between (a) frontally emergent and (b) frontally confined landslides (from Frey-Martínez et al., 2006).

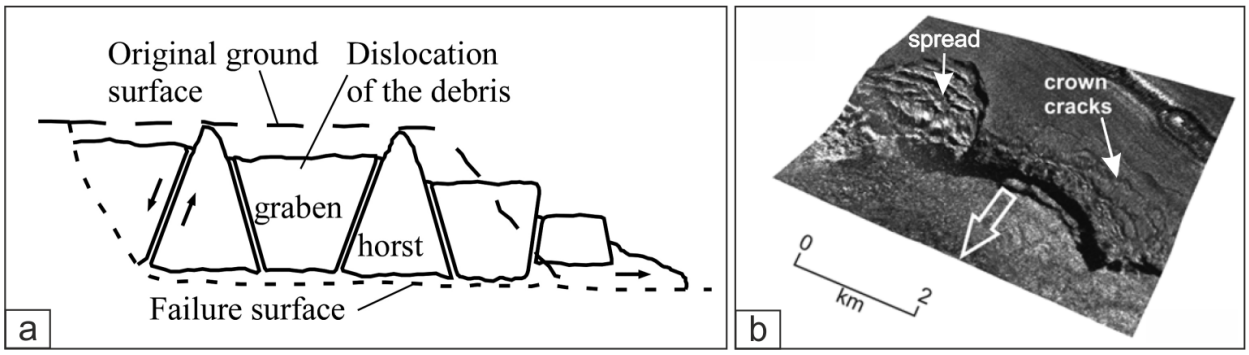

Figure 2.3: Spreading in subaqueous landslides. (a) Schematic representation of spreading ridges and the original ground surface (from Locat et al., 2013). (b) Example of spreading ridges in the headwall region of the Storegga Slide, offshore Norway, using a fusion of TOBI side-scan and bathymetry data (modified after Micallef et al., 2007b). Note the relation between crown cracks and spreading.

so that it typically occurs following the formation of a headwall and the excavation of the failed mass (Lastras et al., 2003, Micallef et al., 2007b).

The landsliding processes and types described so far have been discussed only insofar as they relate to subaqueous landsliding processes; however, it is also pertinent to mention landslides which begin out of water and continue beneath it, such as landslides in fjords, lakes, and at volcanic islands (Blahut et al., 2018, Bellwald et al., 2019a, Sammartini et al., 2019). Such multi-medium failures (involving both air and water) can create strong impulse waves that can travel rapidly across the water surface (e.g. Harbitz et al., 2014a, Ramalho et al., 2015, Zengaffinen et al., 2020).

2.2 Morphology as an indicator of failure mechanics

The morphology of a landslide provides critical information about the process of failure, which can then be used to understand the associated hazard. In their review of kinematic indicators for submarine landslides, Bull et al. (2009) built on the previous work of Prior et al. (1984) and identified indicators that dominate the headwall, translational, and toe regions of submarine landslides (Figure 2.4). The headwall domain is dominated by extension, and includes the headwall scarp and extensional ridges and blocks, such as those generated through the process of spreading described in the previous section. In contrast, the toe domain at the downslope end of the slide is dominated by compressional features, including folds and thrust systems (for frontally confined landslides), and pressure ridges – defined as the surface expression of thrusts that cannot be resolved by the data (for frontally emergent/unconfined landslides; Schnellmann et al., 2005, Frey-Martínez et al., 2006, Bull et al., 2009). Compressional ridges are aligned perpendicular to the flow direction, and have similar geomorphology to spreading ridges found within the headwall domain. Outrunner blocks – relatively undeformed blocks that detach and move independently of the landslide mass – can also often be found downslope of the landslide toe (e.g. De Blasio et al., 2006).

Several kinematic indicators – including translated blocks (e.g. Alves, 2015); folds (e.g. Webb and Cooper, 1988); striated grooves on the basal plane (e.g. Gee et al., 2005); second-order flow fabric (i.e. lineations that are not laterally continuous or cross-cutting; Masson et al., 1993, Gafeira et al., 2010); and basal ramps and flats (steps in the basal plane; e.g. Gamboa

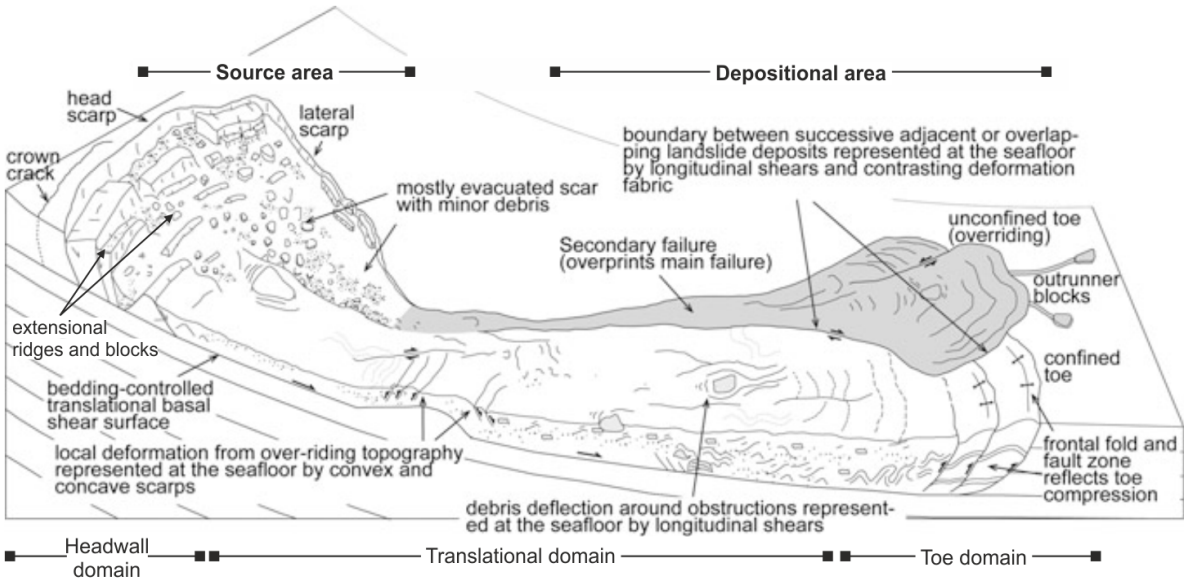

Figure 2.4: Kinematic indicators within a subaqueous landslide (modified after Prior et al., 1984, Bull et al., 2009, Mountjoy and Micallef, 2018).

and Alves, 2016) – can also be found within the translational domain that links the upslope- and downslope-limits of the landslide. The orientation of these features enables the flow direction and landslide mechanics to be constrained.

There has recently been a push within the subaqueous landslide community towards a more quantitative and uniform analysis, so that landslides in different settings can be compared more easily (e.g. Hühnerbach and Masson, 2004, Moscardelli and Wood, 2016, Clare et al., 2018a). Moscardelli and Wood (2016) compiled a morphometric database documenting the length, area, volume and thickness of subaqueous landslides from different settings around the world. Their analysis suggests that morphometric parameters are linked to the geometry, geological setting, and causal mechanisms, such that one can estimate the dimensions of landslides in areas of low data coverage. While such a result is clearly a step forward, these quantitative studies still rely heavily on user input, which means that there is a large amount of subjectivity involved in their analysis. Clare et al. (2018a) – the authors of which include twenty-three experts in submarine landslides – separately analysed a bathymetric dataset covering the Valdes Slide, offshore Chile (Figure 2.5), and then compared their results. While simple locational parameters (latitude, longitude and water depth) varied within <5% of the mean, morphological parameters that required a higher level of user input (such as the scar perimeter length, maximum deposit width, and maximum deposit thickness) varied much more significantly (by 57%, 45%, and 41%, respectively, for those three parameters). Such variation means that it is difficult to compare landslides in different tectonic settings, and/or that have been analysed by different scientists – a comparison that is critical to building up our understanding of submarine landsliding processes, their frequency, and their distribution, amongst other factors.

The use of morphological parameters such as slope curvature and gradient to study and understand subaqueous landslides has become more commonplace in the last decade (e.g. Micallef et al., 2007a, Lecours et al., 2016, 2017), helping to reduce subjectivity in the identification of morphological features. While there are a multitude of terrain attributes that can be calculated, they tend to correlate heavily with each other, and Lecours et al. (2017) found that the majority of topographic and morphologic variations can be identified using just 6-7 specific terrain attributes: topographic mean (average elevation within a neighbourhood of adjacent cells); topographic position index (the elevation of a particular cell relative to the mean elevation of cells around that cell); rugosity (a measure of the roughness of the surface); slope gradient; and northward/eastward orientation (slope aspect) (Figure 2.5).

Furthermore, where repeat bathymetric surveys are available, one can also use the variations between datasets to investigate changing morphology, sediment flux, and slope stability over

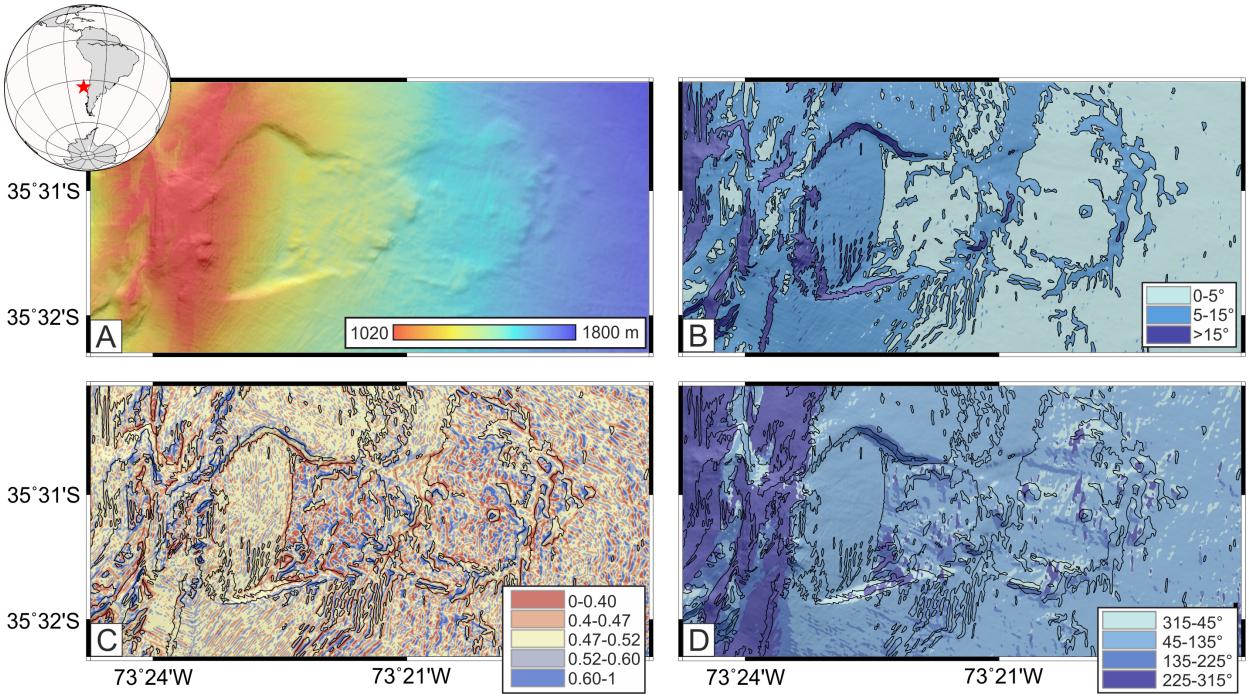

Figure 2.5: A few of the terrain attributes for the Valdes Slide, offshore Chile: (A) Hillshaded bathymetry data, (B) Slope gradient, (C) Bathymetric Position Index, (D) Slope aspect. The black lines highlight the slope gradient boundaries as demarcated in (B).

time. This is particularly useful in regions that are prone to sub-decadal instabilities, such as river deltas (e.g. the Mississippi River Delta, Louisiana, USA; Obelcz et al., 2017, 2020), or submarine canyons/channels (e.g. Bute Inet, Canada; Heijnen et al., 2020). However, such datasets are very uncommon.

2.3 Preconditioning and triggering factors

Landslides are ubiquitous features of continental slopes, active river deltas, submarine canyon-fan systems, fjords, lakes, and volcanic islands and, in all of these settings, failure is ultimately triggered when the gravitational forces exceed the resisting forces (Hampton et al., 1996, Locat and Lee, 2000). There are a number of factors that can both precondition slopes for failure and ultimately trigger that failure; some of which increase the stress, while others decrease the stress (Figure 2.6, Locat and Lee, 2000). While these factors are generally known, the relative importance of, and interplay between, individual factors is often discussed in the literature (e.g. Hampton et al., 1996, Hornbach et al., 2007, Leynaud et al., 2009, Masson et al., 2010, Urlaub et al., 2015, Bellwald et al., 2019a).

The Storegga Slide, which occurred 8,200 years ago offshore Norway and is arguably the best-studied submarine landslide globally, is thought to have been preconditioned for failure

$$F = \frac{\Sigma \text{ Resisting Forces}}{\Sigma \text{ Gravitational forces}}$$

Reducing the Strength	Increasing the Stresses
Earthquakes	Earthquakes
Wave Loading	**Wave Loading**
Tides	Tides
Sedimentation	**Sedimentation**
Gas	Gas
Glaciation	Glaciation
	Erosion
	Diapirs

Figure 2.6: Triggering and preconditioning factors for subaqueous landslides (from Locat and Lee, 2000).

by high excess pore pressure, and then triggered by an earthquake on the lower continental slope (Haflidason et al., 2004, Bryn et al., 2005, Kvalstad et al., 2005, Bellwald et al., 2019a). The timing of the Storegga Slide, shortly after the transition to an interglacial period, led to the development of a model where slope stability in the region is closely tied to glacial and interglacial cycles (Bryn et al., 2005). In that model, the rapid deposition of sediment following the retreat of ice results in the development of overpressure, and a landslide is then triggered by seismic activity related to isostatic rebound (Figure 2.7). This process is thought to repeat every glacial cycle (Bryn et al., 2005).

The presence of gas beneath and within submarine landslides – e.g. the Storegga Slide (Solheim et al., 2005); Tuaheni Slide, offshore New Zealand (Gross et al., 2018); the Humboldt Slide offshore California (Field and Barber, 2002); and the Ana and pre-Ana slides in the Mediterranean (Berndt et al., 2012) – has also led to discussion about the role of fluid migration in landslide development. This preconditioning factor is unique to the marine environment (Locat and Lee, 2000). Its role in landslide development, however, is difficult to constrain due to the destruction of the basal plane (and displacement and deformation of the sediments) during failure.

The timing of debris flows and megaturbidites on non-glaciated, European continental margins (with steeper slope angles) is also thought to be linked to glacial-interglacial cycles, with landslides occurring during glacial maximums when rivers transport sediment all the way to the shelf edge (Leynaud et al., 2009, Badhani et al., 2020). Here again, the rate of sediment accumulation is an important parameter for the generation of landslides. However, large submarine landslides also occur in areas such as offshore northwest Africa, where the rate of sediment accumulation is too low (<0.15 m/kyr) to generate enough overpressure or

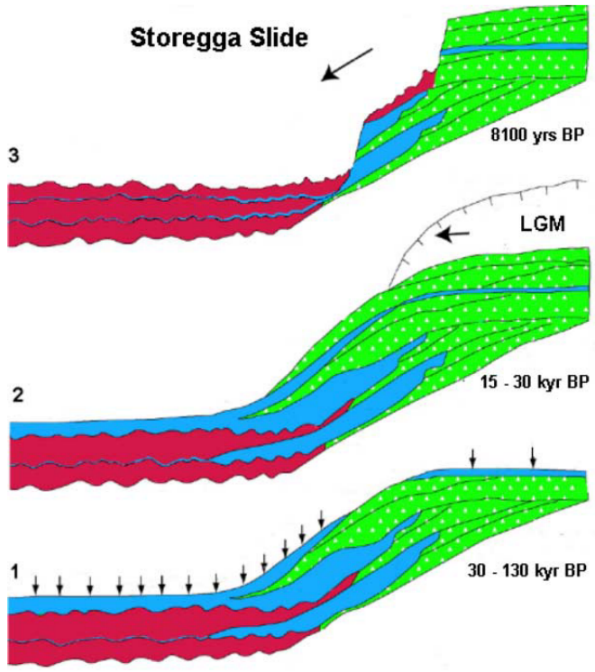

Figure 2.7: A model for the development of the Storegga Slide, offshore Norway. (1) Soft marine clays are deposited during the interglacial period; (2) Ice extends to the shelf edge and glacial sediments are deposited at the Last Glacial Maximum (LGM); (3) The Storegga Slide. Green: glacial sediments; Red: slide deposits; Blue: marine sediments. From Bryn et al. (2005).

lateral fluid flow (Urlaub et al., 2015). In such cases, the presence of a layer that is either extremely rich in organic matter (such as diatom oozes), or undergoes a rapid decrease in porosity, may be enough to generate failure in the absence of other factors (Urlaub et al., 2015, 2018a). Such layers, capped by low-permeability clay, prevent the upward migration of fluids and may lead to the generation of overpressure (Urlaub et al., 2018a).

Tephra has also been suggested to act as a *weak layer* – a layer of inherently lower strength than adjacent layers, which is thereby prone to failure (Harders et al., 2010, Locat et al., 2014, Moernaut et al., 2019). This is especially relevant for slopes proximal to volcanoes, such as offshore Chile (Moernaut et al., 2019), or volcanic islands. The slopes of volcanic islands are particularly prone to failure, which can be triggered by variety of both internal and external factors including dyke and sill intrusions; volcanic eruptions and tremor; earthquakes; flank over-steepening; the weight of new volcanic material on the island flanks; weakening of the volcanic edifice by weathering and hydrothermal activity; and, for smaller landslides, by the effects of wave, wind and storm activity (e.g. Siebert, 1984, Begét and Kienle, 1992, Murray and Voigt, 1996, McGuire, 1996, 2003, Cervelli et al., 2002, Tibaldi et al., 2008, Casalbore et al., 2011, 2015, Gross et al., 2014, Clare et al., 2018b). Such factors occur over timescales ranging from seconds to thousands of years (McGuire, 1996, Urlaub et al., 2018b) and are globally widespread (Blahut et al., 2019). Furthermore, anthropogenic

activities such as land clearance and embankment filling may contribute to the instability of volcanic flanks and fjord slopes (L'Heureux et al., 2010, Clare et al., 2018b).

Erosional processes and high sedimentation rates also create problems for studying submarine landslides. Erosion of the headwall often begins soon after a landslide occurs, either through current-related processes, or ongoing instability (Mountjoy and Micallef, 2018). This can make reconstruction of the landslide's geometry and failure mechanism challenging. In addition, many submarine landslides occur in regions of high sedimentation, such as in trough mouth fans (e.g. Nygård et al., 2005, Normandeau et al., 2019). These high sedimentation rates can help to precondition the slides for failure through the generation of over-pressure (Leynaud et al., 2009, Bellwald et al., 2019b), but also result in the rapid burial of the slides. Such burial means that the full lateral extent, volume, failure mechanism, and even existence of many subaqueous slides remains unknown (e.g. the giant Tampen Slide offshore Norway; Nygård et al., 2005). These parameters are critical for understanding the causes and frequency of landslides, their related hazards, and which areas more (or less) likely to fail (Harbitz et al., 2014b).

2.4 Objectives of this thesis

This chapter has highlighted that constraining the geometry of a landslide is critical for understanding both the process of failure and the corresponding hazards. Such an analysis, however, is heavily dependent on the resolution and coverage of the data. The overarching aim of this thesis is to investigate what the morphology of subaqueous landslides tells us about the process of failure. To this end, I make use of a variety of high resolution geophysical data from a number of different settings to both qualitatively and quantitatively investigate the morphology of mass transport deposits and the surrounding area at a high level of detail. I investigate two end-members – the flank collapse of a volcanic island and mass transport deposits on the adjacent submarine slopes (Fogo Island in the Cape Verdes); and a submarine megaslide on a passive margin (the Tampen Slide, offshore Norway) – in more detail. Specifically, I answer the following questions:

For the two end-member subaqueous landslides:

- How does the geometry and morphology of these landslides compare to other landslides in similar settings?
- Were the landslides emplaced in a single phase, or were there multiple phases? Can giant landslides fail in a single phase, or does retrogression always account for their prodigious volumes?

- What are the implications of these findings for the development and hazard potential of similar landslides?

And more generally:

- What do morphological features (kinematic indicators) within the landslide deposits tell us about the process of failure? Moreover, can we quantitatively distinguish between kinematic indicators that have similar geomorphology?
- What quantitative morphometric approaches could help to improve analysis of subaqueous landslide morphology and make it less subjective?

References

Alves, T. M. (2015). Submarine slide blocks and associated soft-sediment deformation in deep-water basins: A review. *Marine and Petroleum Geology*, 67:262–285.

Antobreh, A. A. and Krastel, S. (2007). Mauritania Slide Complex: Morphology, seismic characterisation and processes of formation. *International Journal of Earth Sciences*, 96(3):451–472.

Azpiroz-Zabala, M., Cartigny, M. J. B., Talling, P. J., Parsons, D. R., Sumner, E. J., Clare, M. A., Simmons, S. M., Cooper, C., and Pope, E. L. (2017). Newly recognized turbidity current structure can explain prolonged flushing of submarine canyons. *Science Advances*, 3(10).

Badhani, S., Cattaneo, A., Collico, S., Urgeles, R., Dennielou, B., Leroux, E., Colin, F., Garziglia, S., Rabineau, M., and Droz, L. (2020). Integrated geophysical, sedimentological and geotechnical investigation of submarine landslides in the Gulf of Lions (Western Mediterranean). In Georgiopoulou, A., Amy, L., Benetti, S., Chaytor, J., Clare, M., Gamboa, D., Haughton, P., Moernaut, J., and Mountjoy, J., editors, *Subaqueous Mass Movements and Their Consequences: Advances in Process Understanding, Monitoring and Hazard Assessments*, volume 500, pages 359–376. Geological Society of London Special Publications, London.

Bagnold, R. A. (1962). Auto-suspension of transported sediment; turbidity currents. *Proceedings of the Royal Society A: Mathematical, Physical and Engineering Sciences*, 265(1322).

Barrett, R., Bellwald, B., Talling, P., Gross, F., Berndt, C., Micallef, A., Planke, S., Myklebust, R., and Krastel, S. (in review). Can a submarine megaslide on a passive margin fail along a single glide plane? *Journal of Geophysical Research: Solid Earth*.

Begét, J. E. and Kienle, J. (1992). Cyclic formation of debris avalanches at Mount St Augustine volcano. *Nature*, 356:701–704.

Bellwald, B., Hjelstuen, B., Sejrup, H., Stokowy, T., and Kuvås, J. (2019a). Holocene mass movements in west and mid-Norwegian fjords and lakes. *Marine Geology*, 407:192–212.

Bellwald, B., Urlaub, M., Hjelstuen, B. O., Sejrup, H. P., Sørensen, M. B., Forsberg, C. F., and Vanneste, M. (2019b). NE Atlantic continental slope stability from a numerical modeling perspective. *Quaternary Science Reviews*, 203:248–265.

Berndt, C., Costa, S., Canals, M., Camerlenghi, A., De Mol, B., and Saunders, M. (2012). Repeated slope failure linked to fluid migration: The Ana submarine landslide complex, Eivissa Channel, Western Mediterranean Sea. *Earth and Planetary Science Letters*, 319-320:65–74.

Blahut, J., Klimeš, J., Rowberry, M., and Kusák, M. (2018). Database of giant landslides on volcanic islands – first results from the Atlantic Ocean. *Landslides*, 15(4):823–827.

Blahut, J., Balek, J., Klimeš, J., Rowberry, M., Kusák, M., and Kalina, J. (2019). A comprehensive global database of giant landslides on volcanic islands. *Landslides*, 16(10):2045–2052.

Bondevik, S., Løvholt, F., Harbitz, C. B., Mangerud, J., Dawson, A., and Svendsen, J. I. (2005). The Storegga Slide tsunami – comparing field observations with numerical simulations. In *Ormen Lange – an Integrated Study for Safe Field Development in the Storegga Submarine Area*, pages 195–208. Elsevier.

Bryn, P., Berg, K., Forsberg, C. F., Solheim, A., and Kvalstad, T. J. (2005). Explaining the Storegga Slide. *Marine and Petroleum Geology*, 22(1-2):11–19.

Bull, S., Cartwright, J., and Huuse, M. (2009). A review of kinematic indicators from mass-transport complexes using 3D seismic data. *Marine and Petroleum Geology*, 26(7):1132–1151.

Callot, P., Sempere, T., Odonne, F., and Robert, E. (2008). Giant submarine collapse of a carbonate platform at the Turonian-Coniacian transition: The Ayabacas Formation, southern Peru. *Basin Research*, 20(3):333–357.

Carter, L., Gavey, R., Talling, P. J., and Liu, J. T. (2014). Insights into submarine geohazards from breaks in subsea telecommunication cables. *Oceanography*, 24(3):58–67.

Casalbore, D., Romagnoli., C., Bosman, A., and Chiocci, F. L. (2011). Potential tsunamigenic landslides at Stromboli Volcano (Italy): insight from marine DEM analysis. *Geomorphology*, 126:42–50.

Casalbore, D., Romagnoli, C., Pimentel, A., Quartau, R., Casas, D., Ercilla, G., Hipólito, A., Sposato, A., and Chiocci, F. L. (2015). Volcanic, tectonic and mass-wasting processes offshore Terceira Island (Azores) revealed by high-resolution seafloor mapping. *Bulletin of Volcanology*, 77(24).

Cervelli, P., Segall, P., Johnson, K., Lisowski, M., Miklius, A., and Building, M. (2002). Sudden aseismic fault slip on the south flank of Kilauea volcano. *Nature*, 415:1014–1018.

Clare, M., Chaytor, J., Dabson, O., Gamboa, D., Georgiopoulou, A., Eady, H., Hunt, J., Jackson, C., Katz, O., Krastel, S., León, R., Micallef, A., Moernaut, J., Moriconi, R., Moscardelli, L., Mueller, C., Normandeau, A., Patacci, M., Steventon, M., Urlaub, M., Völker, D., Wood, L., and Jobe, Z. (2018a). A consistent global approach for the morphometric characterization of subaqueous landslides. In Lintern, G., Mosher, D., Moscardelli, L., Bobrowsky, P., Campbell, C., Chaytor, J., Clague, J., Georgiopoulou, A., Lajeunesse, P., Normandeau, A., Piper, D., Scherwath, M., Stacey, C., and Turmel, D., editors, *Subaqueous Mass Movements and Their Consequences*, pages 455–477. Geological Society of London Special Publications, London, 477 edition.

Clare, M. A., Vardy, M. E., Cartigny, M. J., Talling, P. J., Himsworth, M. D., Dix, J. K., Harris, J. M., Whitehouse, R. J., and Belal, M. (2017). Direct monitoring of active geohazards: Emerging geophysical tools for deep-water assessments. *Near Surface Geophysics*, 15(4):427–444.

Clare, M. A., Le Bas, T., Price, D. M., Hunt, J. E., Sear, D., Cartigny, M. J. B., Vellinga, A., Symons, W., Firth, C., and Cronin, S. (2018b). Complex and Cascading Triggering of Submarine Landslides and Turbidity Currents at Volcanic Islands Revealed From Integration of High-Resolution Onshore and Offshore Surveys. *Frontiers in Earth Science*, 6:1–24.

Collot, J.-Y., Lewis, K., Lamarche, G., and Lallemand, S. (2001). The giant Ruatoria debris avalanche on the northern Hikurangi margin, New Zealand: Result of oblique seamount subduction. *Journal of Geophysical Research: Solid Earth*, 106(B9):19271–19297.

De Blasio, F. V., Engvik, L. E., and Elverhøi, A. (2006). Sliding of outrunner blocks from submarine landslides. *Geophysical Research Letters*, 33(6).

Dingle, R. V. (1977). The anatomy of a large submarine slump on a sheared continental margin (SE Africa). *Journal of the Geological Society*, 134(3):293–310.

Dott, R. (1963). Dynamics of subaqueous gravity depositional processes. *AAPG Bulletin*, 47:104–128.

Embley, R. W. (1982). Anatomy of Some Atlantic Margin Sediment Slides and Some Comments

on Ages and Mechanisms. In Saxov, S. and Nieuwenhuis, J., editors, *Marine Slides and Other Mass Movements*. Springer, Boston, MA, 6 edition.

Field, M. and Barber, J. (2002). A Submarine Landslide Associated with Shallow Seafloor Gas and Gas Hydrates off Northern California. In Schwab, W. C., Lee, H. J., and Twichell, D. C., editors, *Submarine Landslides: Selected Studies in the U.S. Exclusive Economic Zone*. U.S. Geological Survey Bulletin.

Frey-Martínez, J., Cartwright, J., and Hall, B. (2005). 3D seismic interpretation of slump complexes: Examples from the continental margin of Israel. *Basin Research*, 17(1):83–108.

Frey-Martínez, J., Cartwright, J., and James, D. (2006). Frontally confined versus frontally emergent submarine landslides: A 3D seismic characterisation. *Marine and Petroleum Geology*, 23(5):585–604.

Gafeira, J., Long, D., Scrutton, R., and Evans, D. (2010). 3D seismic evidence of internal structure within Tampen Slide deposits on the North Sea Fan: are chaotic deposits that chaotic? *Journal of the Geological Society*, 167:605–616.

Gamboa, D. and Alves, T. M. (2016). Bi-modal deformation styles in confined mass-transport deposits: Examples from a salt minibasin in SE Brazil. *Marine Geology*, 379:176–193.

Gee, M. J., Gawthorpe, R. L., and Friedmann, J. S. (2005). Giant striations at the base of a submarine landslide. *Marine Geology*, 214(1-3):287–294.

Georgiopoulou, A., Masson, D. G., Wynn, R. B., and Krastel, S. (2010). Sahara slide: Age, initiation, and processes of a giant submarine slide. *Geochemistry, Geophysics, Geosystems*, 11(7).

Grilli, S. T., Tappin, D. R., Carey, S., Watt, S. F., Ward, S. N., Grilli, A. R., Engwell, S. L., Zhang, C., Kirby, J. T., Schambach, L., and Muin, M. (2019). Modelling of the tsunami from the December 22, 2018 lateral collapse of Anak Krakatau volcano in the Sunda Straits, Indonesia. *Scientific Reports*, 9(1):1–13.

Gross, F., Krastel, S., Chiocci, F. L., Ridente, D., Bialas, J., Schwab, J., Beier, J., Cukur, D., and Winkelmann, D. (2014). Evidence for submarine landslides offshore Mt. Etna, Italy. In Krastel, S., Behrmann, J. H., Völker, D. J., Stipp, M., Berndt, C., Urgeles, R., Chaytor, J. D., Huhn, K., Strasser, M., and Harbitz, C. B., editors, *Submarine Mass Movements and Their Consequences: Advances in Natural and Technological Hazards Research*, pages 307–316. Springer, Cham, 37 edition.

Gross, F., Mountjoy, J. J., Crutchley, G. J., Böttner, C., Koch, S., Bialas, J., Pecher, I., Woelz, S., Dannowski, A., Micallef, A., Huhn, K., and Krastel, S. (2018). Free gas distribution and basal shear zone development in a subaqueous landslide Insight from 3D seismic imaging of the Tuaheni Landslide Complex, New Zealand. *Earth and Planetary Science Letters*, 502:231–243.

Haflidason, H., Sejrup, H. P., Nygård, A., Mienert, J., Bryn, P., Lien, R., Forsberg, C. F., Berg, K., and Masson, D. (2004). The Storegga Slide: Architecture, geometry and slide development. *Marine Geology*, 213(1-4):201–234.

Hampton, M., Lee, H., and Locat, J. (1996). Submarine landslides. *Reviews of Geophysics*, 34(1):33–59.

Harbitz, C. B., Glimsdal, S., Løvholt, F., Kveldsvik, V., Pedersen, G. K., and Jensen, A. (2014a).

Rockslide tsunamis in complex fjords: From an unstable rock slope at Åkerneset to tsunami risk in western Norway. *Coastal Engineering*, 88:101–122.

Harbitz, C. B., Løvholt, F., and Bungum, H. (2014b). Submarine landslide tsunamis: how extreme and how likely? *Natural Hazards*, 72:1341–1374.

Harders, R., Kutterolf, S., Hensen, C., Moerz, T., and Brueckmann, W. (2010). Tephra layers: A controlling factor on submarine translational sliding? *Geochemistry, Geophysics, Geosystems*, 11(5):1–18.

Heezen, B. C. and Ewing, M. (1952). Turbidity currents and submarine slumps, and the 1929 Grand Banks Earthquake. *American Journal of Science*, 250:849–873.

Heijnen, M. S., Clare, M. A., Cartigny, M. J. B., Talling, P. J., Hage, S., Lintern, D. G., Stacey, C., Parsons, D. R., Simmons, S. M., Chen, Y., Sumner, E. J., Dix, J. K., and Hughes Clarke, J. E. (2020). Rapidly-migrating and internally-generated knickpoints can control submarine channel evolution. *Nature Communications*, 11(1):3129.

Hill, J. C., Brothers, D. S., Hornbach, M. J., Sawyer, D. E., Shillington, D. J., and Bécel, A. (2019). Subsurface controls on the development of the Cape Fear Slide Complex, central US Atlantic Margin. In Lintern, G., Mosher, D., Moscardelli, L., Bobrowsky, P., Campbell, C., Chaytor, J., Clague, J., Georgiopoulou, A., Lajeunesse, P., Normandeau, A., Piper, D., Scherwath, M., Stacey, C., and Turmel, D., editors, *Submarine Mass Movements and their Consequences*, pages 169–181. Geological Society of London Special Publications, London, 477 edition.

Hjelstuen, B. O., Eldholm, O., and Faleide, J. I. (2007). Recurrent Pleistocene mega-failures on the SW Barents Sea margin. *Earth and Planetary Science Letters*, 258:605–618.

Hornbach, M. J., Lavier, L. L., and Ruppel, C. D. (2007). Triggering mechanism and tsunamogenic potential of the Cape Fear Slide complex, U.S. Atlantic margin. *Geochemistry Geophysics Geosystems*, 8(12):1–16.

Hühnerbach, V. and Masson, D. G. (2004). Landslides in the North Atlantic and its adjacent seas: An analysis of their morphology, setting and behaviour. *Marine Geology*, 213(1-4):343–362.

Kane, I. A. and Clare, M. A. (2019). Dispersion, accumulation, and the ultimate fate of microplastics in deep-marine environments: A review and future directions. *Frontiers in Earth Science*, 7(80):1–27.

Korup, O., Clague, J. J., Hermanns, R. L., Hewitt, K., Strom, A., and Weidinger, J. (2007). Giant landslides, topography, and erosion. *Earth and Planetary Science Letters*, 261(3-4):578–589.

Kvalstad, T. J., Andresen, L., Forsberg, C. F., Berg, K., Bryn, P., and Wangen, M. (2005). The Storegga slide: Evaluation of triggering sources and slide mechanics. *Marine and Petroleum Geology*, 22(1-2):245–256.

Laberg, J. S. and Vorren, T. O. (2000). The Trænadjupet Slide, offshore Norway - Morphology, evacuation and triggering mechanisms. *Marine Geology*, 171(1-4):95–114.

Lastras, G., Canals, M., and Urgeles, R. (2003). Lessons from sea-floor and subsea-floor imagery of the BIG'95 debris flow scar and deposit. In Locat, J. and Mienert, J., editors, *Submarine Mass Movements and Their Consequences*, pages 425–431. Kluwer Acad., Dordrecht, Netherlands.

Lecours, V., Dolan, M. F., Micallef, A., and Lucieer, V. L. (2016). A review of marine geomorphometry, the quantitative study of the seafloor. *Hydrology and Earth System Sciences*, 20(8):3207–3244.

Lecours, V., Devillers, R., Simms, A. E., Lucieer, V. L., and Brown, C. J. (2017). Towards a framework for terrain attribute selection in environmental studies. *Environmental Modelling & Software*, 89:19–30.

Leynaud, D., Mienert, J., and Vanneste, M. (2009). Submarine mass movements on glaciated and non-glaciated European continental margins : A review of triggering mechanisms and preconditions to failure. *Marine and Petroleum Geology*, 26(5):618–632.

L'Heureux, J. S., Hansen, L., Longva, O., Emdal, A., and Grande, L. (2010). A multidisciplinary study of submarine landslides at the Nidelva fjord delta, Central Norway - Implications for geohazard assessment. *Norsk Geologisk Tidsskrift*, 90(1):1–20.

Li, W., Alves, T. M., Urlaub, M., Georgiopoulou, A., Klaucke, I., Wynn, R. B., Gross, F., Meyer, M., Repschläger, J., Berndt, C., and Krastel, S. (2017). Morphology, age and sediment dynamics of the upper headwall of the Sahara Slide Complex, Northwest Africa: Evidence for a large Late Holocene failure. *Marine Geology*, 393:109–123.

Locat, A., Jostad, H. P., and Leroueil, S. (2013). Numerical modeling of progressive failure and its implications for spreads in sensitive clays. *Canadian Geotechnical Journal*, 50(9):961–978.

Locat, J. and Lee, H. (2000). Submarine Landslides: Advances and Challenges. *Canadian Geotechnical Journal*, 39(1):193–212.

Locat, J., Leroueil, S., Locat, A., and Lee, H. (2014). Weak layers: their definition and classification from a geotechnical perspective. In Krastel, S., Behrmann, J.-H., Stipp, M., Völker, D., Urgeles, R., Berndt, C., Huhn, K., Chaytor, J., Harbitz, C. B., and Strasser, M., editors, *Submarine Mass Movements and Their Consequences: Advances in Natural and Technological Hazards Research*, pages 3–12. Springer, Cham, 37 edition.

Løvholt, F., Bondevik, S., Laberg, J. S., Kim, J., and Boylan, N. (2017). Some giant submarine landslides do not produce large tsunamis. *Geophysical Research Letters*, 44(16):8463–8472.

Masson, D. G., Hugget, Q., and Brunsden, D. (1993). The surface texture of the Saharan debris flow deposit and some speculation on submarine debris flow processes. *Sedimentology*, 40:583–598.

Masson, D. G., Wynn, R. B., and Talling, P. J. (2010). Large Landslides on Passive Continental Margins: Processes, Hypotheses and Outstanding Questions. In Mosher, D. C., Moscardelli, L., Shipp, R., Chaytor, J., Baxter, C., Lee, H., and Urgeles, R., editors, *Submarine Mass Movements and Their Consequences: Advances in Natural and Technological Hazards Research*, volume 28, pages 153–165. Springer, Dordrecht, Netherlands.

McGuire, W. (1996). Volcano instability: a review of contemporary themes. *Geological Society, London, Special Publications*, 110:1–23.

McGuire, W. (2003). Volcano instability and lateral collapse. *Revista*, 1:33–45.

Micallef, A., Berndt, C., Masson, D. G., and Stow, D. A. V. (2007a). A technique for the morphological characterization of submarine landscapes as exemplified by debris flows of the Storegga Slide. *Journal of Geophysical Research: Earth Surface*, 112(2):1–15.

Micallef, A., Masson, D. G., Berndt, C., and Stow, D. A. (2007b). Morphology and mechanics of submarine spreading: A case study from the Storegga Slide. *Journal of Geophysical Research: Earth Surface*, 112(3):1–21.

Moernaut, J., Van Daele, M., Heirman, K., Wiemer, G., Molenaar, A., Vandorpe, T., Melnick, D., Hajdas, I., Pino, M., Urrutia, R., and De Batist, M. (2019). The subaqueous landslide cycle in south-central Chilean lakes: The role of tephra, slope gradient and repeated seismic shaking. *Sedimentary Geology*, 381:84–105.

Moore, J. G., Clague, D. A., Holcomb, R. T., Lipman, P. W., Normark, W. R., and Torresan, M. E. (1989). Prodigious submarine landslides on the Hawaiian Ridge. *Journal of Geophysical Research*, 94(B12):17465.

Moscardelli, L. and Wood, L. (2008). New classification system for mass transport complexes in offshore Trinidad. *Basin Research*, 20(1):73–98.

Moscardelli, L. and Wood, L. (2016). Morphometry of mass-transport deposits as a predictive tool. *Bulletin of the Geological Society of America*, 128(1-2):47–80.

Mosher, D. C., Laberg, J. S., and Murphy, A. (2016). The role of submarine landslides in the Law of the Sea. In Lamarche, G., Mountjoy, J., Bull, S., Hubble, T., Krastel, S., Lane, E., Micallef, A., Moscardelli, L., Mueller, C., Pecher, I., and Woelz, S., editors, *Submarine Mass Movements and Their Consequences: Advances in Natural and Technological Hazards Research*, pages 15–26. Springer, Cham, Switzerland, 41 edition.

Mountjoy, J. and Micallef, A. (2018). Submarine Landslides. In Micallef, A., Krastel, S., and Savini, A., editors, *Submarine Geomorphology*, pages 235–250. Springer Geology, Cham, Switzerland.

Muhari, A., Heidarzadeh, M., Susmoro, H., Nugroho, H. D., Kriswati, E., Supartoyo, Wijanarto, A. B., Imamura, F., and Arikawa, T. (2019). The December 2018 Anak Krakatau Volcano Tsunami as Inferred from Post-Tsunami Field Surveys and Spectral Analysis. *Pure and Applied Geophysics*, 176(12):5219–5233.

Mulder, T. and Alexander, J. (2001). The physical character of subaqueous sedimentary density flow and their deposits. *Sedimentology*, 48(2):269–299.

Murray, J. and Voigt, B. (1996). Slope stability and eruption prediction on the eastern flank of Mount Etna. *Geological Society, London, Special Publications*, 110:111–114.

Nakata, K., Katsumata, A., and Muhari, A. (2020). Submarine landslide source models consistent with multiple tsunami records of the 2018 Palu tsunami, Sulawesi, Indonesia. *Earth, Planets and Space*, 72(44):1–16.

Nardin, T., Hein, F., Gorsline, D., and Edwards, B. (1979). A review of mass movement processes, sediment, andacoustic c haracteristics and contrasts in slope and base- of-slope systems versus canyon-fan-basin floor system. *Society of Economic Paleontologists and Mineralogists - Special Publications*, 27:61–73.

Nisbet, E. G. and Piper, D. J. W. (1998). Giant submarine landslides. *Nature*, 392(6674):329–330.

Normandeau, A., Campbell, D. C., Piper, D. J., and Jenner, K. A. (2019). New evidence for a major Late Quaternary submarine landslide on the external western levee of the Laurentian fan. In Lintern, G., Mosher, D., Moscardelli, L., Bobrowsky, P., Campbell, C., Chaytor, J., Clague, J., Georgiopoulou, A., Lajeunesse, P., Normandeau, A., Piper, D., Scherwath, M., Stacey, C., and Turmel, D., editors, *Subaqueous Mass Movements and Their Consequences: Assessing Geohazards, Environmental Implications and Economic Significance of Subaqueous Landslides*, volume 477, pages 377–387. Geological Society of London Special Publications, London.

Nygård, A., Sejrup, H. P., Haflidason, H., and Bryn, P. (2005). The glacial North Sea Fan, southern

Norwegian Margin: Architecture and evolution from the upper continental slope to the deep-sea basin. *Marine and Petroleum Geology*, 22(1-2):71–84.

Obelcz, J., Xu, K., Georgiou, I. Y., Maloney, J., Bentley, S. J., and Miner, M. D. (2017). Subdecadal submarine landslides are important drivers of deltaic sediment flux : Insights from the Mississippi River Delta Front. *Geology*, 45(8):703–706.

Obelcz, J., Wood, W. T., Phrampus, B. J., and Lee, T. R. (2020). Machine Learning Augmented Time-Lapse Bathymetric Surveys: A Case Study From the Mississippi River Delta Front. *Geophysical Research Letters*, 47(10).

Okey, T. A. (1997). Sediment flushing observations, earthquake slumping, and benthic community changes in Monterey Canyon head. *Continental Shelf Research*, 17(8):877–897.

Omira, R., Dogan, G. G., Hidayat, R., Husrin, S., Prasetya, G., Annunziato, A., Proietti, C., Probst, P., Paparo, M. A., Wronna, M., Zaytsev, A., Pronin, P., Giniyatullin, A., Putra, P. S., Hartanto, D., Ginanjar, G., Kongko, W., Pelinovsky, E., and Yalciner, A. C. (2019). The September 28th, 2018, Tsunami In Palu-Sulawesi, Indonesia: A Post-Event Field Survey. *Pure and Applied Geophysics*, 176(4):1379–1395.

Panieri, G., Camerlenghi, A., Cacho, I., Cervera, C. S., Canals, M., Lafuerza, S., and Herrera, G. (2012). Tracing seafloor methane emissions with benthic foraminifera: Results from the Ana submarine landslide (Eivissa Channel, Western Mediterranean Sea). *Marine Geology*, 291-294:97–112.

Paull, C. K., Talling, P. J., Maier, K. L., Parsons, D., Xu, J., Caress, D. W., Gwiazda, R., Lundsten, E. M., Anderson, K., Barry, J. P., Chaffey, M., O'Reilly, T., Rosenberger, K. J., Gales, J. A., Kieft, B., McGann, M., Simmons, S. M., McCann, M., Sumner, E. J., Clare, M. A., and Cartigny, M. J. (2018). Powerful turbidity currents driven by dense basal layers. *Nature Communications*, 9(1):1–9.

Prior, D. B., Bornhold, B., and Johns, M. (1984). Depositional characteristics of a submarine debris flow. *Journal of Geology*, 92:707–727.

Ramalho, R. S., Winckler, G., Madeira, J., Helffrich, G. R., Hipólito, A., Quartau, R., Adena, K., and Schaefer, J. M. (2015). Hazard potential of volcanic flank collapses raised by new megatsunami evidence. *Science Advances*, 1(9):1–11.

Sammartini, M., Moernaut, J., Anselmetti, F. S., Hilbe, M., Lindhorst, K., Praet, N., and Strasser, M. (2019). An atlas of mass transport deposits in lakes. *Geophysical Monograph Series*, 246:201–226.

Savini, A., Marchese, F., Verdicchio, G., and Vertino, A. (2016). Submarine Slide Topography and the Distribution of Vulnerable Marine Ecosystems: A Case Study in the Ionian Sea (Eastern Mediterranean). In Lamarche, G., Mountjoy, J., Bull, S., Hubble, T., Krastel, S., Lane, E., Micallef, A., Moscardelli, L., Mueller, C., Pecher, I., and Woelz, S., editors, *Submarine Mass Movements and Their Consequences: Advances in Natural and Technological Hazards Research*. Springer, Cham, Switzerland, 41 edition.

Schnellmann, M., Anselmetti, F. S., Giardini, D., and McKenzie, J. A. (2005). Mass movement-induced fold-and-thrust belt structures in unconsolidated sediments in Lake Lucerne (Switzerland). *Sedimentology*, 52(2):271–289.

Shanmugam, G. (2000). 50 years of the turbidite paradigm (1950s-1990s): Deep-water processes and facies models – a critical perspective. *Marine and Petroleum Geology*, 17:285–342.

Siebert, L. (1984). Large volcanic debris avalanches: characteristics of source areas, deposits, and associated eruptions. *Journal of Volcanology and Geothermal Research*, 22:163–197.

Solheim, A., Bryn, P., Berg, K., Sejrup, H. P., and Mienert, J. (2005). *Ormen Lange – an Integrated Study for Safe Field Development in the Storegga Submarine Area*. Elsevier Science.

Talling, P. J., Masson, D. G., Sumner, E. J., and Malgesini, G. (2012). Subaqueous sediment density flows: Depositional processes and deposit types. *Sedimentology*, 59(7):1937–2003.

Talling, P. J., Paull, C. K., and Piper, D. J. (2013). How are subaqueous sediment density flows triggered, what is their internal structure and how does it evolve? Direct observations from monitoring of active flows. *Earth-Science Reviews*, 125:244–287.

Teide Group (1997). Morphometric interpretation of the northwest and southeast slopes of Tenetire, Canary Islands. *Journal of Geophysical Research*, 102(B9):20,325–20,342.

Tibaldi, A., Pasquarè, F., Papanikolaou, D., and Nomikou, P. (2008). Discovery of a huge sector collapse at the Nisyros volcano, Greece, by on-land and offshore geological-structural data. *Journal of Volcanology and Geothermal Research*, 177:485–499.

Urlaub, M., Talling, P. J., Zervos, A., and Masson, D. G. (2015). What causes large submarine landslides on low gradient sediment accumulation? *Journal of Geophysical Research: Solid Earth*, 120:1–18.

Urlaub, M., Geersen, J., Krastel, S., and Schwenk, T. (2018a). Diatom ooze: Crucial for the generation of submarine mega-slides? *Geological Society of America*, 46(4):331–334.

Urlaub, M., Petersen, F., Gross, F., Bonforte, A., Puglisi, G., Guglielmino, F., Krastel, S., Lange, D., and Kopp, H. (2018b). Gravitational collapse of Mount Etna's southeastern flank. *Science Advances*, 4(10):1–8.

Vanneste, M., Mienert, J., and Bünz, S. (2006). The Hinlopen Slide: A giant, submarine slope failure on the northern Svalbard margin, Arctic Ocean. *Earth and Planetary Science Letters*, 245(1-2):373–388.

Watts, A. B. and Masson, D. G. (1995). A giant landslide on the north flank of Tenerife, Canary Islands. *Journal of Geophysical Resarch*, 100(B12):24,487–24,498.

Webb, B. C. and Cooper, A. H. (1988). Slump folds and gravity slide structures in a Lower Palaeozoic marginal basin sequence (the Skiddaw group), NW England. *Journal of Structural Geology*, 10(5):463–472.

Weimer, P., Slatt, R. M., and Bouroullec, R. (2007). Introduction to the petroleum geology of deepwater settings. *AAPG Studies in Geology*, 57:419–455.

Weninger, B., Schulting, R., Bradtmöller, M., Clare, L., Collard, M., Edinborough, K., Hilpert, J., Jöris, O., Niekus, M., Rohling, E., and Wagner, B. (2008). The catastrophic final flooding of Doggerland by the Storegga Slide tsunami. *Documenta Praehistorica*, 35:1–24.

Winkelmann, D., Geissler, W., Schneider, J., and Stein, R. (2008). Dynamics and timing of the Hinlopen/Yermak Megaslide north of Spitsbergen, Arctic Ocean. *Marine Geology*, 250(1-2):34–50.

Zengaffinen, T., Løvholt, F., Pedersen, G. K., and Muhari, A. (2020). Modelling 2018 Anak Krakatoa Flank Collapse and Tsunami: Effect of Landslide Failure Mechanism and Dynamics on Tsunami Generation. *Pure and Applied Geophysics*, 177(6):2493–2516.

Chapter 3

Revisiting the tsunamigenic volcanic flank collapse of Fogo Island in the Cape Verdes, offshore West Africa

Manuscript I

Published as:

Rachel Barrett, Elodie Lebas, Ricardo Ramalho, Ingo Klaucke, Steffen Kutterolf, Andreas Klügel, Katja Lindhorst, Felix Gross, and Sebastian Krastel (2019). Revisiting the tsunamigenic volcanic flank collapse of Fogo Island in the Cape Verdes, offshore West Africa. *In* Geological Society of London Special Publications, 500, https://doi.org/10.1144/SP500-2019-187.

Abstract

Volcanic archipelagos are a source of numerous on- and offshore geohazards, including explosive eruptions and potentially tsunamigenic large-scale flank-collapses. Fogo Island in the southern Cape Verdes is one of the most active volcanoes in the world, making it both prone to collapse (as evidenced by the ca. 73 ka Monte Amarelo volcanic flank-collapse), and a source of widely-distributed tephra and volcanic material. The offshore distribution of the Monte Amarelo debris avalanche deposits and the surrounding volcaniclastic apron were previously mapped using only medium-resolution bathymetric data. Here, using recently acquired, higher resolution acoustic data, we revisit Fogo's flank-collapse, and find evidence suggesting that the deposition of hummocky volcanic debris originating from the failed eastern flank most likely triggered the contemporaneous, multi-phase failure of pre-existing seafloor sediments. Additionally, we identify, for the first time, multiple mass-transport deposits in the southern part of the volcaniclastic apron of Fogo and Santiago based on the presence of acoustically chaotic deposits in parametric echo sounder data and volcaniclastic turbiditic sands in recovered cores. These preliminary findings indicate a long and complex history of instability on the southern slopes of Fogo and suggest that Fogo may have experienced multiple flank- collapses.

3.1 Introduction

Volcanic archipelagos are home to numerous on- and offshore hazards such as changes in sea level, storms, volcanic eruptions, slope instabilities, large flank-collapses, and tsunamis (Casalbore, 2018). These events can have devastating consequences for people, nature, and infrastructure, both onshore and offshore. A variety of internal and external factors can precondition and trigger flank instabilities. These include dyke and sill intrusions; volcanic eruptions and tremor; earthquakes; flank over-steepening; the weight of new volcanic material on the island flanks; weakening of the volcanic edifice by weathering and hydrothermal activity; and, for smaller landslides, by the effects of wave, wind and storm activity (e.g. Siebert, 1984, Begét and Kienle, 1992, Murray and Voigt, 1996, McGuire, 1996, 2003, Tibaldi, 2001, Cervelli et al., 2002, Casalbore et al., 2011, 2015, Gross et al., 2014, Clare et al., 2018). Such factors occur over timescales ranging from seconds to thousands of years, and are globally widespread (McGuire, 1996, Blahut et al., 2019).

The volume of volcanic flank-collapses varies significantly, but can be as large as thousands of cubic kilometres, e.g. in the Hawaiian archipelago (Moore et al., 1989). Many such events have volumes in the order of tens to hundreds of cubic kilometres, e.g. at Nisyros Volcano in

the Aegean Sea (Tibaldi et al., 2008, Livanos et al., 2013); in the Lesser Antilles Arc (Lebas et al., 2011, Le Friant et al., 2015, Brunet et al., 2016); in the Canary Islands (Krastel et al., 2001, Masson et al., 2002, León et al., 2017); and in the Cape Verde Islands (Masson et al., 2008). However, even comparatively small-volume volcanic flank-collapses, such as the 0.22-0.3 km^3 Anak Krakatau flank-collapse in December 2018 (Grilli et al., 2019), may result in catastrophic tsunamis. The hazard potential of such flank-collapses is widely recognized, but the magnitude, and therefore hazard potential, of the tsunamis that can be triggered by flank-collapses is heavily debated (e.g. Moore and Moore, 1984, Goff et al., 2014, McMurtry et al., 2004, Watt et al., 2012b, Ramalho et al., 2015, Paris et al., 2018).

Other factors that can contribute to the instability of slopes offshore are the deposition of centi- to decimetre-thick discrete layers of volcanic ash across a wide region and the presence of buried turbidites in the volcanic apron. Studies in lacustrine settings (e.g. Wiemer et al., 2015, Moernaut et al., 2019) and on active offshore margins (e.g. Harders et al., 2010, Lafuerza et al., 2014, Hornbach et al., 2015, Kuhlmann et al., 2016, Sammartini et al., 2018) have indicated a relationship between tephra layers or turbidites and slide failure planes. Although the exact nature of this relationship is disputed (Wiemer and Kopf, 2016), it is thought that tephra could behave as *weak layers* - layers of inherently lower strength than adjacent layers, which are thereby prone to failure (Locat et al., 2014). Using core logging, sedimentological, and geotechnical data from the IODP Expedition 340, Lafuerza et al. (2014) showed that low hydraulic conductivity of hemipelagic sediments offshore Martinique (Lesser Antilles) could cause low rates of dewatering in turbidites and tephra layers, allowing excess pore fluid pressures to persist at depth. Moreover, Hornbach et al. (2015) suggested that even small changes in the stress regime of these layers, such as that resulting from regional strain and grain reorganization during the compaction of sediments, might trigger motion. Effectively, results from IODP 340 showed that sand layers (i.e. tephra ash and turbidites), as well as boundaries between sand and mud layers, may act as multiple decollement surfaces that promote and enhance the mobility of landslide deposits (Le Friant et al., 2015).

3.1.1 Geological Setting

The Cape Verdes archipelago, offshore West Africa (Figure 3.1), is the surface expression of a mantle hotspot (Crough, 1978, Holm et al., 2008, Ramalho et al., 2010). The island of Fogo, in the southern part of the archipelago, is one of the most active oceanic intraplate volcanoes in the world, having erupted 28 times in the last 520 years (Ribeiro, 1960, Torres et al., 1997, González et al., 2015). Such volcanically active areas are well known to be associated with seismicity and the southern Cape Verdes are no different, recording frequent

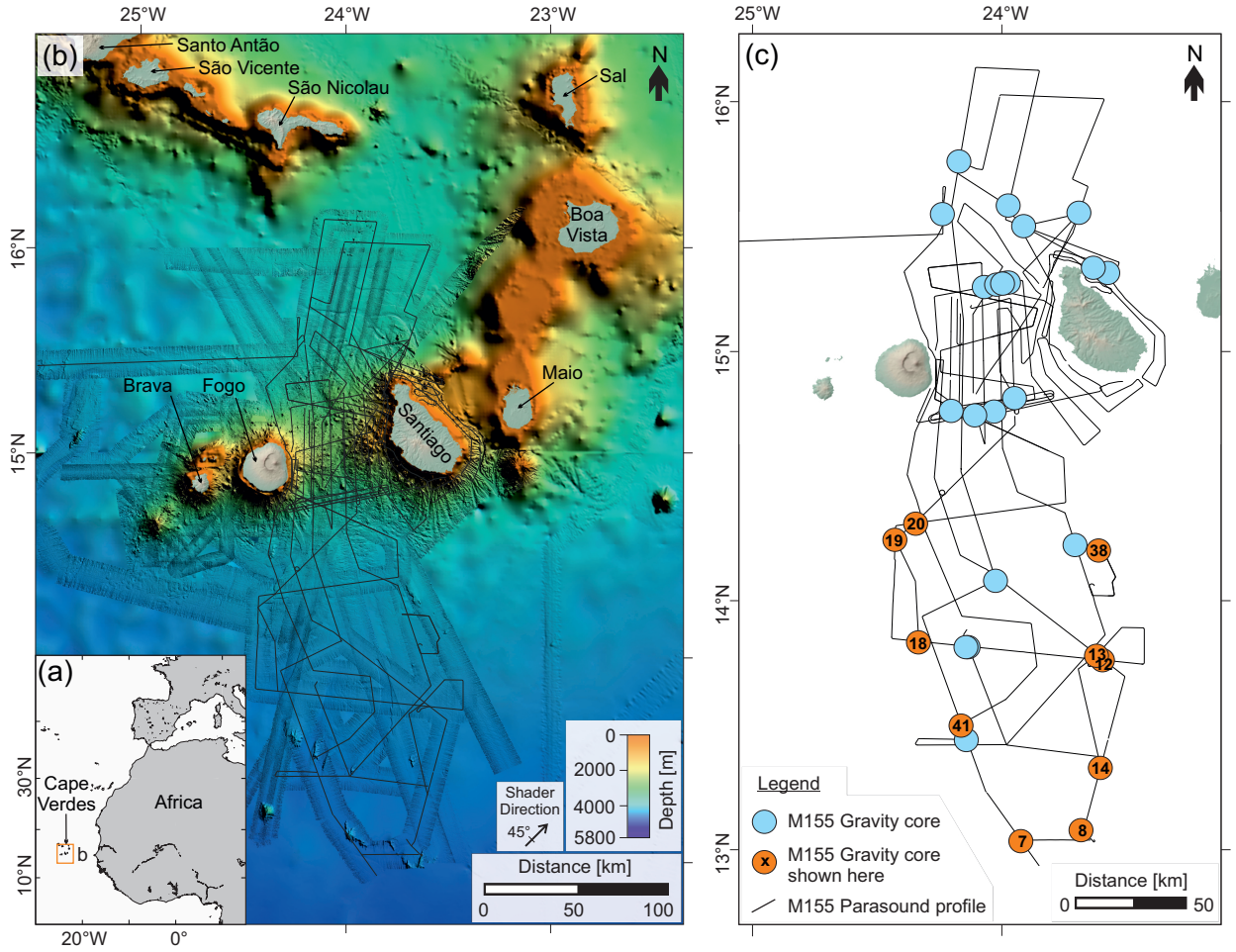

Figure 3.1: (a) Location of the Cape Verdes offshore West Africa. Box outlines the region presented in b. (b) Multibeam bathymetric data collected during R/V Meteor cruises M155 and M80/3 overlain on GEBCO2019 (British Oceanographic Data Centre, www.gebco.net) bathymetry of the southern Cape Verdean archipelago. Black lines show the locations of Parasound profiles collected during cruise M155 of R/V Meteor. (c) Location of the newly acquired Parasound data and of the gravity cores collected during cruise M155.

volcano-tectonic earthquakes (Grevemeyer et al., 2010, Faria and Fonseca, 2014, Vales et al., 2014). Sediment cores collected in the region provide evidence of at least 43 large, explosive eruptions in the area in the last 150 kyr (Eisele et al., 2015), attesting to Fogo's vigorous volcanic activity. Such frequent volcanic activity, along with the accumulation of volcanic deposits on the submarine flanks, means that Fogo's flanks are potentially unstable and prone to collapsing.

An up-to-1 km high, semi-circular depression (Bordeira), open to the east on central Fogo, was interpreted by Day et al. (1999) as the scar of a large flank-collapse, referred to as "Monte Amarelo" (Figure 3.2). Other authors, however, interpret the same morphology as two partially overlapping volcanic calderas that were later cut by a flank-collapse that affected the eastern portion of the edifice (Torres et al., 1997, Brum da Silveira et al.,

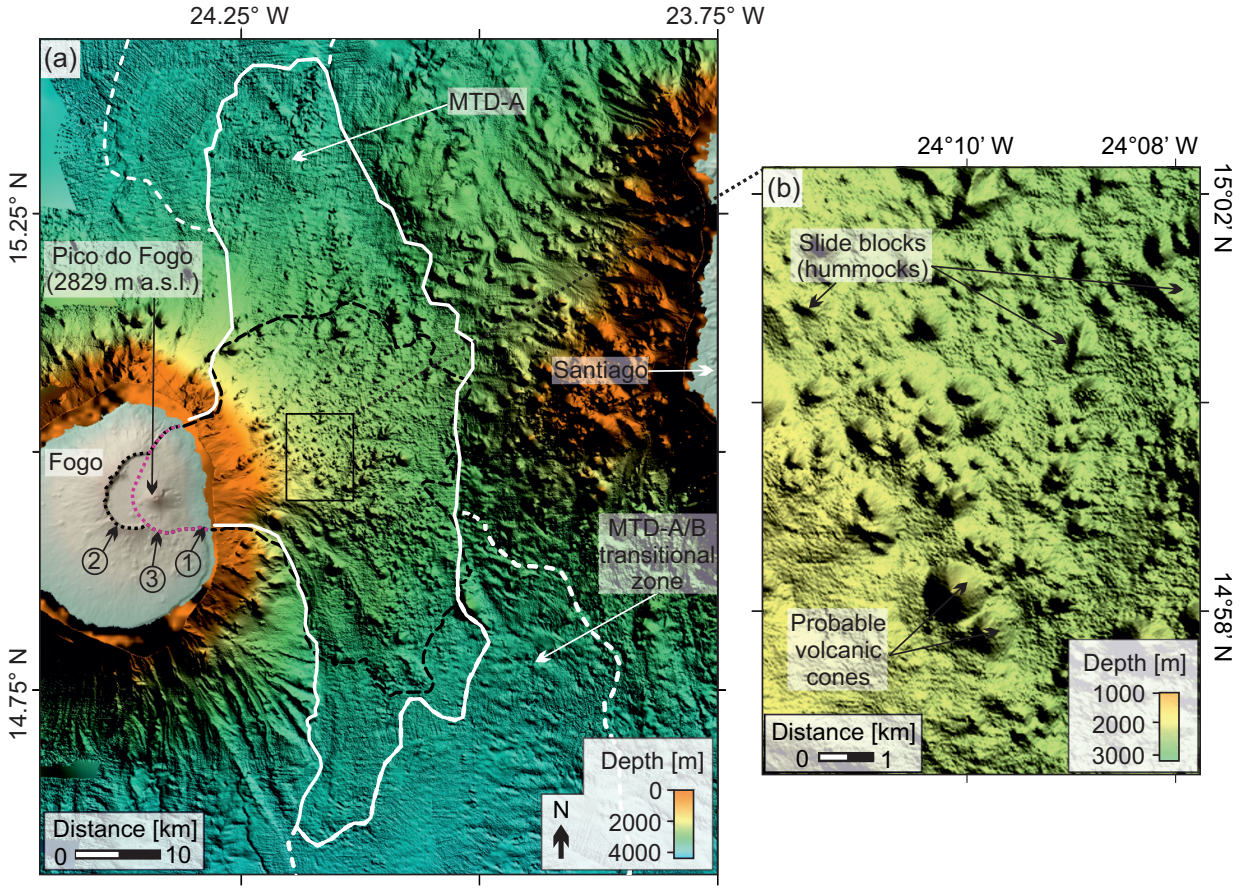

Figure 3.2: High-resolution, multibeam bathymetry data highlighting the hummocky nature of the Monte Amarelo debris avalanche deposits (MTD-A) proximal to Fogo. (a) Compilation of the M155 and M80/3 multibeam bathymetry data overlain on GEBCO2019 bathymetry and DEM topography of Fogo Island. (1) Espigo escarpment; (2) Bordeira escarpment (dotted black line) is regarded as either the Monte Amarelo headwall scarp (Day et al., 1999), or the edge of a caldera (Madeira et al., 2008, Martínez-Moreno et al., 2018); (3) Monte Amarelo headwall scarp (dotted pink line, Madeira et al., 2008, Martínez-Moreno et al., 2018); dashed black line: previously estimated extent of the Monte Amarelo debris avalanche deposits (Masson et al., 2008); solid white line: revised extent of the Monte Amarelo debris avalanche deposits (MTD-A); dashed white line: transitional zone where the size of the hummocks decreases with distance from the source. (b) Enlarged view of the hummocky topography of the Monte Amarelo debris avalanche deposits. Note the angular shape and variable size of the hummocks.

1997, Madeira et al., 2008, Martínez-Moreno et al., 2018). Fogo's Monte Amarelo flank-collapse, however, is strongly supported by the presence of a preserved lateral ramp at Espigao (Brum da Silveira et al., 1997), and a debris avalanche deposit located between the islands of Fogo and Santiago (Le Bas et al., 2007, Masson et al., 2008) (Figures 3.2, 3.3). Using a combined magnetotelluric- and multibeam-based approach, Martínez-Moreno et al. (2018) estimated a volume of 110 km^3 for the Monte Amarelo debris avalanche deposit. This estimate corresponds well with previous bathymetric-based estimates, which ranged between 80 and 160 km^3 (Le Bas et al., 2007, Madeira et al., 2008, Masson et al., 2008).

Tsunami deposits found on the nearby islands of Santiago and Maio indicate that the Monte Amarelo flank-collapse was tsunamigenic, with the resulting tsunami achieving a run-up in excess of 270 m above coeval sea level on Santiago (Ramalho et al., 2015, Madeira et al., 2019). The exact age of the collapse, however, is the topic of ongoing debate. On the basis of 3He geochronology of lava flows from Fogo, Foeken et al. (2009) first estimated the collapse to have occurred between 62 and 123 ka. Paris et al. (2011) suggested a narrower window of 86 to 124 ka, based, respectively, on Ar/Ar ages of lava flows from Fogo thought to be post-collapse, and U-Th dating of corals from tsunami deposits on Santiago. More recently, based on the results of cosmogenic 3He dating of tsunami megaclasts from Santiago Island, Ramalho et al. (2015) proposed that the collapse and ensuing tsunami took place between 65 and 84 ka, with a most probable age of 73 $\pm$ 7 ka. This agrees, within uncertainty, with the age recently reported by Madeira et al. (2019, 78 $\pm$ 0.9 ka) for a set of tsunami deposits found on the coast of Maio Island. Dating of turbidite material attributed to tsunami-triggered sediment transport along the flanks of Fogo and Brava islands, however, led Eisele et al. (2015) to favour an older age of 86-117 ka. Finally, and most recently, Marques et al. (2019) suggested a much younger age of 43-59 ka, based on K/Ar dating of Fogo lava flows that they considered to be pre- and post-collapse.

Whether Fogo has collapsed only once or multiple times is also the subject of discussion (Day et al., 1999, Ramalho et al., 2015, Martínez-Moreno et al., 2018, Marques et al., 2019). Subsequent eruptions on Fogo have largely been constrained to the central and eastern parts of the island, and a prominent stratovolcano - Pico do Fogo - presently rises to 2829 m above sea level within the landslide scar (Figure 3.2, Torres et al., 1997).

3.1.2 Objectives

A detailed analysis of the distribution of the landslide deposits and failure mechanism are critical for constraining the hazard linked to the collapse of a volcanic flank. Moreover, this characterization is crucial for tsunami hazard modelling, given that the mode, volume and run-out of a collapse will have a profound effect on the resulting tsunami waves (Grilli et al., 1997, Abadie et al., 2012, Watt et al., 2012b). The offshore distribution of the Monte Amarelo flank-collapse debris (i.e. debris avalanche deposits) and the surrounding volcaniclastic apron were previously mapped using only medium-resolution (100 m grid cell size) multibeam bathymetric data (Masson et al., 2008). Consequently, the distribution of the debris avalanche deposits, and of any additional slope instabilities in the area, are still poorly constrained. As Fogo's volcanic flank-collapse likely triggered a megatsunami with a recognizable impact on the adjacent islands' coastlines (Paris et al., 2011, 2018, Ramalho et al., 2015, Madeira et al., 2019), a full characterization of this landslide and its related

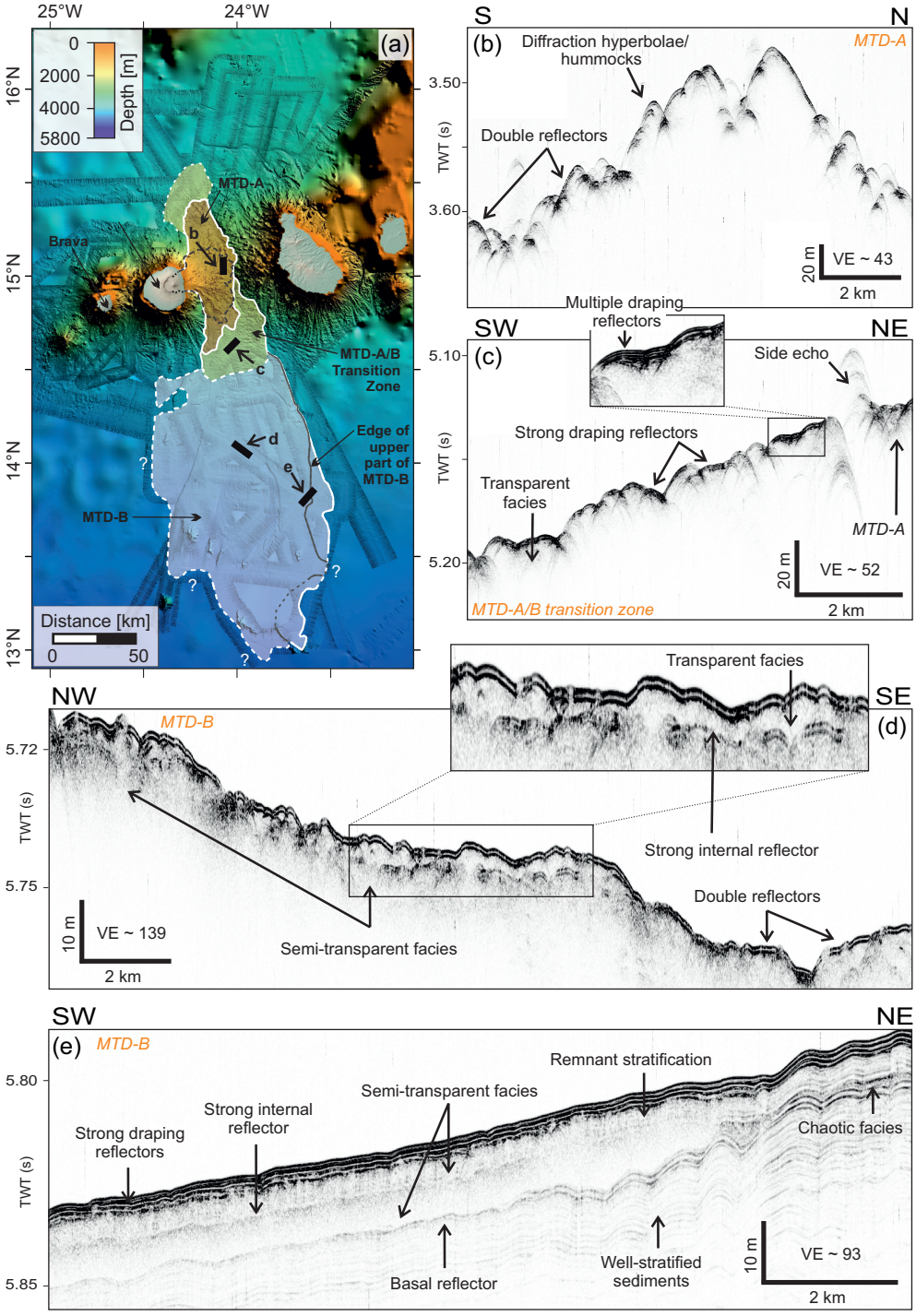

Figure 3.3: Map showing the distribution of the debris avalanche deposits (MTD-A), the acoustically transparent/seismically chaotic MTD-B associated with the Monte Amarelo flank-collapse, and a transitional zone where the size of the hummocks decreases with distance from the source. The lateral extent of MTD-B may extend further south and west of the surveyed area. Dashed black line: previous mapped extent of the Monte Amarelo deposits (Masson et al., 2008); Grey line: eastern margin of the upper part of MTD-B. Solid black lines: location of the Parasound lines shown in (b) to (e). (b-e) Parasound profiles highlighting the acoustic character of (b) MTD-A, (c) the transitional zone, and (d-e) MTD-B. See the text for discussion on the nature of these deposits.

volume is crucial for improving numerical models of tsunami generation, propagation and inundation, and for constraining the hazard potential associated with large, tsunamigenic volcanic flank-collapses.

Here, using recently acquired multibeam bathymetric data (50 m grid cell size) in conjunction with parametric sediment echo-sounder data and sediment gravity cores, we revisit the Monte Amarelo volcanic flank-collapse and consider general slope stability in the southern distal region of the volcanic apron. We aim to (i) map out the lateral extent and characterise the acoustic nature of the Monte Amarelo debris avalanche deposits; (ii) identify possible additional landslides on the slopes south of the islands of Fogo and Santiago; and (iii) consider the related preconditioning and triggering processes.

3.2 Data and methodology

The data presented in this paper were collected during R/V Meteor cruise M155 (May - June 2019; Krastel et al., 2019) and are supplemented by multibeam bathymetric data collected during R/V Meteor cruise M80/3 (Hansteen et al., 2014). The bathymetric data from both cruises were acquired using hull-mounted Kongsberg EM120 (M80/3), EM122 (M155) and EM710 (M155) multibeam echo-sounders. The EM120/EM122 system has a swath coverage of up to 150° and a nominal sonar frequency of 12 kHz, and is designed to perform seabed mapping to full ocean depth. During cruise M155, the swath width was reduced to 120° in order to increase the quality and resolution of the data. The EM710 system has a swath coverage of up to 140°, and a nominal sonar frequency of 70 to 100 kHz. As such, the EM710 was only used in water depths less than 700 m close to the islands of Fogo and Santiago. All bathymetric data were filtered for outliers and manually edited. The data from all cruises and multibeam systems are combined and gridded at 50 m.

Parametric sediment echo-sounder data were collected using a parametric ATLAS DS-3/P70 system (Parasound). This system has an opening angle of 4° and operates at primary high frequencies of 18.5 kHz and 22.5 kHz, resulting in a parametric low frequency of 4 kHz. The vertical resolution of this system is in the decimeter range. All depth scales on Parasound images presented in this study were calculated using a constant velocity of 1500 m/s.

Sediment cores were collected during cruise M155 using a gravity corer with tube lengths of 3 to 15 m. These cores were visually described onboard, and smear slides were analyzed to obtain further microscopic information about the core mineralogy, texture and composition. Dating and further geochemical and sedimentological analysis of these cores is ongoing and will form the basis of future work on the subject.

3.3 Results

3.3.1 The Monte Amarelo debris avalanche deposits (MTD-A)

The Monte Amarelo deposits proximal to Fogo (MTD-A; distribution shown in Figure 3.3a) are characterized by overlapping diffraction hyperbolae (Figure 3.3b). This hummocky character is typical of debris avalanche deposits from volcanic flank-collapses (Siebert, 1984). The sedimentary drape covering MTD-A is relatively thin (<1.5 m thick) or not imaged, and is often characterized by two strong, positive reflections. Irregularly shaped blocks that are up to 100 m higher than the surrounding seafloor are present within the landslide debris (Figure 3.2). Further away from Fogo, the hummocky topography is less prevalent in the bathymetric data, despite the presence of diffraction hyperbolae in the Parasound data. This highlights a decrease in the size of the hummocks with distance from the island. We note a progressive transition in the acoustic signature of the deposits from a hyperbolic facies with metre-scale acoustic penetration (Figure 3.3b), to a mounded facies draped by ∼1.5 m of sediment characterized by the aforementioned prominent double reflections (Figure 3.3d). In a few places, these double reflections are replaced by a succession of finely stratified layers (inset of Figure 3.3c).

3.3.2 Distal deposits related to the Monte Amarelo volcanic flank-collapse (MTD-B)

Southwards, with increasing distance from Fogo, the acoustic character of the Monte Amarelo deposits changes from being hyperbolae-dominated to being characterised by an acoustically transparent/semi-transparent facies (Figure 3.3d; hereafter referred to as MTD-B; distribution shown in Figure 3.3a). In the northern reaches of MTD-B, the upper surface of the deposits is undulating, with metre-scale variations in depth over wavelengths of tens to hundreds of metres (Figure 3.3d). The overlying sedimentary drape mantles the surface of the deposits and a strong internal reflector is imaged in places within the deposits (Figure 3.3d). This internal reflector clearly contrasts with the overlying transparent facies, separating it from the lower semi-transparent facies. In the northern and western reaches of MTD-B, this internal reflector is either clearly imaged or not present at all, and the base of the lower part of MTD-B is not resolved (Figure 3.3d).

In the eastern and southern reaches of MTD-B, the aforementioned internal reflector is continuous over a relatively long distance (Figure 3.3e). In these areas, a thicker sedimentary drape (up to ∼4 m thick), containing multiple strong reflections alternating with relatively

thin, transparent layers, overlies MTD-B. The upper surface of MTD-B is diffuse and undulating in parts. The base of MTD-B is marked by a prominent reflection that has a similar acoustic signature, although of lower amplitude, as the double reflector that overlies the deposits. A series of well-stratified sediments is imaged below the base of MTD-B (Figure 3.3e). At the eastern lateral margin of MTD-B, the internal reflector within the slide deposits is more diffuse (Figure 3.3e). The lowermost part of MTD-B remains transparent in nature, but remnant stratifications are imaged in some areas of the uppermost part. The eastern boundary is gradational over two to three km, and is marked by a progressive thinning of the transparent facies, and an increase in stratification within the deposits (Figure 3.3e).

Constraining the thickness and lateral extent of MTD-B is challenging. In the northern reaches, where the strong internal reflector is imaged, the base of the deposits is not resolved by the acoustic system (Figure 3.3c). This means that only the thickness of the upper transparent facies related to MTD-B (up to ∼7 m thick, but variable) can be estimated. In its eastern and southern extents, however, the bases of the upper and lower units of MTD-B are imaged, leading to thickness estimates of 4-6 m and 5-15 m for the upper and lower units, respectively (Figure 3.3e). The large spacings between the Parasound profiles in the central and southern parts of the working area, south of Fogo and Santiago, mean that we cannot constrain the thickness of the deposits in these areas with certainty. In addition, MTD-B deposits might extend beyond the limits of the surveyed area, especially to the west and south (Figure 3.3a).

3.3.3 Additional mass wasting events on the shallow slopes south of Fogo and Santiago

Visual analysis of gravity cores taken in the southern part of the volcaniclastic apron of Fogo and Santiago reveals mud- and nanofossil-rich facies interbedded with multiple sand units that are defined by parallel and cross-laminated, seldom normally-graded beds (Figure 3.4). These sandy intervals generally range from fine to coarse sand deposits, and are typically of centi- to decimetre scale (Figure 3.4b). Microscopic analyses show that these shallow sandy turbidites are predominantly of volcaniclastic (volcanic lithics that are mostly lava fragments, tachylitic to brown glass, crystal fragments), and/or mixed volcaniclastic-bioclastic composition, rather than solely bioclastic.

Multibeam-bathymetry and sediment echo-sounder data on the shallow slopes south of Fogo and Santiago reveal multiple morphological steps and several mass transport deposits (MTDs; Figure 3.5). These additional MTDs are characterized by acoustically transparent

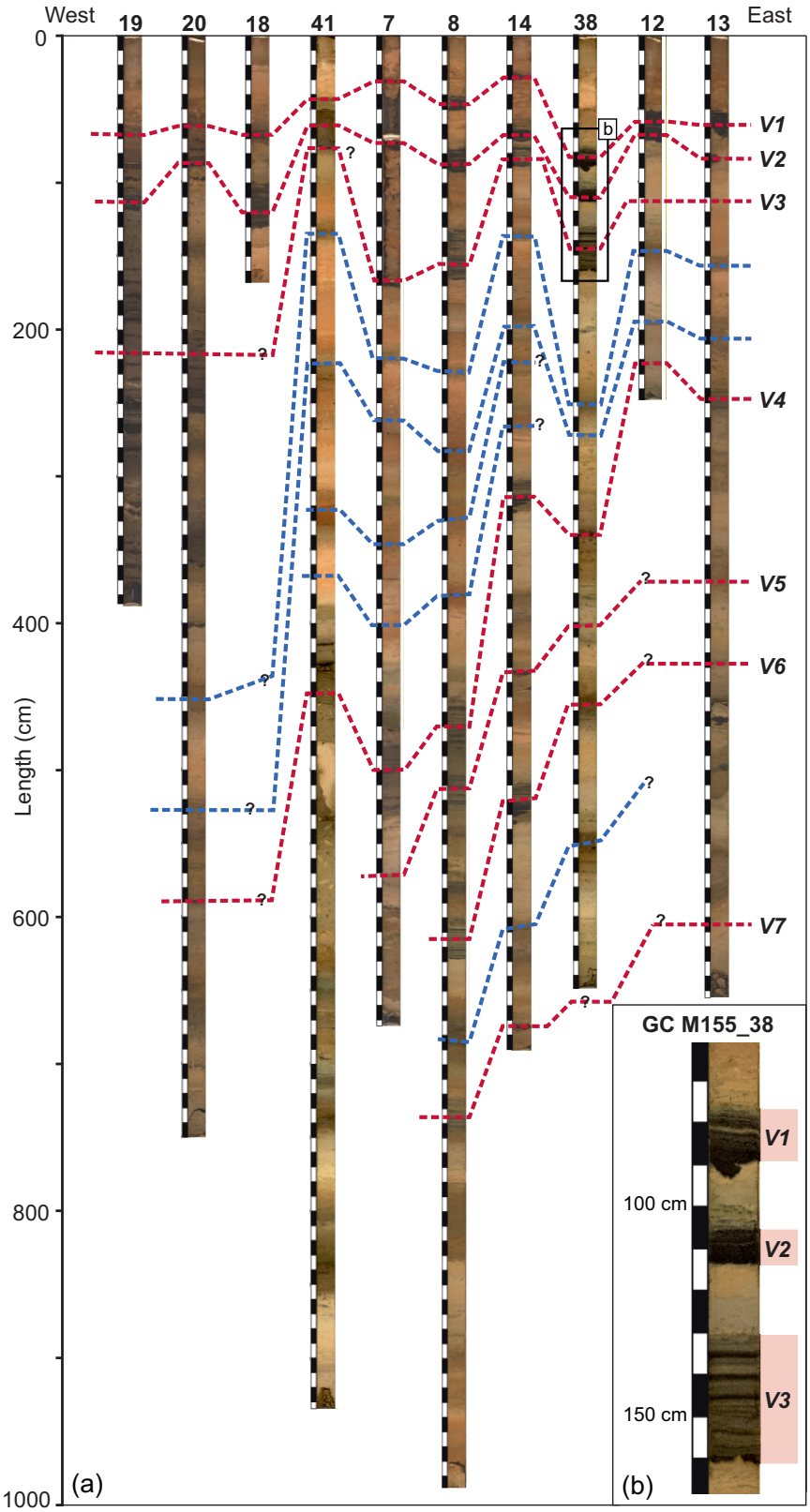

Figure 3.4: (a) Compilation of sediment gravity cores retrieved south of Fogo and Santiago during M155 showing preliminary stratigraphic correlations based on visual analysis. Dashed red lines: correlations between different volcaniclastic sand layers (V1-V7); Dashed blue lines: correlation of background sediment layers (reddish-brown horizons) that helped to correlate the volcaniclastic sand layers. The location of these cores is shown in Figure 3.1c. (b) Zoom of gravity core M155-38 (62-168 cm) showing the visually identified volcaniclastic layers V1-3.

and/or hyperbolic facies and occur both above and below MTD-B. Several of these MTDs are exposed at the surface and have remobilized previously failed sediments, including those of MTD-B (e.g. Figure 3.5, 3.6). However, as for MTD-B, their full lateral extent is generally poorly constrained due to large profile spacings and their possible continuation outside the surveyed area. The morphological steps vary in length, height, strike, and orientation (Figure 3.5a), but are typically near-vertical (Figure 3.5c, d). In the following section, we describe the character of, and relation between, several of these features in more detail.

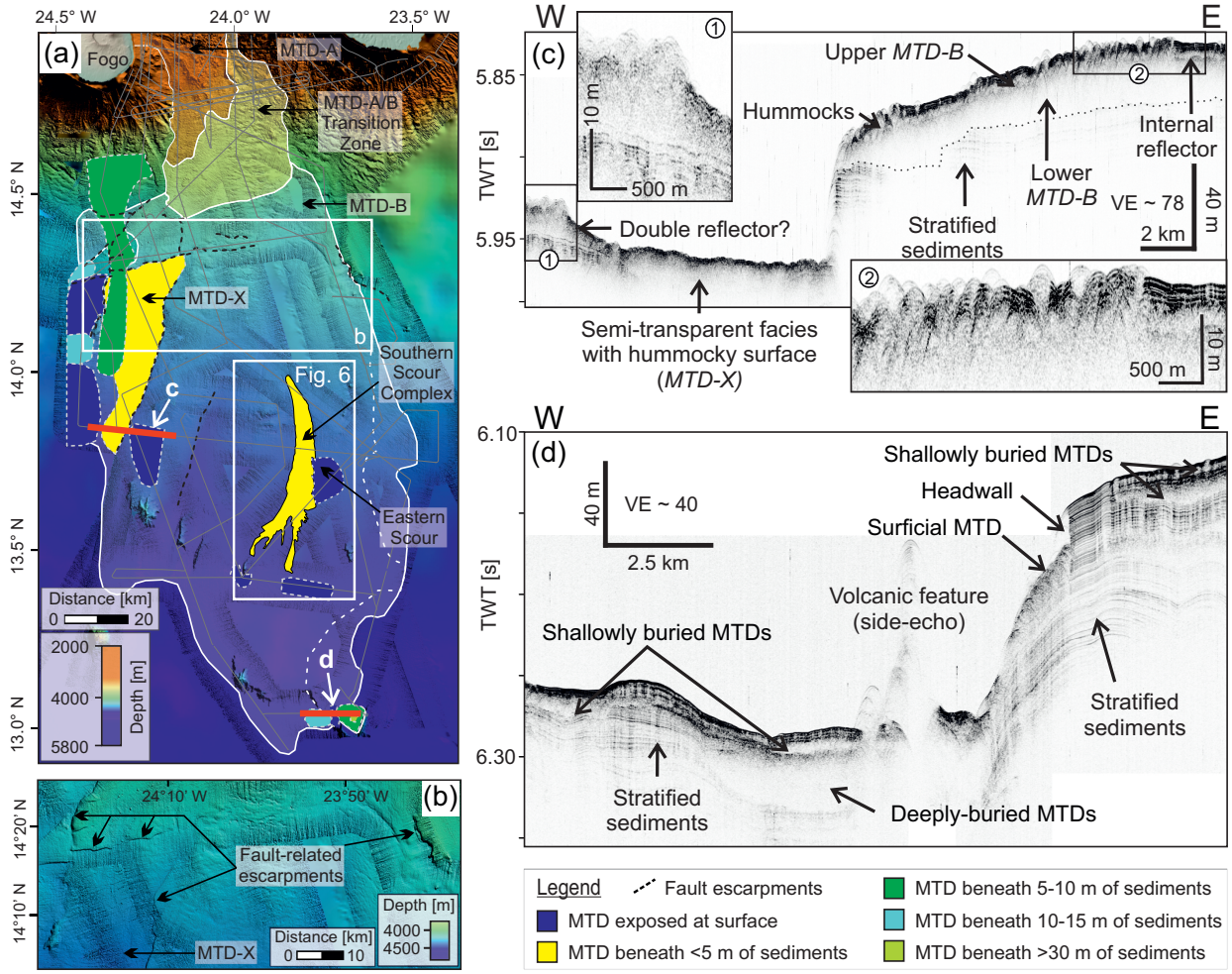

Figure 3.5: (a) Multibeam data overlain on GEBCO2019 bathymetry highlighting the presence of multiple fault-related escarpments and volcanic features on the shallow slopes south of Fogo. Additional mass-transport deposits are also identified in the Parasound data and coloured according to their burial depth (see legend). Solid red lines: location of the Parasound profiles shown in (c) and (d). (b) Multibeam data showing the nature of the fault-related escarpments on the slopes south of Fogo and Santiago in more detail. (c) Parasound profile crossing one of the most striking escarpments visible on the western side (see 5b), highlights the relation between tectonic processes and landsliding in the area. Monte Amarelo MTD-B deposits (eastern side) are remobilised across the escarpment. (d) Parasound profile crossing an escarpment in the southern reaches of the working area highlights acoustically transparent MTDs at varying depths.

3.3.3.1 Tectonic escarpments along the western and eastern margins

A series of escarpments is imaged to the west, along the western margin of MTD-B, and stretching between 40 and 110 km south of Fogo (Figure 3.5a,b). The most prominent escarpment is orientated roughly north-south and extends across ∼55 km. It is ∼50 m high and near vertical (Figure 3.5c). Monte Amarelo MTD-B deposits are imaged on the eastern side (footwall) of this step. On the western (hanging wall) side, the sediments are characterized by a semi-transparent facies with a hummocky upper surface (hereafter referred to as MTD-X; Figure 3.5c). In places, a pair of strong reflectors is identified within the sedimentary drape that overlies MTD-X. Proximal to the escarpment, the base of MTD-X cannot be resolved. Further west of the scarp, however, stratified sediment is imaged below the base of MTD-X (inset 1 of Figure 3.5c). The lateral extent of MTD-X is constrained to both the north and east by the morphological steps (Figure 3.5b,c), resulting in a minimum area of 900 km^2 for MTD-X.

3.3.3.2 Southern Scour Complex

A prominent, elongated scour-shaped feature is evident in the central part of the southern distal region (hereafter referred to as the Southern Scour Complex (SSC), Figure 3.6a). This feature is ∼60 km long and covers an area of ∼340 km^2. The western and eastern sides of the SSC are constrained by up-to-40 and 55 m high escarpments, respectively (Figure 3.6). In Parasound data crossing the complex, acoustically transparent facies with a strong internal reflector characterizing the Monte Amarelo MTD-B is evident on both the eastern and western sides of the SSC (Figure 3.6b,c). In the central part of the SSC (Figure 3.6c), acoustically transparent MTDs with some internal structure are covered by ∼3 m of stratified sediment. In the northern part, the material within the SSC is characterized by a semi-transparent facies with a hummocky upper surface, and the deposits are largely exposed at the surface (Figure 3.6b). An additional instability is visible on the eastern side of the SSC (hereafter referred to as the Eastern Scour (ES); Figure 3.6d). The ES reaches a thickness of up to 35 m thick in its centre, and covers an area of ∼120 km^2. Parasound data across the ES show that this failure primarily remobilized the Monte Amarelo MTD-B deposits in this region along the same basal glide plane as MTD-B (Figure 3.6d). To the south, the SCC is fan-shaped, with fingers of unfailed stratified sediments standing up to ∼20 m above failed sediment (Figure 3.6d). Semi-transparent deposits characteristic of MTD-B are imaged on the tops of these stratified fingers.

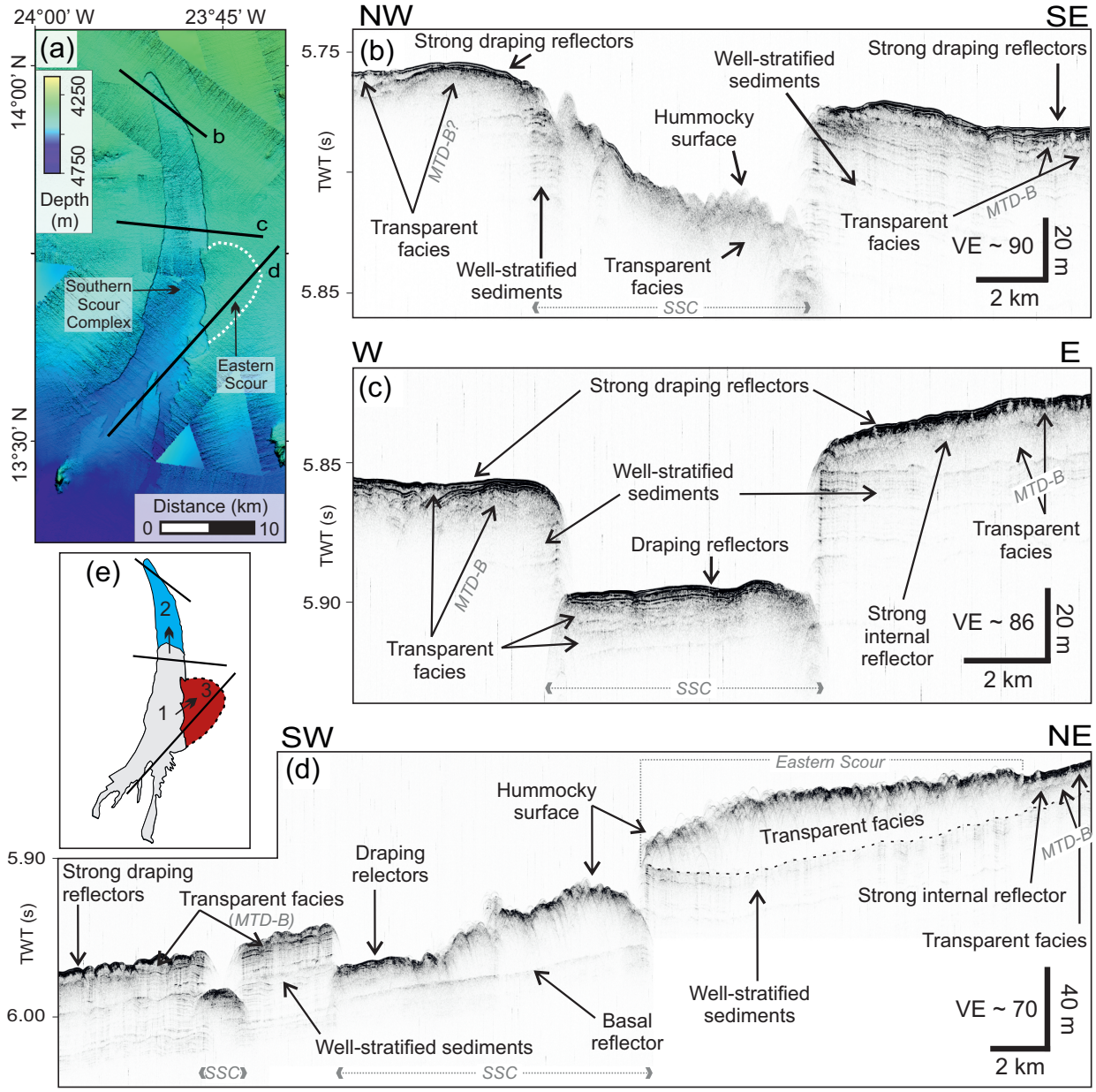

Figure 3.6: The Southern Scour Complex (SSC). (a) Multibeam data highlighting the surface morphology of the Southern Scour Complex and the extension of the Eastern Scour (dashed white line). The location of Figure 3.6a with respect to the other features discussed in this article is shown in Figure 3.5. (b-d) Parasound profiles crossing the SSC showing a complex relationship between former and more recent landsliding processes, along with the variable acoustic character of the deposits and of the adjacent unfailed material. (e) Conceptual model showing the proposed retrogressive development of the SSC towards the north and east. Numbers 1-3 highlight the sequence of events.

3.4 Discussion

3.4.1 The two-fold nature of Fogo's Monte Amarelo flank-collapse

Based on the difference in their acoustic character, we distinguish between two main types of deposits related to the Monte Amarelo volcanic flank-collapse: hummocky, debris avalanche deposits proximal to Fogo (MTD-A), and finer-grained, acoustically transparent landslide deposits (MTD-B) at greater distances from Fogo that were previously not recognized (Figure 3.3). The blocky debris avalanche deposits of MTD-A cover a surface area of 3,180 km^2. If we also include the region in which the size of the hummocks decreases with distance from the source (marked by the yellow shaded region in Figure 3.3a), this increases the total area of MTD-A to 6,820 km^2; more than four times the previous estimate ($\sim$1,470 km^2; Masson et al., 2008). As the base of the volcanic debris avalanche deposits is not resolved by the Parasound data, we cannot, at this stage, revisit estimates of the volume involved.

Monte Amarelo MTD-B is characterised by an acoustically transparent to semi-transparent facies that is overlain by a series of two to four strong reflectors (Figure 3.3, 3.5c, 3.6b-d). A prominent, internal reflection is clearly observed in places within the deposits; separating MTD-B into two main parts (Figure 3.3d, e). The uppermost section is of relatively constant thickness (4-6 m). Contrastingly the thickness of the lower part of MTD-B is highly variable (up to 15 m thick). Interestingly, the upper and lower parts of MTD-B have a similar areal distribution within the volcaniclastic apron; covering a minimum of 18,400 km^2 (upper) and 19,500 km^2 (lower) (Figure 3.3a). This implies minimum volumes of 92 km^3 (upper) and 195 km^3 (lower), assuming average thicknesses of 5 m (upper) and 10 m (lower). Their similar distribution implies that the upper and lower parts of MTD-B might share the same source or, at least, be genetically linked. We therefore infer that the upper and lower part of MTD-B might have been emplaced (almost) contemporaneously. The absolute timing of these two phases, however, remains unclear. Of particular interest is whether these two failures occurred as two phases of the same event, or as two distinct events separated by some time. Further analytical work on the sediment cores will help to reveal more information about the nature of the prominent internal reflection, along with the relative timing of these two depositional episodes.

A similar two-fold nature of volcanic flank-collapse deposits hummocky debris avalanche deposits accompanied by acoustically transparent to seismically chaotic deposits with a comparatively smooth upper surface has also been reported for flank-collapses at other locations, including in the Lesser Antilles (Watt et al., 2012b,a, Le Friant et al., 2015, Brunet et al., 2016); at La Réunion (Indian Ocean; Lebas et al., 2018); and at Ritter

Island (Papua New Guinea; Karstens et al., 2019, Watt et al., 2019). Drilled cores retrieved during IODP Expedition 340 in the Lesser Antilles indicated that widespread, seismically chaotic deposits (interpreted as equivalent to our MTD-B) primarily consist of hemipelagic mud interbedded with a combination of tephra, volcaniclastic layers, or bioclastic turbiditic deposits, which have undergone varying degrees of deformation (Le Friant et al., 2015, Brunet et al., 2016). To explain these findings, Le Friant et al. (2015) proposed a failure model where the loading of seafloor sediment by volcanic debris avalanche deposits triggered sediment destabilization and progressive downslope-propagating failure along a decollement. In this way, the deformation can propagate great distances away from the flank-collapse, affecting seafloor sediments that were otherwise stable (Le Friant et al., 2015). The acoustic character of our MTD-B bears a strong resemblance to the seismically chaotic deposits in the Lesser Antilles. We, therefore, interpret MTD-B to be the result of the failure of pre-existing seafloor sediments following the loading of the Monte Amarelo debris avalanche deposits (MTD-A).

3.4.2 A history of mass wasting and remobilization in the southern Cape Verdes

3.4.2.1 Repeated mass-wasting events at Fogo?

Preliminary stratigraphic correlations based on visual similarities of cores in the southern distal part of the working area indicate at least seven volcaniclastic or mixed volcaniclastic-bioclastic sandy turbidite layers above and below the Monte Amarelo flank-collapse deposits (Figure 3.4). These turbidite layers are dominated by mafic glass, crystals and lava fragments, which, based on their petrography, suggests that they originated from Fogo volcano. This indicates that smaller mass-wasting events may have occurred at Fogo in addition to the Monte Amarelo volcanic flank-collapse, as also recently suggested by Marques et al. (2019). Correlation and origin of these volcaniclastic deposits will, however, be verified by future analytical work on the sediment cores.

3.4.2.2 Regional tectonic and volcanic influences south of Fogo?

The multiple fault-related escarpments and MTDs identified in the acoustic data south of Fogo further highlight a long and complex history of instability and slope failure in the region (Figure 3.5). Ramalho et al. (2010) found that the island of Santiago has uplifted at a rate of ∼100 m/Myr over the past 4 Myr, and attributed this uplift to a combination of magmatic intrusions under or within the island edifice, together with episodic swell-wide

uplift that affected the whole archipelago. Although geologically recent uplift has not been reported at Fogo, the neighbouring island of Brava has experienced one of the most dramatic intrusion-related uplift trends of any ocean island in the world, with up to 400 m of uplift in the last 1.8 Ma (Madeira et al., 2010). The presence of such widespread uplift across the archipelago - and particularly around the southern Cape Verdes - thus suggests that the series of escarpments and landslides observed on the slopes south of Fogo may be the surface expression of a combination of regional tectonics, associated with the growth of the Cape Verdes hotspot swell, and crustal intrusions in the vicinity of the islands. As several of the exposed faults have landslide deposits on their hanging wall side, we interpret that these MTDs are most likely the results of movement along the faults and, as such, the result of neo-tectonic activity.

The Southern Scour Complex (SSC), which is exposed at the seafloor, post-dates the Monte Amarelo flank-collapse (Figure 3.6). Monte Amarelo MTD-B deposits are imaged on the footwall east of the SSC (Figure 3.6b-d), and on the tops of the unfailed, stratified fingers at the southern extent of the SSC (Figure 3.6d). This indicates that the SSC formed after the Monte Amarelo flank-collapse, remobilizing MTD-B. In the northern and eastern parts of the SSC, acoustically transparent mass-wasting deposits are exposed at the seafloor, highlighting more recent mass wasting and remobilization of MTD-B (Figure 3.6b). We interpret the more recent mass-wasting deposits in the northern and eastern parts of the SSC as evidence of retrogressive development of the SSC in these directions (Figure 3.6e).

The presence of fault-related escarpments on the slopes south of Fogo, frequent volcanic episodes at Fogo (Ribeiro, 1960, Torres et al., 1997), and ongoing uplift at the neighbouring islands of Santiago and Brava (Madeira et al., 2010, Ramalho et al., 2010), together imply the occurrence of frequent earthquakes in the past. The volcanic activity at Fogo has resulted in the widespread deposition of numerous tephra layers (Eisele et al., 2015). Subsequent earthquake shaking may have resulted in liquefaction of overlying layers, which, together with sedimentary over-pressure following further sediment deposition, can help to precondition the shallow slopes for failure (Moernaut et al., 2019). Even small changes in the stress regime of tephra layers have been found to be able to trigger failure (Hornbach et al., 2015). Consequently, it is possible that some of the MTDs observed on the shallowly dipping slopes south of Fogo, and unrelated to escarpments, may result from such a process. Future work, particularly on the sediment cores collected during cruise M155, will help to shed light on the sources and processes responsible for the MTDs mapped on the shallow slopes south of Fogo and Santiago.

3.5 Implications and conclusions

In this study, we revisited the Monte Amarelo volcanic flank-collapse of Fogo Island and found that the deposition of the debris avalanche material may have triggered subsequent failures of pre-existing seafloor sediments in (at least) two phases. This is similar to what has been observed in the Lesser Antilles (Le Friant et al., 2015, Brunet et al., 2016), at La Réunion (Lebas et al., 2018), and at Ritter Island (Karstens et al., 2019, Watt et al., 2019). It is not yet clear whether these two phases of seafloor sediment failure were synchronous as a result of a single flank-collapse, or if they reflect multiple, distinct events. The question of whether the main flank-collapse occurred as a single or as multiple events is of utmost importance for tsunami modelling because the volume and timing of individual failures are the main factors controlling the tsunamigenic potential (Løvholt et al., 2015). Water depth and landslide kinematics play a key role in controlling the tsunamigenic potential of a subaqueous landslide (Watts et al., 2000, Ward, 2001, Watt et al., 2012b, Harbitz et al., 2014). As MTD-B occurred in depths exceeding 3,000 m, we consider that its influence on the resulting tsunami magnitude was negligible, and that only the hummocky debris avalanche deposits (MTD-A) contributed to the megatsunami that inundated nearby islands.

Multibeam bathymetric, sediment echo-sounder, and sediment gravity core data acquired during cruise M155 of R/V Meteor provide seafloor evidence that show, for the first time, the presence of multiple additional mass-wasting events on the shallow slopes south of Fogo. Turbidite sands recovered in the cores have a volcaniclastic or mixed volcaniclastic-bioclastic composition, which suggests that prevailing mass-transport processes in the region may be dominated by volcanic eruptions or volcanic mass-wasting events. However, it is also possible that some of the additional mass-wasting events are unrelated to flank-collapse events or submarine failures, and could instead have been generated by sedimentary overpressure and/or by the presence of a mechanically weak layer such as tephra or turbidites. Further analytical work is required to verify the sources of these events on the shallow slopes south of the Cape Verdean archipelago. As these layers are thin, have limited lateral extent, and occurred on low-gradient slopes in deep water, we consider their associated tsunamigenic potential to be low.

Acknowledgements

We are grateful to the captain, crew and scientific teams of R/V Meteor (M155) for their enthusiasm and assistance onboard. We are also thankful for the thoughtful reviews of the editor, Lawrence Amy, as well as Paraskevi Nomikou and two anonymous reviewers, whose

comments improved this manuscript. Data acquisition during R/V Meteor's cruise M155 was funded by the DFG and BMBF. R. Barrett is funded by the European Union's Horizon 2020 research and innovation programme under the Marie Sklodowska-Curie grant agreement No. 721403 (SLATE - 'Submarine LAndslides and Their impact on European continental margins'). R. Ramalho acknowledges his IF/01641/2015 contract funded by Fundacão para a Ciência e Tecnologia (FCT), as well as the following projects funded by FCT: IF/01641/2015, LISBOA-01-0145-FEDER-028588 and PTDC/CTA-GEO/28588/2017 UNTIeD, PTDC/GEOGEO/1123/2014 FIRE, and UID/GEO/50019/2019 Instituto Dom Luiz.

References

Abadie, S. M., Harris, J. C., Grilli, S. T., and Fabre, R. (2012). Numerical modeling of tsunami waves generated by the flank collapse of the Cumbre Vieja Volcano (La Palma, Canary Islands): Tsunami source and near field effects. *Journal of Geophysical Research: Oceans*, 117(5):1–26.

Begét, J. E. and Kienle, J. (1992). Cyclic formation of debris avalanches at Mount St Augustine volcano. *Nature*, 356:701–704.

Blahut, J., Balek, J., Klimeš, J., Rowberry, M., Kusák, M., and Kalina, J. (2019). A comprehensive global database of giant landslides on volcanic islands. *Landslides*, 16(10):2045–2052.

Brum da Silveira, A., Madeira, J., Serralheiro, A., Torres, P., da Silva, L., and Mendes, M. (1997). O controlo estrutural da erupcao de Abril de 1995 na Ilha do Fogo, Cabo Verde. In *A Erupcao Vulcanica de 1995 na Ilha do Fogo, Cabo Verde*, pages 51–61. IICT, Lisboa, Portugal.

Brunet, M., Le Friant, A., Boudon, G., Lafuerza, S., Talling, P., Hornbach, M. J., Ishizuka, O., Lebas, E., Guyard, H., and Science Party, I. E. . (2016). Composition, geometry, and emplacement dynamics of a large volcanic island landslide offshore Martinique: From volcano flank-collapse to seafloor sediment failure? *Geochemistry Geophysics Geosystems*, 17:699–724.

Casalbore, D., Romagnoli., C., Bosman, A., and Chiocci, F. L. (2011). Potential tsunamigenic landslides at Stromboli Volcano (Italy): insight from marine DEM analysis. *Geomorphology*, 126:42–50.

Casalbore, D., Romagnoli, C., Pimentel, A., Quartau, R., Casas, D., Ercilla, G., Hipólito, A., Sposato, A., and Chiocci, F. L. (2015). Volcanic, tectonic and mass-wasting processes offshore Terceira Island (Azores) revealed by high-resolution seafloor mapping. *Bulletin of Volcanology*, 77(24).

Casalbore, D. (2018). Volcanic islands and seamounts. In Micallef, A., Krastel, S., and Savini, A., editors, *Submarine Geomorphology*, pages 333–347. Springer Geology, Cham, Switzerland.

Cervelli, P., Segall, P., Johnson, K., Lisowski, M., Miklius, A., and Building, M. (2002). Sudden aseismic fault slip on the south flank of Kilauea volcano. *Nature*, 415:1014–1018.

Clare, M. A., Le Bas, T., Price, D. M., Hunt, J. E., Sear, D., Cartigny, M. J. B., Vellinga, A., Symons, W., Firth, C., and Cronin, S. (2018). Complex and Cascading Triggering of Submarine Landslides and Turbidity Currents at Volcanic Islands Revealed From Integration of High-Resolution Onshore and Offshore Surveys. *Frontiers in Earth Science*, 6:1–24.

Crough, S. T. (1978). Thermal origin of mid-plate hot-spot swells. *Geophysical Journal International*, 55(2):451–469.

Day, S. J., Heleno Da Silva, S. I., and Fonseca, J. F. (1999). A past giant lateral collapse and present-day flank instability of Fogo, Cape Verde Islands. *Journal of Volcanology and Geothermal Research*, 94(1-4):191–218.

Eisele, S., Reißig, S., Freundt, A., Kutterolf, S., Nürnberg, D., Wang, K. L., and Kwasnitschka, T. (2015). Pleistocene to Holocene offshore tephrostratigraphy of highly explosive eruptions from the southwestern Cape Verde Archipelago. *Marine Geology*, 369:233–250.

Faria, B. and Fonseca, J. F. (2014). Investigating volcanic hazard in Cape Verde Islands through geophysical monitoring: Network description and first results. *Natural Hazards and Earth System Sciences*, 14(2):485–499.

Foeken, J. P., Day, S., and Stuart, F. M. (2009). Cosmogenic 3He exposure dating of the Quaternary basalts from Fogo, Cape Verdes: Implications for rift zone and magmatic reorganisation. *Quaternary Geochronology*, 4(1):37–49.

Goff, J., Terry, J. P., Chagué-Goff, C., and Goto, K. (2014). What is a mega-tsunami? *Marine Geology*, 358:12–17.

González, P. J., Bagnardi, M., Hooper, A. J., Larsen, Y., Marinkovic, P., Samsonov, S. V., and Wright, T. J. (2015). The 20142015 eruption of Fogo volcano: Geodetic modeling of Sentinel1 TOPS interferometry. *Geophysical Research Letters*, 42:9239–9246.

Grevemeyer, I., Helffrich, G., Faria, B., Booth-Rea, G., Schnabel, M., and Weinrebe, W. (2010). Seismic activity at Cadamosto seamount near Fogo Island, Cape Verdes - formation of a new ocean island? *Geophysical Journal International*, 180(2):552–558.

Grilli, S., Svendsen, I., and Subramanya, R. (1997). Breaking Criterion and Characteristics for Solitary Waves on Slopes. *Journal of Waterway, Port, Coastal and Ocean Engineering*, 123(3).

Grilli, S. T., Tappin, D. R., Carey, S., Watt, S. F., Ward, S. N., Grilli, A. R., Engwell, S. L., Zhang, C., Kirby, J. T., Schambach, L., and Muin, M. (2019). Modelling of the tsunami from the December 22, 2018 lateral collapse of Anak Krakatau volcano in the Sunda Straits, Indonesia. *Scientific Reports*, 9(1):1–13.

Gross, F., Krastel, S., Chiocci, F. L., Ridente, D., Bialas, J., Schwab, J., Beier, J., Cukur, D., and Winkelmann, D. (2014). Evidence for submarine landslides offshore Mt. Etna, Italy. In Krastel, S., Behrmann, J. H., Völker, D. J., Stipp, M., Berndt, C., Urgeles, R., Chaytor, J. D., Huhn, K., Strasser, M., and Harbitz, C. B., editors, *Submarine Mass Movements and Their Consequences: Advances in Natural and Technological Hazards Research*, pages 307–316. Springer, Cham, 37 edition.

Hansteen, T. H., Kwasnitschka, T., and Klügel, A. (2014). Cape Verde Seamounts Cruise No. M80/3 December 29, 2009 February 1, 2010 - Dakar (Senegal) - Las Palmas de Gran Canaria (Spain). Technical report, METEOR-Berichte, DFG-Senatskommission für Ozeanographie.

Harbitz, C. B., Løvholt, F., and Bungum, H. (2014). Submarine landslide tsunamis: how extreme and how likely? *Natural Hazards*, 72:1341–1374.

Harders, R., Kutterolf, S., Hensen, C., Moerz, T., and Brueckmann, W. (2010). Tephra layers: A controlling factor on submarine translational sliding? *Geochemistry, Geophysics, Geosystems*, 11(5):1–18.

Holm, P. M., Grandvuinet, T., Friis, J., Wilson, J. R., Barker, A. K., and Plesner, S. (2008). An 40Ar39Ar study of the Cape Verde hot spot: Temporal evolution in a semistationary plate environment. *Journal of Geophysical Research: Solid Earth*, 113(B08201).

Hornbach, M. J., Manga, M., Genecov, M., Valdez, R., Miller, P., Saffer, D., Adelstein, E., Lafuerza, S., Adachi, T., Breitkreuz, C., Jutzeler, M., Le Friant, A., Ishizuka, O., Morgan, S., Slagle, A., Talling, P. J., Fraass, A., Watt, S. F. L., Stroncik, N. A., Aljahdali, M., Boudon, G., Fujinawa, A., Hatfield, R., Kataoka, K., Maeno, F., Martinez-Colon, M., McCanta, M., Palmer, M., Stinton, A., Subramanyam, K. S. V., Tamura, Y., Villemant, B., Wall-Palmer, D., and Wang, F. (2015). Permeability and pressure measurements in Lesser Antilles submarine slides: Evidence for pressure-driven slow-slip failure. *Journal of Geophysical Research: Solid Earth*, 120(12):7986–8011.

Karstens, J., Berndt, C., Urlaub, M., Watt, S. F., Micallef, A., Ray, M., Klaucke, I., Muff, S., Klaeschen, D., Kühn, M., Roth, T., Böttner, C., Schramm, B., Elger, J., and Brune, S. (2019). From gradual spreading to catastrophic collapse - Reconstruction of the 1888 Ritter Island volcanic sector collapse from high-resolution 3D seismic data. *Earth and Planetary Science Letters*, 517:1–13.

Krastel, S., Schmincke, H. U., Jacobs, C. L., Rihm, R., Le Bas, T. P., and Alibés, B. (2001). Submarine landslides around the Canary Islands. *Journal of Geophysical Research: Solid Earth*, 106(B3):3977–3997.

Krastel, S., Andrade, M., Barrett, R., Donoval, D., Hauser, R., Heinrich, S., Hinz, A.-K., Jähmlich, H., Klaucke, I., Klein, E., Klügel, A., Köck, D., Kutterolf, S., Lebas, E., Lindhorst, K., Pank, K., Ramalho, R., Rohleder, C., Scheffler, J., Tang, Q., and Villinger, H. (2019). The tsunamigenic gravitational flank-collapse of Fogo volcano, Cape Verde Islands, Seismic pre-site survey for an IODP site on the Cape Verde Plateau, Cruise No. M155, 26.05.19 - 30.06.19, Pointe-à-Pitre (Guadeloupe) - Mindelo (Cape Verde). Technical report, METEOR-Berichte, Gutachterpanel Forschungsschiffe, Bonn.

Kuhlmann, J., Huhn, K., and Ikari, M. J. (2016). Do embedded volcanoclastic layers serve as potential glide planes? An integrated analysis from the Gela Basin offshore southern Sicily. In Lamarche, G., Mountjoy, J., Bull, S., Hubble, T., Krastel, S., Lane, E., Micallef, A., Moscardelli, L., Mueller, C., Pecher, I., and Woelz, S., editors, *Submarine Mass Movements and Their Consequences. Advances in Natural and Technological Hazards Research*, pages 273–280. Springer International Publishing, Cham, Switzerland, 41 edition.

Lafuerza, S., Le Friant, A., Manga, M., Boudon, G., Villemant, B., Stroncik, N., Voight, B., Hornbach, M., Ishizuka, O., and Party, t. E. . S. (2014). Geomechanical characterizations of submarine volcano flank sediments, Martinique, Lesser Antilles Arc. In Krastel, S., Behrmann, J.-H., Stipp, M., Völker, D., Urgeles, R., Berndt, C., Huhn, K., Chaytor, J., Harbitz, C. B., and Strasser, M., editors, *Submarine Mass Movements and Their Consequences. Advances in Natural and Technological Hazards Research*. Springer International Publishing, Cham, Switzerland, 37 edition.

Le Bas, T. P., Masson, D. G., Holtom, R. T., and Grevemeyer, I. (2007). Slope Failures of the Flanks of the Southern Cape Verde Islands. In Lykousis, V., Sakellariou, D., and Locat, J., editors, *Submarine Mass Movements and Their Consequences: Advances in Natural and Technological Hazards Research*, pages 337–345. Springer, Dordrecht, Netherlands, 27 edition.

Le Friant, A., Ishizuka, O., Boudon, G., Palmer, M., Talling, P., Villemant, B., Adachi, T., Aljahdali, M., Breitkreuz, C., Brunet, M., Caron, B., Coussens, M., Deplus, C., Endo, D., Feuillet, N.,

Fraas, A., Fujinawa, A., Hart, M., Hatfield, R., Hornbach, M., Jutzeler, M., Kataoka, K., Komorowski, J.-C., Lebas, E., Lafuerza, S., Maeno, F., Manga, M., Martnez-Colon, M., McCanta, M., Morgan, S., Saito, T., Slagle, A., Sparks, S., Stinton, A., Stroncik, N., Subramanyam, K., Tamura, Y., Trofimovs, J., Voight, B., Wall-Palmer, D., Wang, F., and Watt, S. (2015). Submarine record of volcanic island construction and collapse in the Lesser Antilles arc: First scientific drilling of submarine volcanic island landslides by IODP Expedition 340. *Geochemistry Geophysics Geosystems*, 16:420–442.

Lebas, E., Le Friant, A., Boudon, G., Watt, S. F., Talling, P. J., Feuillet, N., Deplus, C., Berndt, C., and Vardy, M. E. (2011). Multiple widespread landslides during the long-term evolution of a volcanic island: Insights from high-resolution seismic data, Montserrat, Lesser Antilles. *Geochemistry, Geophysics, Geosystems*, 12(5).

Lebas, E., Le Friant, A., Deplus, C., and de Voogd, B. (2018). Understanding the Evolution of an Oceanic Intraplate Volcano From Seismic Reflection Data: A New Model for La Réunion, Indian Ocean. *Journal of Geophysical Research: Solid Earth*, 123(2):1035–1059.

León, R., Somoza, L., Urgeles, R., Medialdea, T., Ferrer, M., Biain, A., García-Crespo, J., Mediato, J. F., Galindo, I., Yepes, J., González, F. J., and Gimenez-Moreno, J. (2017). Multi-event oceanic island landslides: New onshore-offshore insights from El Hierro Island, Canary Archipelago. *Marine Geology*, 393:156–175.

Livanos, I., Nomikou, P., Papanikolaou, D., and Rousakis, G. (2013). The volcanic debris avalanche on the SE submarine slope of Nisyros volcano, Greece: Geophysical exploration and implications for subaerial eruption history. *Geo-Marine Letters*, 33(6):419–431.

Locat, J., Leroueil, S., Locat, A., and Lee, H. (2014). Weak layers: their definition and classification from a geotechnical perspective. In Krastel, S., Behrmann, J.-H., Stipp, M., Völker, D., Urgeles, R., Berndt, C., Huhn, K., Chaytor, J., Harbitz, C. B., and Strasser, M., editors, *Submarine Mass Movements and Their Consequences: Advances in Natural and Technological Hazards Research*, pages 3–12. Springer, Cham, 37 edition.

Løvholt, F., Pedersen, G., Harbitz, C. B., Glimsdal, S., and Kim, J. (2015). On the characteristics of landslide tsunamis. *Philosophical Transactions of the Royal Society A: Mathematical, Physical and Engineering Sciences*, 373(2053):20140376.

Madeira, J., Brum da Silveira, A., Mata, J., Mourão, C., and Martins, S. (2008). The role of mass movements on the geomorphologic evolution of island volcanoes: examples from Fogo and Brava in the Cape Verde archipelago. *Comunicações Geológicas*, 95:93–106.

Madeira, J., Mata, J., Mourao, C., Brum da Silveira, A., Martins, S., Ramalho, R., and Hoffman, D. (2010). Volcano-stratigraphic and structural evolution of Brava Island (Cape Verde) based on 40Ar/39Ar, UTh and field constraints. *Journal of Volcanology and Geothermal Research*, 196:219–235.

Madeira, J., Ramalho, R. S., Hoffmann, D. L., Mata, J., and Moreira, M. (2019). A geological record of multiple Pleistocene tsunami inundations in an oceanic island: The case of Maio, Cape Verde. *Sedimentology*, 67(3):1529–1552.

Marques, F. O., Hildenbrand, A., Victória, S. S., Cunha, C., and Dias, P. (2019). Caldera or flank collapse in the Fogo volcano? What age? Consequences for risk assessment in volcanic islands. *Journal of Volcanology and Geothermal Research*, 388.

Martínez-Moreno, F. J., Monteiro Santos, F. A., Madeira, J., Pous, J., Bernardo, I., Soares, A.,

Esteves, M., Adão, F., Ribeiro, J., Mata, J., and Brum da Silveira, A. (2018). Investigating collapse structures in oceanic islands using magnetotelluric surveys: The case of Fogo Island in Cape Verde. *Journal of Volcanology and Geothermal Research*, 357:152–162.

Masson, D. G., Watts, A. B., Gee, M. J., Urgeles, R., Mitchell, N. C., Le Bas, T. P., and Canals, M. (2002). Slope failures on the flanks of the western Canary Islands. *Earth-Science Reviews*, 57(1-2):1–35.

Masson, D. G., Le Bas, T. P., Grevemeyer, I., and Weinrebe, W. (2008). Flank collapse and large-scale landsliding in the Cape Verde Islands, off West Africa. *Geochemistry, Geophysics, Geosystems*, 9(7):1–16.

McGuire, W. (1996). Volcano instability: a review of contemporary themes. *Geological Society, London, Special Publications*, 110:1–23.

McGuire, W. (2003). Volcano instability and lateral collapse. *Revista*, 1:33–45.

McMurtry, G. M., Fryer, G. J., Tappin, D. R., Wilkinson, I. P., Williams, M., Fietzke, J., Garbe-Schoenberg, D., and Watts, P. (2004). Megatsunami deposits on Kohala volcano, Hawaii, from flank collapse of Mauna Loa. *Geology*, 32(9):741–744.

Moernaut, J., Van Daele, M., Heirman, K., Wiemer, G., Molenaar, A., Vandorpe, T., Melnick, D., Hajdas, I., Pino, M., Urrutia, R., and De Batist, M. (2019). The subaqueous landslide cycle in south-central Chilean lakes: The role of tephra, slope gradient and repeated seismic shaking. *Sedimentary Geology*, 381:84–105.

Moore, J. G. and Moore, G. W. (1984). Deposit from a Giant Wave on the Island of Lanai, Hawaii. *Science*, 226(4680):1312–1315.

Moore, J. G., Clague, D. A., Holcomb, R. T., Lipman, P. W., Normark, W. R., and Torresan, M. E. (1989). Prodigious submarine landslides on the Hawaiian Ridge. *Journal of Geophysical Research*, 94(B12):17465.

Murray, J. and Voigt, B. (1996). Slope stability and eruption prediction on the eastern flank of Mount Etna. *Geological Society, London, Special Publications*, 110:111–114.

Paris, R., Giachetti, T., Chevalier, J., Guillou, H., and Frank, N. (2011). Tsunami deposits in Santiago Island (Cape Verde archipelago) as possible evidence of a massive flank failure of Fogos volcano. *Sedimentary Geology*, 239(3-4):129–145.

Paris, R., Ramalho, R. S., Madeira, J., Ávila, S., May, S. M., Rixhon, G., Engel, M., Brückner, H., Herzog, M., Schukraft, G., Perez-Torrado, F. J., Rodriguez-Gonzalez, A., Carracedo, J. C., and Giachetti, T. (2018). Mega-tsunami conglomerates and flank collapses of ocean island volcanoes. *Marine Geology*, 395(September 2017):168–187.

Ramalho, R., Helffrich, G., Cosca, M., Vance, D., Hoffmann, D., and Schmidt, D. N. (2010). Episodic swell growth inferred from variable uplift of the Cape Verde hotspot islands. *Nature Geoscience*, 3(11):774–777.

Ramalho, R. S., Winckler, G., Madeira, J., Helffrich, G. R., Hipólito, A., Quartau, R., Adena, K., and Schaefer, J. M. (2015). Hazard potential of volcanic flank collapses raised by new megatsunami evidence. *Science Advances*, 1(9):1–11.

Ribeiro, O. (1960). A ilha do Fogo e as suas erupiones. In *Memorias, serie geografica I. Publ. Junta de Investigacoes do Ultramar*. Ministerio do Ultramar, Lisbon, Portugal, 2 edition.

Sammartini, M., Camerlenghi, A., Budillon, F., Insinga, D. D., Zgur, F., Conforti, A., Iorio, M., Romeo, R., and Tonielli, R. (2018). Open-slope, translational submarine landslide in a tectonically active volcanic continental margin (Licosa submarine landslide, southern Tyrrhenian Sea). *Geological Society, London, Special Publications*, 477(1):133–150.

Siebert, L. (1984). Large volcanic debris avalanches: characteristics of source areas, deposits, and associated eruptions. *Journal of Volcanology and Geothermal Research*, 22:163–197.

Tibaldi, A. (2001). Multiple sector collapses at stromboli volcano, Italy: how they work. *Bulletin of Volcanology*, 63(2):112–125.

Tibaldi, A., Pasquarè, F., Papanikolaou, D., and Nomikou, P. (2008). Discovery of a huge sector collapse at the Nisyros volcano, Greece, by on-land and offshore geological-structural data. *Journal of Volcanology and Geothermal Research*, 177:485–499.

Torres, P., Madeira, J., Silva, L., Brum da Silveira, A., Serralheiro, A., and Mota Gomes, A. (1997). Carta geológica das erupções históricas da Ilha do Fogo: revisão e actualização:.A erupcao vulcanica de 1995 na Ilha do Fogo, Cabo Verde. In *Publ IICT*, pages 119–132. Lisboa, Portugal.

Vales, D., Dias, N. A., Rio, I., Matias, L., Silveira, G., Madeira, J., Weber, M., Carrilho, F., and Haberland, C. (2014). Intraplate seismicity across the Cape Verde swell: A contribution from a temporary seismic network. *Tectonophysics*, 636:325–337.

Ward, S. (2001). Landslide tsunami. *Journal of Geophysical Research*, 106(B6):11201–11215.

Watt, S. F., Talling, P. J., Vardy, M. E., Masson, D. G., Henstock, T. J., Hühnerbach, V., Minshull, T. A., Urlaub, M., Lebas, E., Le Friant, A., Berndt, C., Crutchley, G. J., and Karstens, J. (2012a). Widespread and progressive seafloor-sediment failure following volcanic debris avalanche emplacement: Landslide dynamics and timing offshore Montserrat, Lesser Antilles. *Marine Geology*, 323-325:69–94.

Watt, S. F., Karstens, J., Micallef, A., Berndt, C., Urlaub, M., Ray, M., Desai, A., Sammartini, M., Klaucke, I., Böttner, C., Day, S., Downes, H., Kühn, M., and Elger, J. (2019). From catastrophic collapse to multi-phase deposition: Flow transformation, seafloor interaction and triggered eruption following a volcanic-island landslide. *Earth and Planetary Science Letters*, 517:135–147.

Watt, S. F. L., Talling, P. J., Vardy, M. E., Heller, V., Hühnerbach, V., Urlaub, M., Sarkar, S., Masson, D. G., Henstock, T. J., Minshull, T. A., Paulatto, M., Le Friant, A., Lebas, E., Berndt, C., Crutchley, G. J., Karstens, J., Stinton, A. J., and Maeno, F. (2012b). Combinations of volcanic-flank and seafloor-sediment failure offshore Montserrat, and their implications for tsunami generation. *Earth and Planetary Science Letters*, 319-320:228–240.

Watts, P., Imamura, F., and Grilli, S. T. (2000). Comparing model simulations of three benchmark tsunami generation cases. *Science of Tsunami Hazards*, 18(2):107–124.

Wiemer, G., Moernaut, J., Stark, N., Kempf, P., De Batist, M., Pino, M., Urrutia, R., de Guevara, B. L., Strasser, M., and Kopf, A. (2015). The role of sediment composition and behavior under dynamic loading conditions on slope failure initiation: a study of a subaqueous landslide in earthquake-prone South-Central Chile. *International Journal of Earth Sciences*, 104(5):1439–1457.

Wiemer, G. and Kopf, A. (2016). On the role of volcanic ash deposits as preferential submarine slope failure planes. *Landslides*, 14(1):223–232.

Chapter 4

Emplacement of the Tampen Slide, a buried megaslide offshore Norway

Can a submarine megaslide on a passive margin fail along a single glide plane?

Manuscript II

Rachel Barrett, Benjamin Bellwald, Peter Talling, Felix Gross, Christian Berndt, Aaron Micallef, Sverre Planke, Reidun Myklebust, and Sebastian Krastel

Submitted to the *Journal of Geophysical Research: Solid Earth* on 23.07.2020
Positive reviews received on 25.09.2020
Revised version will be resubmitted soon

Key points

- We use high resolution data to characterise the headwall of the buried submarine Tampen Slide, one of the largest landslides on Earth.
- The first phase of the Tampen Slide involved the simultaneous translation of over 720 km^3 of sediments along a single failure plane.
- This study highlights that retrogression (bottom-up development) may not always account for the large volumes of submarine landslides.

Abstract

Submarine landslides can be several orders of magnitude larger than their terrestrial counterparts, and can pose significant hazards across entire ocean basins. The landslide failure mechanism strongly controls the associated tsunami hazard. The Tampen Slide offshore Norway is one of the largest landslides on Earth, but remains poorly understood due to its subsequent burial beneath up to 450 m of sediments. Here, we use laterally extensive (16,000 km^3), high resolution, processed 3D seismic reflection data to characterise the upper Tampen Slide. We identify longitudinal (downslope, movement-parallel) chutes and ridges that are up-to-40 m high, as well as extensional and compressional (cross-slope) ridges. This is the first time longitudinal ridges of this size have been imaged in a deep marine setting. The first phase of the Tampen Slide involved the simultaneous translation of over 720 km^3 of sediments along a single failure plane. This was followed by spreading along headwalls and sidewalls, and the formation of a retrogressive debris flow and slump, the volumes of which are all insignificant compared to the first failure. The process responsible for movement of such a large volume along a single glide plane differs significantly from that of other passive margin megaslides, which typically comprise numerous smaller landslides that fail retrogressively along multiple planes. The trigger mechanism (e.g. earthquake), the presence of mechanically strong obstructions (e.g. igneous topographical high), and the number and location of weak layers may be key factors that determine whether megaslides develop along a single plane or retrogressively.

Plain Language Summary

Submarine landslides can be significantly larger than those that occur on land, and can cause damaging and widespread tsunami. Furthermore, submarine landslides can also damage critical offshore infrastructure, including telecommunication cables that now carry >95% of global data traffic. However, we still lack fundamental understanding about how such landslides fail. This is critical to understand because it determines the magnitude of associated tsunami. Here we use exceptionally detailed seismic data to understand how one of the largest landslides on Earth (the Tampen Slide offshore Norway) failed. We find that the Tampen Slide failed mainly as a single volume along a single failure surface. This differs significantly from how other giant submarine landslides seem to have failed: in multiple phases, and involving multiple failure surfaces that migrated upslope. This was thought to be the only way that giant submarine landslides developed, with multiple smaller landslides accounting for the large total volume. Here we show for the first time that large submarine landslides can also fail along a single surface across an extensive area, possibly favouring generation of particularly large tsunami. Other large submarine landslides may also fail similarly, and this new model may need to be included in future hazard assessments.

4.1 Introduction

Submarine landslides can be several orders of magnitude larger than their terrestrial counterparts (Korup et al., 2007), and can have devastating and widespread consequences. The submarine landslide itself could destroy critical seabed infrastructure, whilst an associated tsunami could inundate coastlines across ocean basins, impacting communities, global economies and seabed ecosystems (Lintern et al., 2018, and references therein). The way in which a landslide fails strongly determines the scale of an associated tsunami (e.g. Harbitz et al., 2014), and direct hazards to seabed infrastructure. Retrogression, a process whereby failure initiates at the base of the slope and migrates upslope, is widely thought to be the main mechanism by which the largest volume landslides (*megaslides*) develop on passive margins (Masson et al., 2010). The large total volume of these megaslides is typically the result of numerous smaller retrogressive failures, involving multiple headwalls that cut down to different failure (*glide*) planes (e.g. Laberg and Vorren, 2000, Kvalstad et al., 2005, Vanneste et al., 2006, Antobreh and Krastel, 2007, Georgiopoulou et al., 2010, Hill et al., 2019). The Storegga Slide that occurred ca. 8,100 years ago offshore Norway (Figure 4.1) is perhaps the best studied submarine megaslide. It is one of the largest landslides on the planet, and involved a total volume of 2,400 to 3,200 km^3. It failed retrogressively in tens of

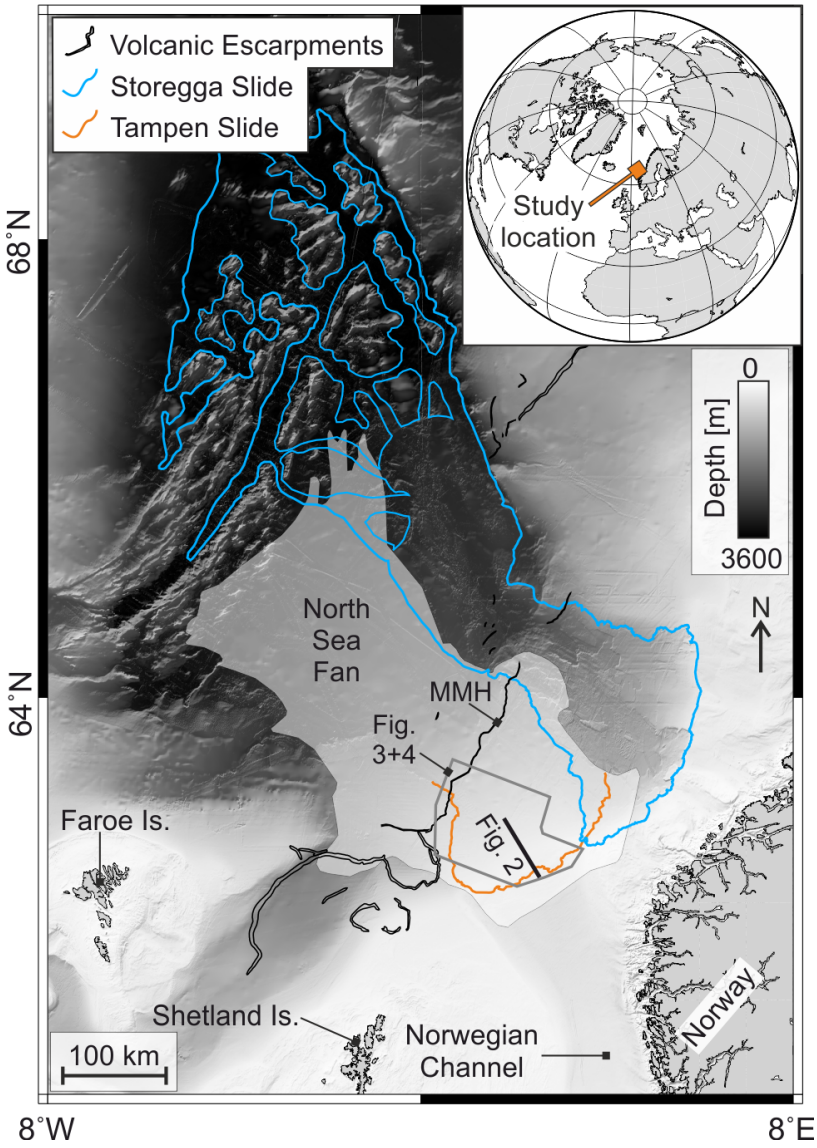

Figure 4.1: Map showing the location of the buried Tampen Slide headwall within the North Sea Fan offshore Norway. Regional volcanic escarpments after Zastrozhnov et al. (2020). MMH: Møre Marginal High.

phases, along multiple glide planes (Haflidason et al., 2004, Kvalstad et al., 2005, Micallef et al., 2009), and the resulting tsunami inundated coastlines across the North Sea, with a run-up of up to 25 m at the Shetland Islands (Bondevik et al., 2005).

The Tampen Slide, an older and perhaps even larger submarine megaslide, is located in a similar position to the Storegga Slide (Figure 4.1). However, the emplacement of the Tampen Slide remains poorly understood. This is largely due to its subsequent burial under up to 450 m of sediment, and partial remobilisation by the Storegga Slide. Several previous studies have analysed the character of the Tampen Slide (Evans et al., 1996, Nygård et al., 2005, Gafeira et al., 2010, Hjelstuen and Grinde, 2016). These studies, however, are based

on rather widely-spaced 2D seismic profiles, and local 3D seismic surveys, and the character of the Tampen Slide deposits and glide plane within the headwall region remain poorly constrained.

Here we make use of extensive (~16,000 km^2), high resolution, processed 3D seismic reflection data that cover the headwall area of the Tampen Slide. We characterise the megaslide's morphology, and thereby understand its emplacement mechanism. We then compare the Tampen Slide with other megaslides on passive margins, and determine if there are significant differences in their emplacement mechanisms. We discuss possible reasons for these differences, and their implications for tsunami generation and geohazards.

4.2 Geological Setting

The Tampen Slide occurred within the deposits of the North Sea Fan offshore Norway (Figure 4.1). The North Sea Fan is a trough mouth fan that comprises glacigenic sediments (flow deposits that accumulated very rapidly at the termination of an ice stream) and contourites that accumulated between ice sheet advances (Nygård et al., 2005). In addition, multiple submarine landslides are found within the North Sea Fan, several of which have total volumes exceeding 1,000 km^3 (King et al., 1996, Nygård et al., 2005, Hjelstuen and Grinde, 2016). The most recent of these megaslides, the Storegga Slide, is exposed at the seafloor and is dated at 8.1 ka (Haflidason et al., 2005). The timing of megaslides offshore Norway has been suggested to correspond with the transition from a glacial to an interglacial period (Bryn et al., 2005). In this model, the occurrence of megaslides correlates strongly with glacial cycles: the slides are preconditioned by sedimentary loading during glacial periods, and then triggered by a large earthquake during the process of glacial rebound (Bryn et al., 2005, Kvalstad et al., 2005, Bellwald et al., 2019b).

The giant Tampen Slide is buried beneath up to 450 m of glacigenic sediments and contourites within the North Sea Fan (Figure 4.2). In keeping with the previous model (Bryn et al., 2005) and based on the results of numerical modelling, Bellwald et al. (2019a) suggest that the Tampen Slide was preconditioned by the rapid deposition of glacial sediments and then triggered by an earthquake. Its headwall is bound by the Norwegian continental shelf on its eastern and southern sides, and by the volcanic Møre Marginal High on the west (Figure 5.1). The Møre Marginal High is one of a series of volcanic structural highs offshore Norway, and its eastern boundary is known as the Faroe-Shetland Escarpment (Kiørboe, 1999). The subsequent Storegga Slide remobilized Tampen Slide deposits west of the headwall area. Burial and remobilization of the Tampen Slide deposits have hindered its investigation. Previous studies have suggested that the Tampen Slide mobilized a total

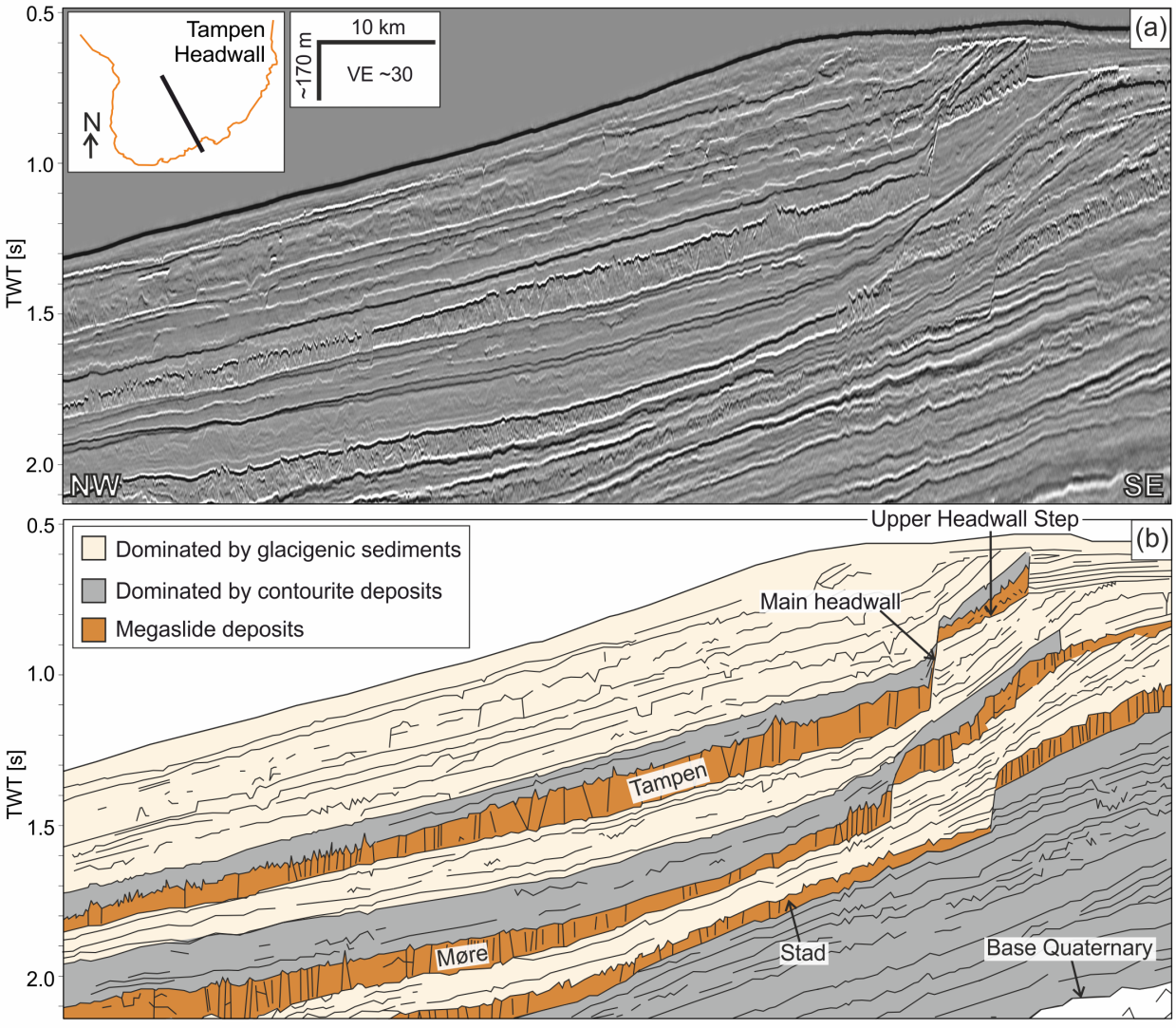

Figure 4.2: Seismic section crossing the headwall of the Tampen Slide, showing (a) migrated data, and (b) interpretation. Note that the Tampen Slide is overlain by up to 450 m of glacigenic sediments and contouritic deposits. The location of this profile is shown by the black line in the inset panel. See Figure 4.1 for the location of the Tampen headwall. VE: Vertical Exaggeration. Profile from the AMS17 Vol. A dataset and courtesy of TGS.

of 1,400 km^3 of sediment (Nygård et al., 2005), but this estimate is based on widely spaced 2D seismic reflection profiles, and is thus associated with significant uncertainty. The estimated age of the Tampen Slide (130 ka; Nygård et al., 2005) is also based on regional seismic correlation and is also poorly constrained (Watts et al., 2016, Pope et al., 2018).

4.3 Data and Methodology

We make use of 3D migrated seismic reflection data (AMS17; Figure 4.1) that were acquired by TGS in 2017. These data cover an area of ∼16,000 km^2, and were collected using a triple-sourced airgun array with a total volume of 3,000 in^3 and a shot point interval of 12.5 m. The acquisition system consisted of 12 streamers separated by 112.5 m. The streamers were 8,100 m long and were towed in water depths of 7 to 12 m.

The two seismic volumes used in this study are i) Volume A, which has 4 ms sampling and 12.5 m x 18.75 m bin size; and ii) Volume B: a shallow, high resolution volume with a 2 ms sample rate and 6.25 m x 18.75 m binning. Volume B was processed with the aim of increasing the resolution of shallow targets and hazards. However, this volume only extends to the first multiple, which cuts through the Tampen Slide near its eastern headwall.

The upper and lower surfaces of the Tampen Slide were picked at increments of 150 m (every 8th inline with an inline spacing of 18.75 m) using the software IHS Kingdom. The bounding surfaces were defined as the highest amplitude peak that corresponds with the horizons immediately overlying and underlying the slide deposits (Figure 4.2). In regions with a higher amount of morphologic variation, picking was conducted at higher density, and included the interpretation of crosslines. The interpreted lines were gridded using continuous curvature splines with adjustable tension (GMT 5.4.5 *surface* routine; Smith and Wessel, 1990), and the grid was snapped to the maximum amplitude within a vertical window of 10 ms centered on the picked horizon. The structure and amplitude maps, as well as the seismic profiles, were then used for geomorphological analysis of the slide. Two-way travel time (TWT) was converted to depth using a uniform velocity of 1700 m/s (after Nygård et al., 2005), in order to calculate the thickness of units.

4.4 Results: Morphology of the Tampen Slide

The horseshoe-shaped main headwall of the Tampen Slide extends for >350 km, and encompasses an area >25,500 km^2 (Figure 4.1). The main headwall is 150 m high, and is encircled by a secondary headwall step that was first identified by Nygård et al. (2005) and is up to 200 m high (Figures 4.2 and 4.3). A large amount of failed material (∼845 km^3) remains within the surveyed region of the Tampen Slide's headwall. In the following sections, we describe the morphology of the Tampen Slide's failure surface (glide plane) and the deposits that remain within the surveyed region of the headwall.

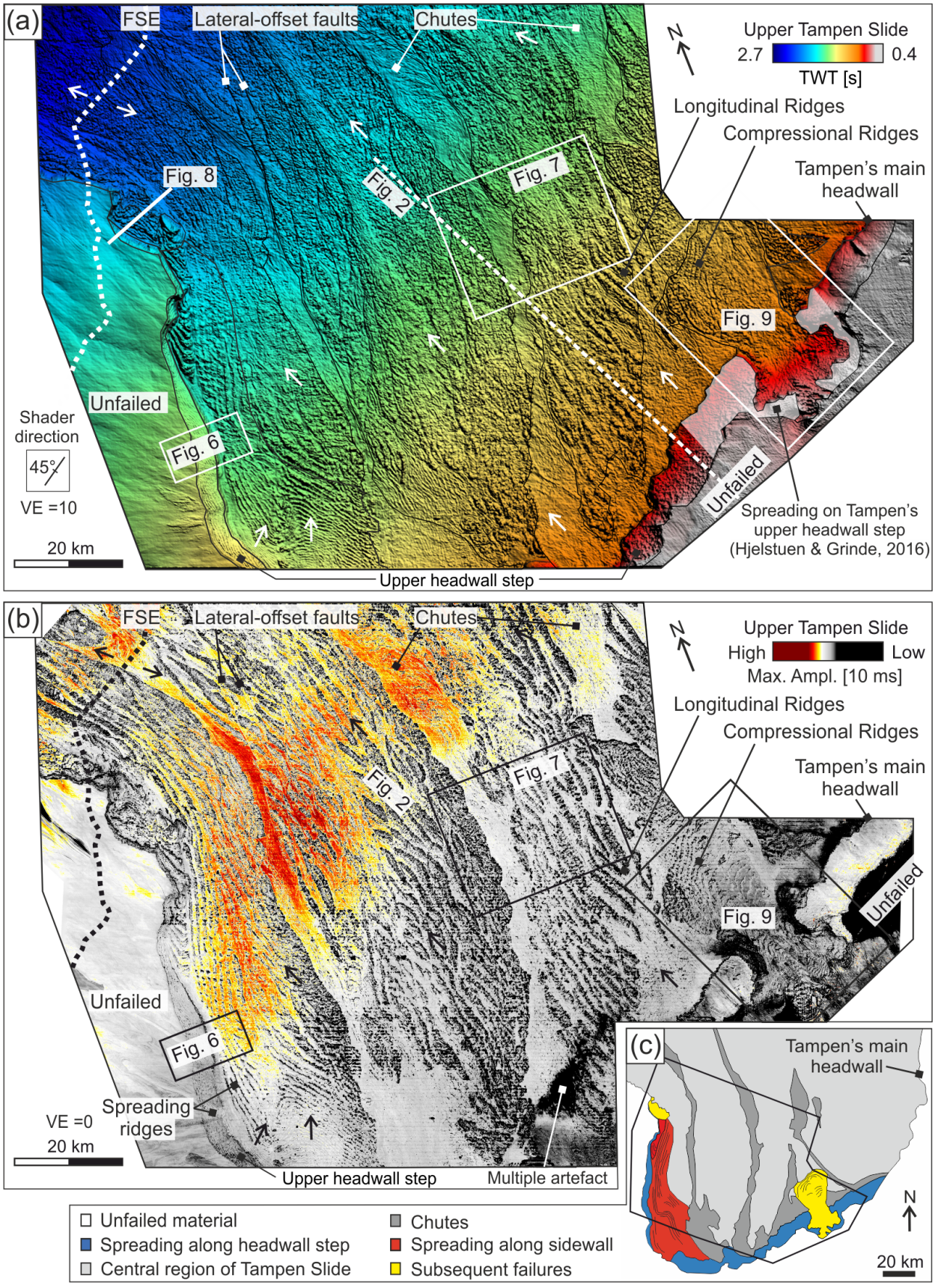
(a)
FSE
Lateral-offset faults
Chutes
N
Upper Tampen Slide
2.7
0.4
TWT [s]
Longitudinal Ridges
Compressional Ridges
Tampen's main headwall
Fig. 8
Fig. 2
Fig. 7
Fig. 9
Unfailed
Fig. 6
Shader direction
45°
VE =10
20 km
Unfailed
Spreading on Tampen's upper headwall step (Hjelstuen & Grinde, 2016)
Upper headwall step
(b)
FSE
Lateral-offset faults
Chutes
N
Upper Tampen Slide
High
Low
Max. Ampl. [10 ms]
Longitudinal Ridges
Compressional Ridges
Tampen's main headwall
Fig. 2
Fig. 7
Fig. 9
Unfailed
Unfailed
Fig. 6
Spreading ridges
VE =0
20 km
Upper headwall step
Multiple artefact
(c)
Tampen's main headwall
N
20 km
Unfailed material
Spreading along headwall step
Central region of Tampen Slide
Chutes
Spreading along sidewall
Subsequent failures

Figure 4.3 *(previous page)*: Upper surface of the Tampen Slide: (a) two-way travel time (TWT); and (b) maximum amplitude within a 10 ms vertical window of the picked TWT horizon. Note that the band of high amplitudes through the northern-central region of the slide deposits corresponds with where the deposits are thinner (see Figure 4.9). Locations of subsequent figures in this chapter are indicated by the boxes. Small white arrows: slope direction of the glide plane; white dashed line: Faroe-Shetland Escarpment (FSE); VE: Vertical Exaggeration. (c) Geomorphologic map highlighting the main types of debris within the Tampen Slide headwall region. A regional pseudo-3D cube (J-Cube MN; Whiteside et al., 2013) was used to extend the headwall of the Tampen Slide beyond the limits of AMS17. Data from AMS17 Vol. B and courtesy of TGS.

4.4.1 The glide plane

The Tampen Slide's glide plane follows underlying stratigraphy, and dips gently (<1° on average) north-northwest, except at the southwest corner of the headwall where it dips towards the northeast (Figure 4.4). The maximum amplitude map of the basal plane (Figure 4.4b) is dominated by high amplitudes along the western sidewall. The central region of the Tampen Slide's basal plane is characterised by medium to low amplitude stripes (>20 km wide) that are aligned downslope. The glide plane is largely smooth, although we identify parallel linear scours along the western side of the headwall and within the western-central region of the headwall, and parallel steps in the northern reaches of the surveyed region (Figures 4.4 and 4.5).

The parallel linear scours along the western side of the headwall (Figure 4.4a) correspond to overlying patterns of deformation (linear ridges) within the slide debris (Figure 4.6). The erosional scour marks within the western-central region of the headwall correspond with a change in the maximum amplitude of the glide plane (Figure 4.4b), as well as a variation in the nature of the overlying slide deposits. The slide deposits to the west of this divide are characterised by linear ridges, orientated parallel to the headwall, and with visible internal horizons (discussed in Section 4.4.2). East of this divide, the internal structure of the slide debris is chaotic, with no mappable internal horizons. In the northern reaches of the headwall region, the glide plane steps down to a lower stratigraphic level and then back up again across two parallel steps (Figure 4.5).

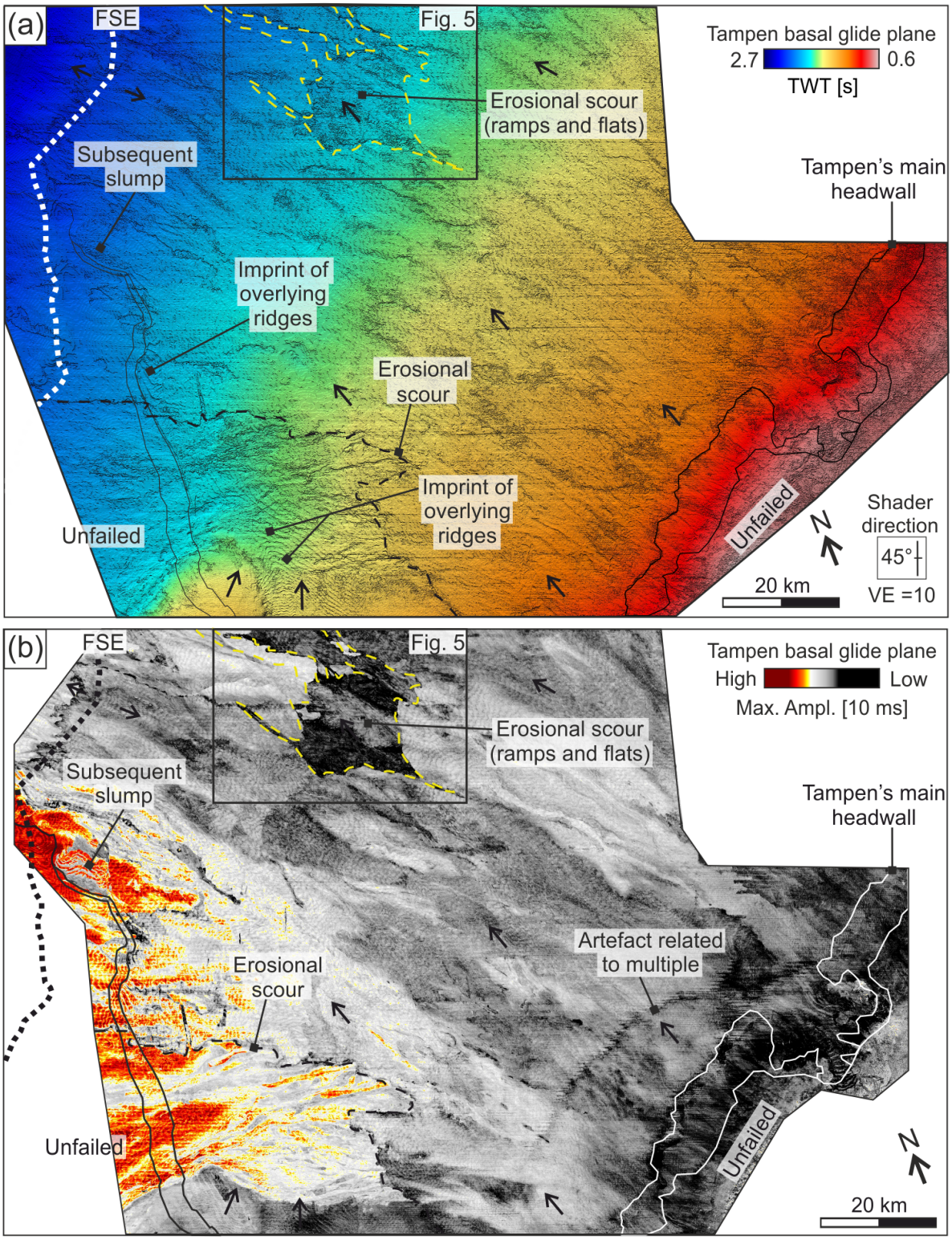

Figure 4.4: The Tampen Slide's basal glide plane: (a) two-way travel time (TWT); and (b) maximum amplitude within a 10 ms vertical window of the picked TWT horizon. Small black arrows: slope direction of the glide plane; white/black dashed line: Faroe-Shetland Escarpment (FSE); VE: Vertical Exaggeration. Data from AMS17 Vol. A and courtesy of TGS.

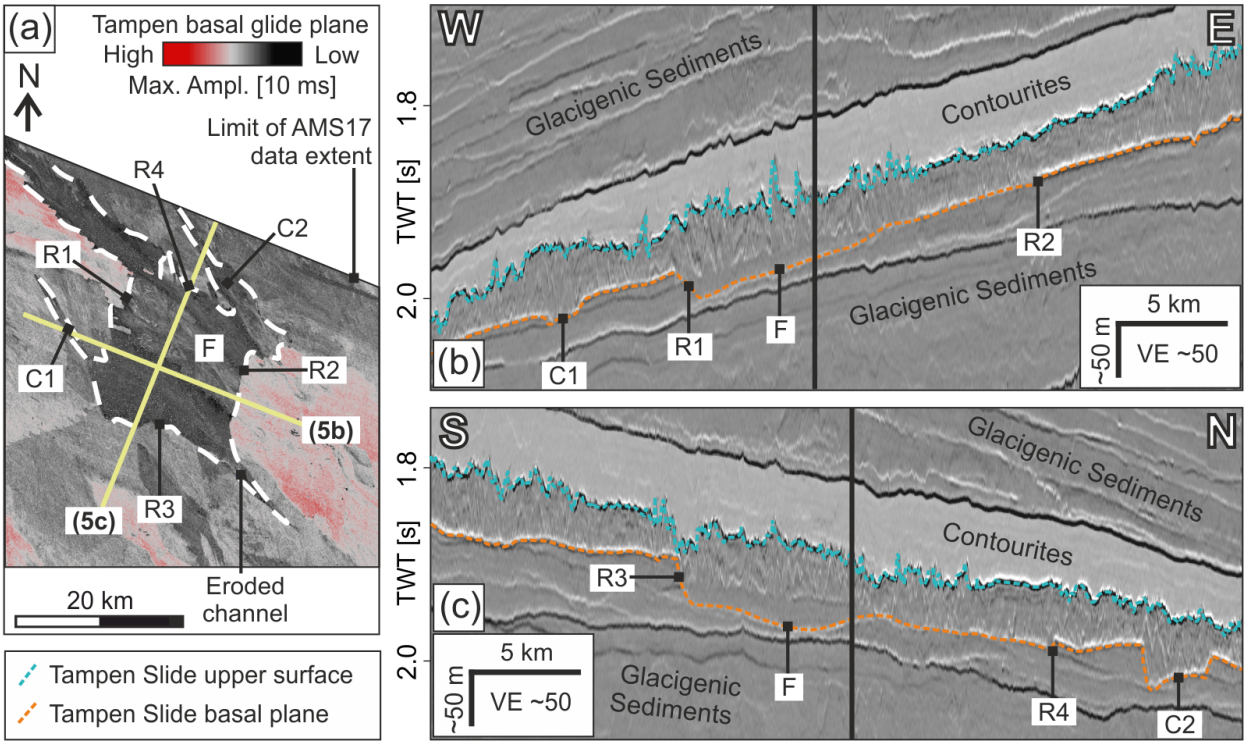

Figure 4.5: Eroded ramps, flats and channels in the northern reaches of the study area. (a) Maximum amplitude surface within a 10 ms vertical window of the picked basal plane. See Figure 4.4 for location. (b, c) Seismic profiles crossing the eroded ramps, flats and channels. Black line: profile crossing point; C1/C2: eroded channels; F: eroded flat section; R1/R2/R3/R4: ramps; VE: Vertical Exaggeration. Data from AMS17 Vol. A, and courtesy of TGS.

4.4.2 Extensional ridges along the western sidewall and on the upper headwall step

Along the western sidewall, elongated ridges are observed parallel to the headwall scarp (Figures 4.3 and 4.6). The interior of these ridges is increasingly chaotic with distance from the scarp (eastwards) (Figure 4.6), and associated deformation extends through the full thickness of the deposits, imprinting onto the glide plane below (Figure 4.4a). These ridges are spaced at ~2 km intervals, and cover ~850 km^2. They stand up to 290 m above the glide plane, and decrease in height with distance from the scarp (Figure 4.6).

Similar headwall-parallel ridges are also present along the upper headwall step (Figure 4.6). These ridges are spaced 700-1,000 m apart, and are up to 120 m high. With distance from the scarp, the ridges both decrease in height and have a more chaotic interior.

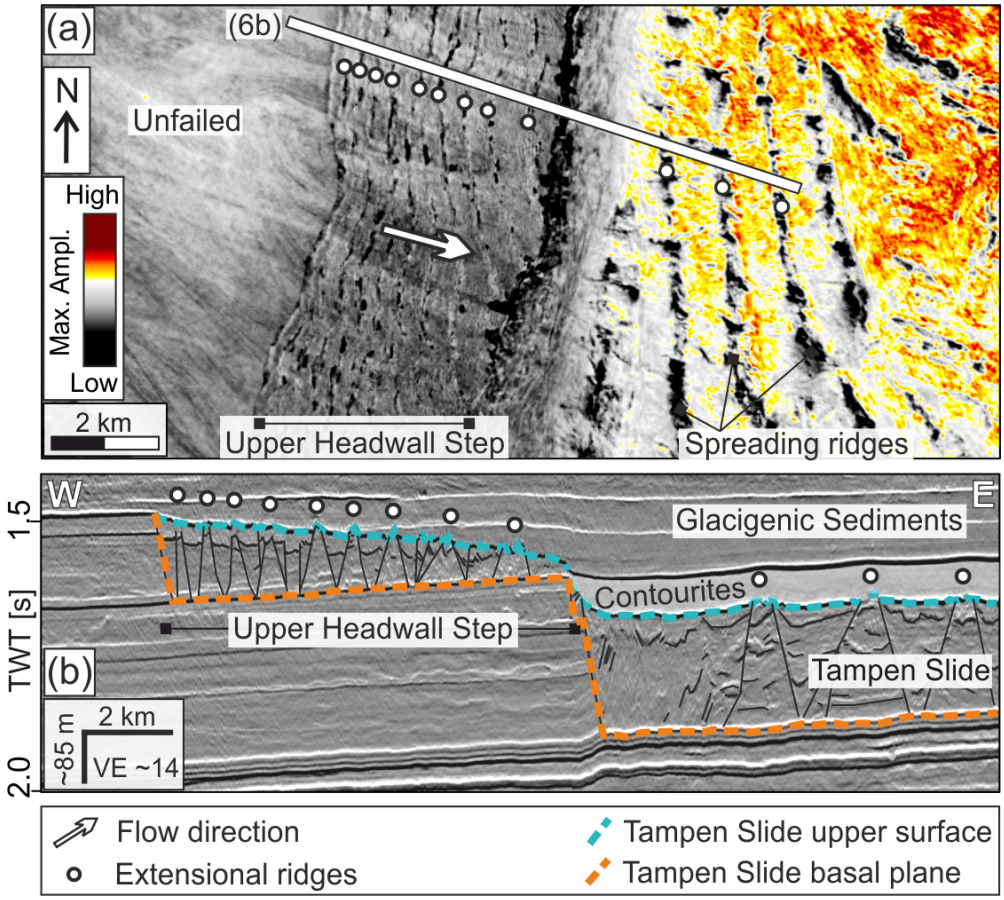

Figure 4.6: Extensional ridges (spreading) along the upper headwall step and along the western sidewall of the Tampen Slide. (a) Maximum amplitude of the Tampen Slide's upper surface, and (b) seismic profile highlighting the character of the spreading ridges. Location of this figure is shown in Figure 4.3. VE: Vertical Exaggeration. Data from AMS17 Vol. B, and courtesy of TGS.

4.4.3 Longitudinal chutes and ridges within the slide deposits

Elongated chutes, up to 10 km wide and more than 120 km long, are imaged within the slide deposits (Figure 4.3). These chutes are characterized by a comparatively smooth, high amplitude upper surface (Figures 4.3b and 4.7). The chute boundaries are marked by lateral-offset faults that extend through the whole interior of the slide debris, and commonly coincide with a topographical variation on the upper surface of the slide (Figure 4.7). There is no consistent variation on the glide plane to explain why chutes preferentially form in specific locations, although the edges of the centremost chute coincide with the erosional feature noted on the basal plane in the northern region of the study area (Figure 4.5; Section 4.4.1).

Prominent downslope-elongated (longitudinal) ridges are also present within the Tampen Slide deposits (Figures 4.3 and 4.7). These ridges are irregularly spaced and up to 40 m higher than the surrounding debris. Their height distinguishes them from flowlines, which

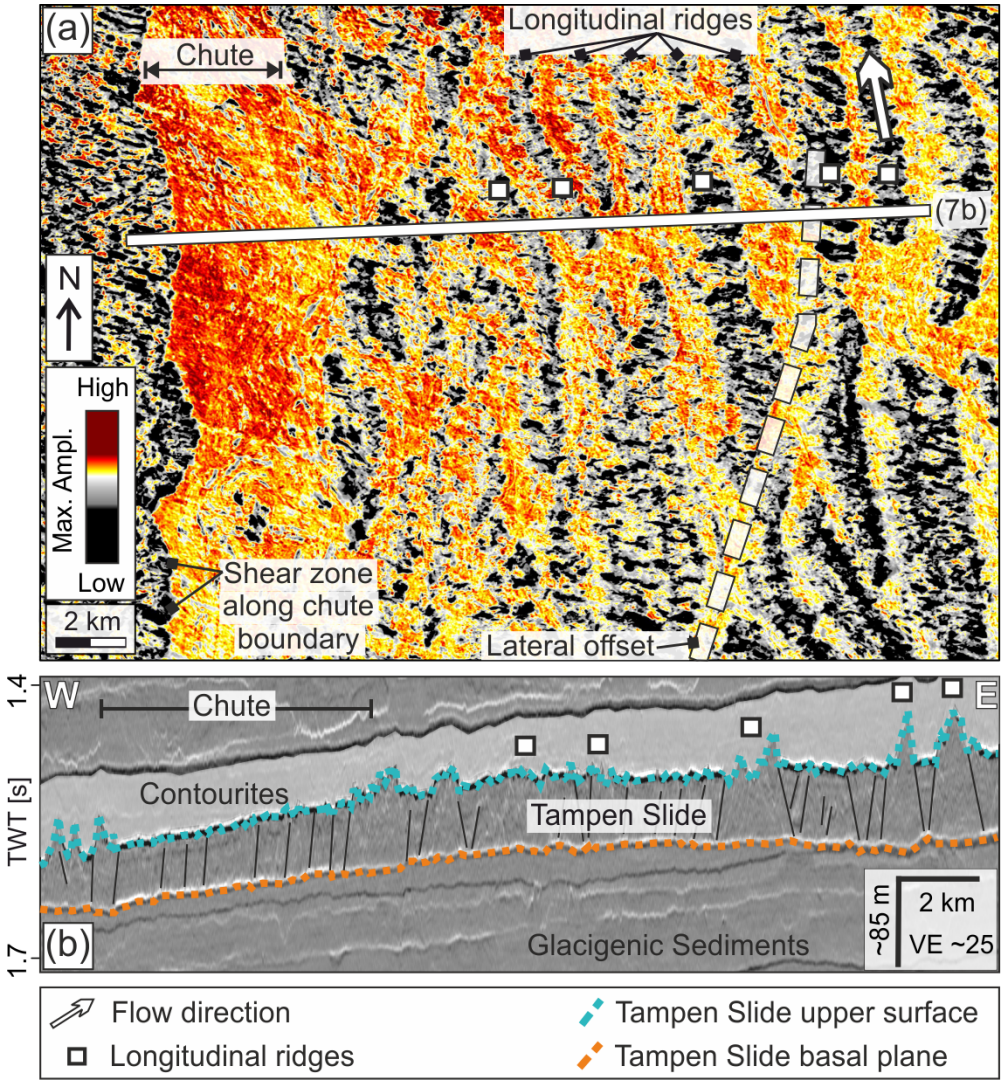

Figure 4.7: Longitudinal ridges and chutes within the Tampen Slide deposits. (a) Maximum amplitude of the Tampen Slide's upper surface, and (b) seismic profile highlighting the character of the longitudinal ridges and chutes. Note the high level of internal deformation of the slide deposits here, within the central region of the headwall, in comparison with those along the western side of the headwall (Figure 4.5; from the same data volume). Location of this figure is shown in Figure 4.3. VE: Vertical Exaggeration. Data from AMS17 Vol. B, and courtesy of TGS.

typically have relief <1 m (Masson et al., 1993, Bull et al., 2009), and their downslope orientation also distinguishes them from slump folds, which have similar geomorphology but are perpendicular to the direction of motion (Bull et al., 2009). Unlike for the ridges along the western sidewall, the glide plane beneath these ridges is devoid of topographical variations.

4.4.4 Secondary failures of the Tampen Slide headwall

We also image two smaller volume failures along the Tampen Slide headwall. The first failure, on the western side of the headwall (Figure 4.8), consists of a series of irregularly-shaped blocks and wavy fabric on the upper surface. The deformation extends through the full interior of these blocky deposits, imprinting onto the partially eroded basal plane below. This slump has a volume of ~12 km^3 and its limit is delineated by an upward step in the basal glide plane (Figure 4.8).

The second subsequent failure, on the eastern side of the Tampen Slide's main headwall, has a cauliflower-shaped headwall (Figure 4.9). Along-slope-orientated elongated ridges are present both at the headwall and within the toe region of this failure. The ridges within the headwall region are similar to those described in Section 4.4.2, along the upper step of the headwall and along the western sidewall. The ridges within the toe region of this comparatively small volume (~36 km^3) failure have a chaotic interior and minimal topographic signature (Figure 4.9b).

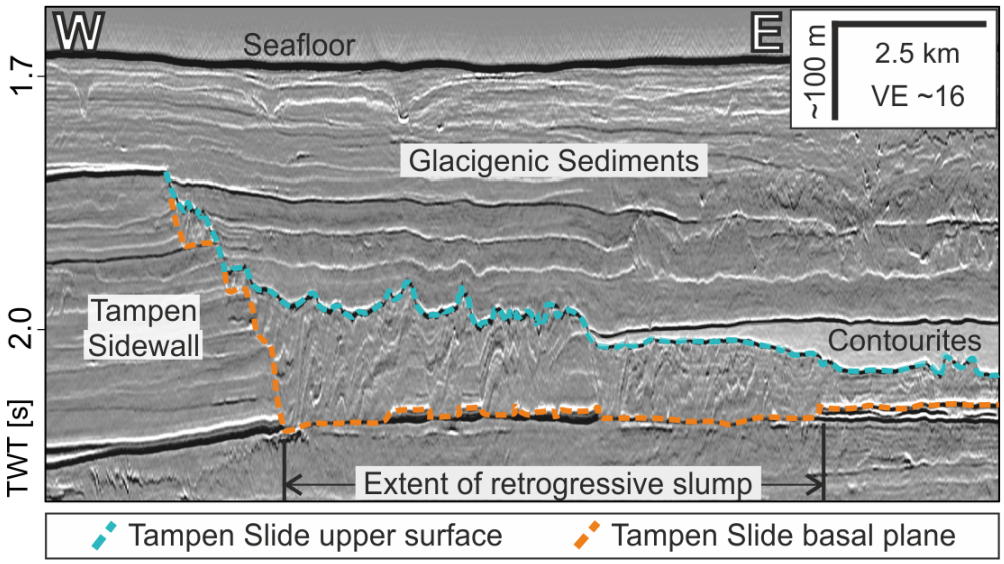

Figure 4.8: Seismic profile crossing a small volume (~12 km^3), retrogressive slump on the western sidewall of the Tampen Slide. Note the blocky character of the slump deposits. Location of this figure is shown in Figure 4.3. VE: Vertical Exaggeration. Data from AMS17 Vol. B, and courtesy of TGS.

Figure 4.9 *(next page)*: The ~36 km^3 retrogressive debris flow on the eastern headwall of the Tampen Slide. (a) Maximum amplitude of the Tampen Slide's upper surface, and (b) seismic profile highlighting the character of the compressional ridges at the toe of this failure. Location of this figure is shown in Figure 4.3. VE: Vertical Exaggeration. Amplitude data from AMS17 Vol. B, and seismic profile from AMS17 Vol. A. Data courtesy of TGS.

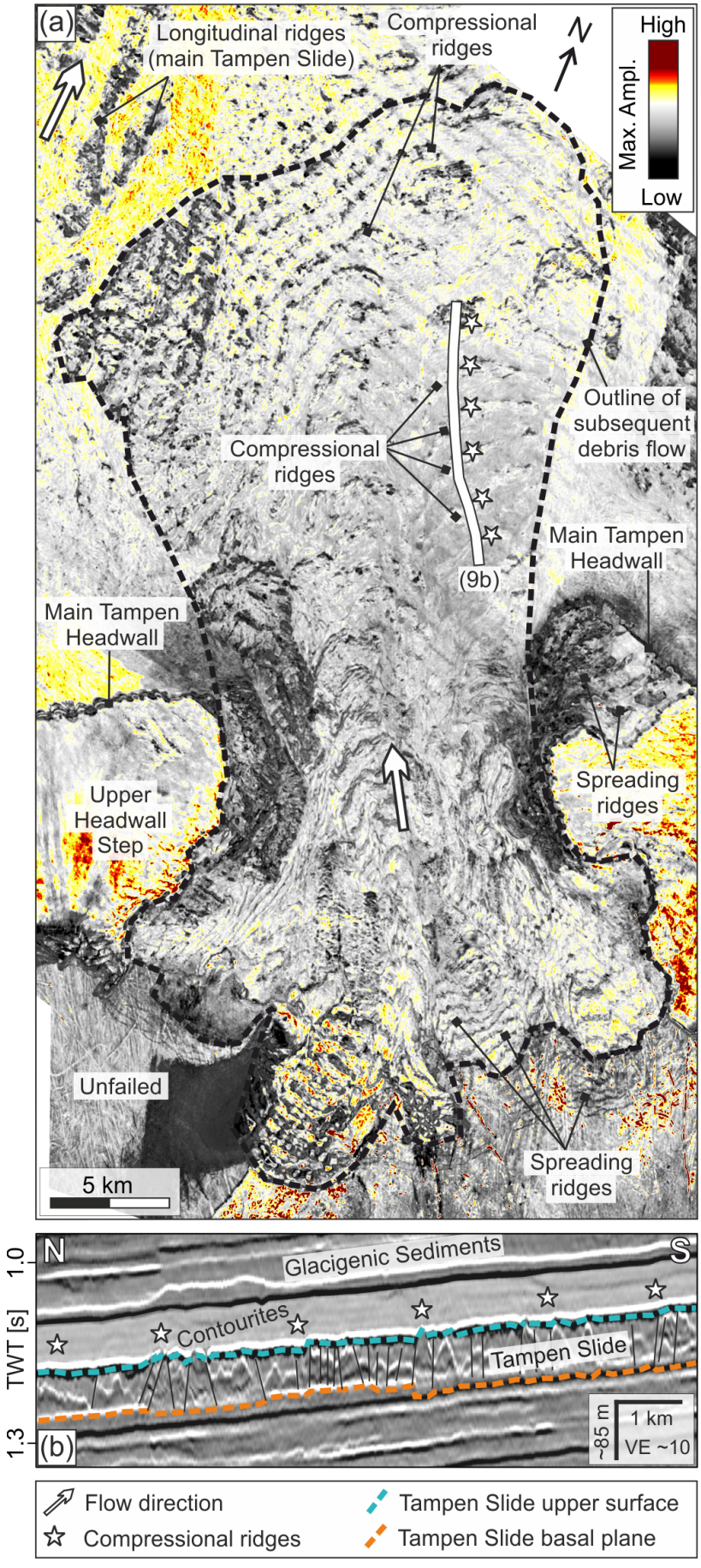
(a)
Longitudinal ridges
(main Tampen Slide)
Compressional
ridges
N
High
Max. Ampl.
Low
Outline of
subsequent
debris flow
Compressional
ridges
(9b)
Main Tampen
Headwall
Main Tampen
Headwall
Upper
Headwall
Step
Spreading
ridges
Unfailed
5 km
Spreading
ridges
N
S
Glacigenic Sediments
Contourites
Tampen Slide
1.0
TWT [s]
1.3
(b)
~85 m
1 km
VE ~10
Flow direction
Compressional ridges
Tampen Slide upper surface
Tampen Slide basal plane

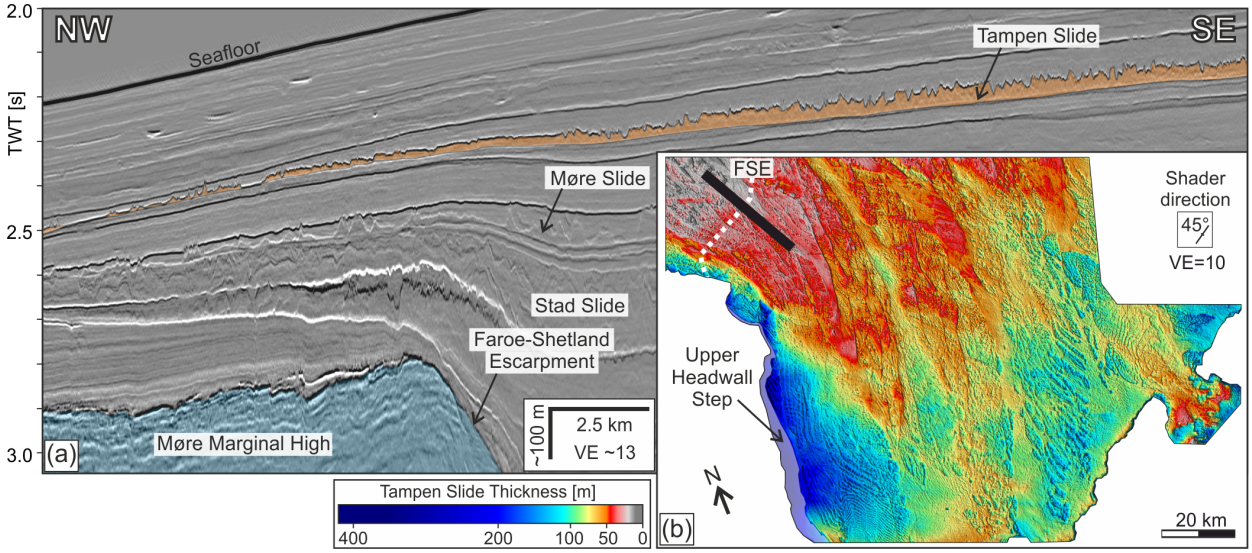

Figure 4.10: The deposits of the Tampen Slide thin over the Faroe-Shetland Escarpment (FSE). (a) Seismic profile crossing the FSE; and (b) Thickness map highlighting the distribution of the Tampen Slide deposits within the Tampen Slide headwall region. The deposits are at their thickest along the western sidewall, where they are characterised by ridges and troughs characteristic of spreading (Figure 4.5), and thinnest west of the FSE. Black line shows the location of the seismic profile in (a); VE: Vertical Exaggeration. Seismic profile from AMS17 Vol. A. Data courtesy of TGS.

4.4.5 Thinning of the Tampen Slide over the Faroe-Shetland Escarpment

The deposits of the Tampen Slide thin towards the north-western corner of the data coverage, and most notably over the Faroe-Shetland Escarpment, the eastern boundary of the volcanic Møre Marginal High (Figure 4.10). On the eastern side of this divide, the deposits are generally 40-50 m thick, but thin to <20 m thick on the western side.

4.5 Discussion

The high resolution and extensive coverage of these 3D seismic data constrain the character of the Tampen Slide. In this section, we discuss how the Tampen Slide morphology provides new insights into how it was emplaced. We then compare the morphology and emplacement mechanism of the Tampen Slide to other megaslides on passive margins, and conclude by outlining a new megaslide failure model and its implications for tsunami generation.

4.5.1 Emplacement of the Tampen Slide

4.5.1.1 The main failure

The smoothness of the basal plane (Figure 4.4a), the broad (>20 km wide), downslope-orientated stripes of varying maximum amplitude of the basal plane (Figure 4.4b), and the continuity of internal deformation across the slide deposits (e.g. Figures 4.2, 4.7, and 4.10) indicate that the material largely failed as one along a single stratigraphic horizon. Consequently, we suggest that the initial failure began at the southern edge of the headwall, and propagated ∼290 km northwards along the eastern side of the headwall, remobilizing in excess of 720 km^3 of sediments (the volume that remains within the extent of the surveyed area) (Figure 4.11b).

Longitudinal chutes and ridges within the slide deposits

Within the deposits of the Tampen Slide, we identify downslope-elongated (longitudinal) chutes (Figure 4.7; Section 4.4.3). These are similar to longitudinal chutes that have been documented in landslides at fjord-head deltas (e.g. Kitimat Arm in British Columbia; Prior et al., 1981) and in deposits of the Storegga Slide (Bugge et al., 1988), where they have been interpreted as regions of faster motion within the debris. Consequently, we suggest that varying flow speeds within the failed material resulted in the development of these longitudinal chutes within the Tampen Slide deposits.

We also observe up to 40 m high, longitudinal ridges within the slide deposits (Figure 4.7; Section 4.4.3). While such large-scale longitudinal ridges are frequently present in terrestrial and volcanic landslide deposits (e.g. Dufresne and Davies, 2009, and references therein), this is the first time, to our knowledge, that they have been observed in a deep marine environment. Simple laboratory studies indicate that the formation of longitudinal ridges depends upon lateral segregation of grains at the front of the debris flow (Pouliquen et al., 1997, Dufresne and Davies, 2009). The grains are segregated according to size and shape, where the ridges are made up of coarser, more angular particles, while finer-grained material fills the central channels (Valderrama et al., 2017). While these studies are certainly simplified compared to the natural case, the authors (Pouliquen et al., 1997, Dufresne and Davies, 2009, Valderrama et al., 2017) found that their results were consistent with the character of debris avalanche deposits in several locations. The development of longitudinal ridges also seems to require high basal shear, which arises as a result of mechanical differences between the glide plane and the overlying material (Dufresne and Davies, 2009). In glacial environments, this is often attributed to the presence of an icy basal layer; however, based on wavelength analyses of ridges within a Martian landslide, Magnarini et al. (2019) suggested

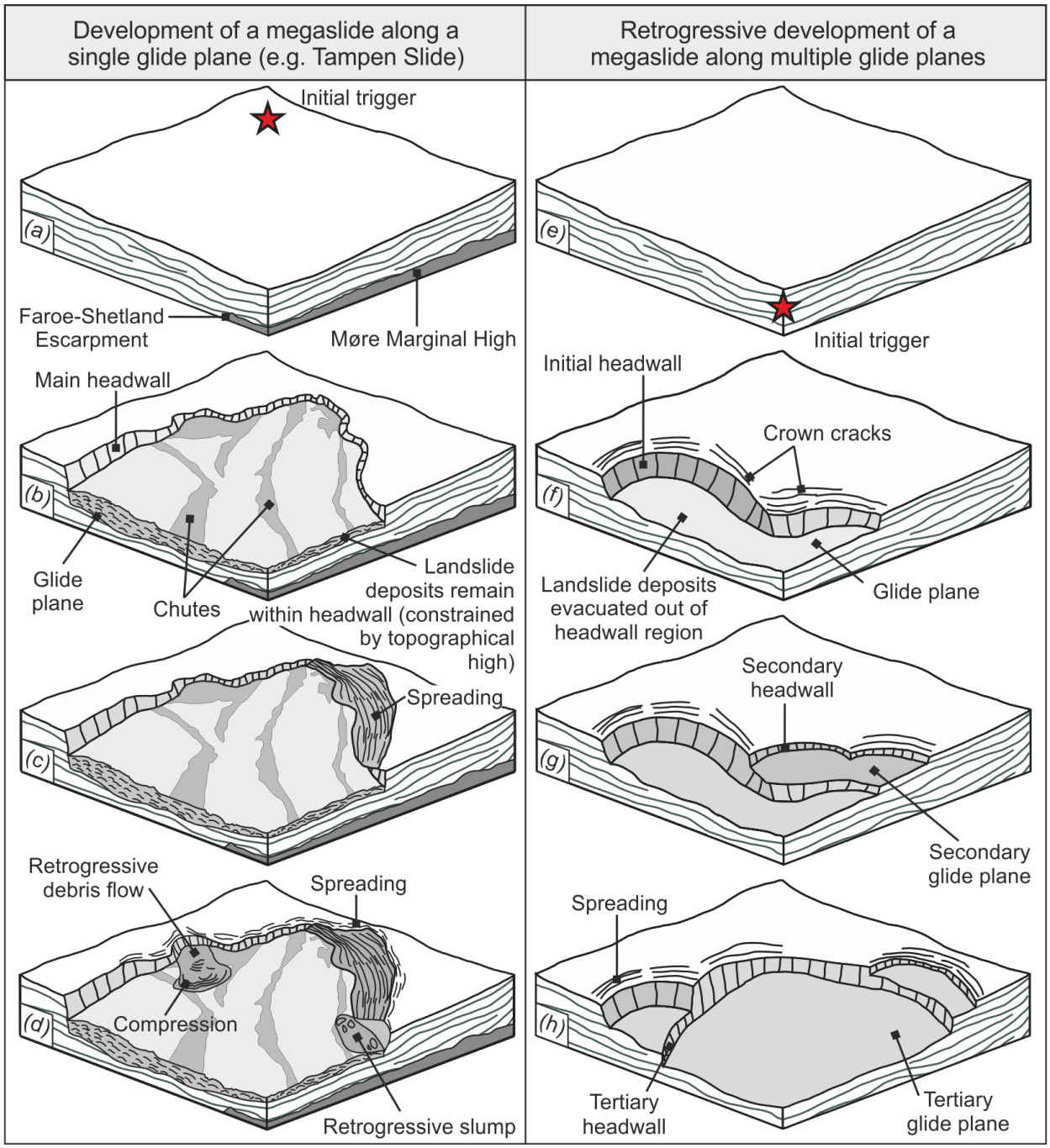

Figure 4.11: Conceptual models showing (a-d) development of a megaslide along a single glide plane (as for the Tampen Slide); and (e-h) upslope-migrating failure across multiple glide planes (responsible for the large total volume of other passive margin megaslides, such as the Storegga, Trænadjupet, Hinlopen/Yermak, Sahara, and Cape Fear Slides).

that longitudinal ridges are inevitable once a kinematic threshold within the rapidly failing mass is exceeded. Furthermore, longitudinal ridges seem more likely to develop in flows where the longitudinal velocity is much greater than the lateral velocity, such as in cases where the flow is laterally constrained (Dufresne and Davies, 2009).

Diversion around the Faroe-Shetland Escarpment

The deposits of the Tampen Slide thin across the Faroe-Shetland Escarpment (Figure 4.10). This near-linear variation in thickness across this eastern margin of the Møre Marginal High leads us to suggest that the Møre Marginal High acted as a topographic constraint, which prevented the Tampen Slide deposits from continuing their downslope run-out away from the continental margin. This resulted in a large volume of sediments remaining proximal to the headwall (Figure 4.11b), rather than being evacuated out of the headwall region, as is typical for megaslides on passive margins (Figure 4.11f; e.g. Kvalstad et al., 2005, Vanneste et al., 2006, Li et al., 2017, Hill et al., 2019). Additionally, the lateral constraints and corresponding shift in the direction of transport of the failed mass may also have aided the development of the <40 m high longitudinal ridges identified within the slide deposits (Figure 4.7).

The erosional feature in the northern part of the headwall region (Figure 4.5), including the two steps and the interlinking portion of the glide plane, is orientated roughly parallel to the failure direction (downslope), and bears striking similarity to features that have been described as ramps and flats (e.g. Trincardi and Argnani, 1990, Frey-Martínez et al., 2005, Bull et al., 2009, Omosanya and Alves, 2013). Ramps and flats have been observed in many major slides, including the Møre Slide that is buried beneath the Tampen Slide (Evans et al., 1996, Bull et al., 2009), and have been suggested to occur where there are multiple, low shear strength layers or localised erosion during translation of the failed mass (Strachan, 2002, Bull et al., 2009). We suggest that the slowing and/or redirection of the failed deposits around the Faroe-Shetland Escarpment could account for the location of these ramps and flats on the basal plane of the Tampen Slide.

4.5.1.2 Spreading along the western sidewall and the upper step

The ridges observed along the upper step of the headwall and along the western side of the headwall decrease in height and have a more chaotic interior with distance from the head- and sidewall (Figure 4.6). These characteristics are typical of ridges that have elsewhere been associated with spreading - a process thought to result from seismic loading and loss of basal support (Lastras et al., 2003, Micallef et al., 2007). Hjelstuen and Grinde (2016) identified spreading ridges in a small area on the upper step of the Tampen Slide's headwall

(∼270 km^2; Figure 4.3a). The lateral extent of our data enables us to map spreading across ∼860 km^2 of the upper headwall step (Figure 4.3c).

We suggest that this spreading, both along the upper step of the headwall and along the western side of the headwall, occurred in response to loss of support following the first phase of failure. The spreading along the base of the western sidewall, (incorporating ∼125 km^3 of sediment), began in the south where the basal plane dips towards the north (Figure 4.4), and extended northwards along the sidewall (Figure 4.11c). This corresponds with the region that is characterised by very high basal plane amplitudes along the western sidewall (Figure 4.4b). This was followed by spreading along the top step of the head- and sidewall (Figures 4.3, 4.6, and 4.11d).

4.5.1.3 Retrogressive failures of the Tampen Slide headwall

The blocky nature of the ∼12 km^3 slump on the western sidewall (Figure 4.8), as well as its clearly defined limit, which is demarcated by an upward step on the basal glide plane, lead us to interpret it as a retrogressive slump that was emplaced following the main Tampen Slide (Figure 4.11d). The cauliflower shape of the headwall of the debris flow on the eastern side of the Tampen Slide's headwall (Figures 4.9 and 4.11d), similarly, has previously been linked to retrogressive landslide development (Micallef et al., 2008). The ridges at the headwall and toe of this debris flow are consistent with ridges that result from extensional spreading and compression, respectively (Bull et al., 2009). The timing of this slump and debris flow, as well as that of the spreading along the upper step of the headwall, is poorly constrained, and could have occurred minutes, hours, or even many years after the main Tampen Slide event.

4.5.2 Comparison to other passive margin megaslides

4.5.2.1 Retrogressive development

Most megaslides worldwide are thought to have developed retrogressively, with numerous failures across multiple headwalls and glide planes typically accounting for their total volume (e.g. Laberg and Vorren, 2000, Kvalstad et al., 2005, Vanneste et al., 2006, Antobreh and Krastel, 2007, Georgiopoulou et al., 2010, Hill et al., 2019). It is clear that some relatively small retrogressive failures occurred at the Tampen Slide headwall following the first phase of failure (Figures 4.8, 4.9, and 4.11a-d). However, the Tampen Slide deviates from other megaslides on passive margins (Figure 4.11e-h) in that initial failure of the Tampen Slide seems to have involved a prodigious volume of sediments (>720 km^3) that were translated

as one mass along a single glide plane, accounting for the majority of the total failed volume. In comparison, the neighbouring Storegga Slide has been suggested to have failed in tens of (more than seventy) phases (Haflidason et al., 2004, Micallef et al., 2009). This difference is significant because these slides both occurred on the same margin, within the same type of sediments (glacial), along the same type of glide plane (a glacimarine layer), and were supposedly both triggered by a large earthquake (Kvalstad et al., 2005, Bellwald et al., 2019b). Consequently, we could reasonably have expected them to fail in a similar way. In the next section, we consider possible causes for the difference in failure mechanism.

4.5.2.2 Pre-conditioning and triggering factors

Bellwald et al. (2019b) used 2D Finite Element modelling and geotechnical data from the nearby Ormen Lange gas field to evaluate the effects of various pre-conditioning factors for the Tampen Slide. Their results indicated that a basal glacimarine sediment layer was critical for the generation of sediment over-pressure. However, over-pressure alone was not enough to trigger the Tampen Slide, and an earthquake of >M6.9, and proximal to the headwall, was required for failure to occur (Figure 4.11a). No evidence of gas hydrate dissociation has been found within the sediments related to the Tampen Slide (both failed and unfailed, and within the seismic data presented in this study, as well as in the work of Nygård et al., 2005, Bellwald et al., 2019b). The Storegga Slide, in comparison, is thought to have also been preconditioned by high excess pore pressure combined with earthquake loading, but its triggering earthquake seems to have occurred on the lower continental slope (Figure 4.11e; Haflidason et al., 2004, Kvalstad et al., 2005). Failure of the Storegga Slide, then, initiated on the lower continental slope and migrated upslope, incorporating multiple glide planes and escarpments (Haflidason et al., 2004). Thus, when a landslide is triggered by an earthquake, the location of that earthquake may be a key factor that influences whether a landslide develops retrogressively or along a single glide plane.

Furthermore, the location and number of glacimarine weak layers may also play an important role in controlling whether a landslide fails retrogressively or mainly during a single phase. The Tampen Slide is located within the proximal deposits of the North Sea Fan, a region with highly variable sedimentation rates. In glacial periods, the presence of ice on the shelf can result in as much as a ten-fold increase in hemipelagic sedimentation (Lekens et al., 2009), with extreme sedimentation rates exceeding 20 m/kyr on the upper slope directly affected by ice-stream sediment delivery (Hjelstuen et al., 2004). Nygård et al. (2007) found that the Norwegian Channel ice stream loaded the North Sea Fan with as much as 1.1 Gt of sediment per year during the last glacial stage. In contrast, sedimentation at the neighbouring Storegga Slide is locally controlled by contouritic currents and meltwater

plumes, and occurs at a much slower rate, averaging 1 m/kyr over the last 250 kyr (Hjelstuen et al., 2004). Weak layers, which may be prone to failure, are then more condensed within the Storegga Slide region. This may favour the development of retrogressive sliding in the Storegga region. In contrast, within the North Sea Fan, weak layers are typically separated by a thicker sedimentary unit, which would favour the development of a megaslide along a single plane as observed at the Tampen Slide.

4.5.3 Wider implications for hazards and tsunami generation

The failure mechanism and landslide geometry have major implications for the potential consequences (especially tsunami generation potential) resulting from a submarine landslide. To date, no tsunami deposits have been linked to the Tampen Slide. Although this may be due to post-depositional glacial erosion (e.g. Montelli et al., 2018) and lower sea level at that time, rather than an indication that the Tampen Slide did not result in a major tsunami. It should be noted that, whilst landslide volume is an important parameter for generating a tsunami, not all large submarine landslides result in tsunamis. For example, the retrogressive Trnadjupet Slide, also located offshore Norway, occurred ca. 4,500 years ago and involved a total volume of 500-1,000 km^3, but does not seem to have resulted in a tsunami (Laberg and Vorren, 2000, Løvholt et al., 2017). Using a coupled landslide-tsunami model, Løvholt et al. (2017) found that this was likely a result of low failure velocity (supported by observations of blocky deposits near the headwall and limited turbidity current deposits), with lesser volume and a greater distance to the coastline (compared to the Storegga Slide) also playing a role. Contrastingly, at the Tampen Slide, although a large volume of sediment remains proximal to the headwall, the interior of the slide deposits is heavily deformed (e.g. Figures 4.5 and 4.7). This, together with the large volume of the Tampen Slide's translational first phase, and the height of the main headwall ($\sim$150 m), suggests the rapid displacement of a prodigious (>720 km^3) sediment volume. The initial acceleration of the failed mass, however, cannot be reconstructed using the seismic data. This, together with the absence of tsunami deposits linked to the Tampen Slide, makes it impossible to construct a well-constrained tsunami model for the Tampen Slide. However, such a failure may generate a far larger tsunami than a multi-phase, retrogressive megaslide with the same total volume.

4.6 Conclusions

In this study, we present laterally extensive, high resolution, processed 3D seismic data from the headwall of the buried Tampen Slide offshore Norway. These data reveal the character of the slide deposits at a high level of detail, and allow us to revisit their emplacement process.

Unlike other megaslides on passive continental margins, the deposits of which are typically evacuated away from the headwall, a large volume of the Tampen Slide deposits remain close to the headwall. We suggest that this is because the Tampen deposits were laterally constrained by the Faroe-Shetland Escarpment, over which the slide deposits thin markedly. This lateral constraint significantly impacted the flow dynamics, resulting in erosion in the northern part of the surveyed area as the flow redirected northwards around the topographical high.

Within the deposits of the Tampen Slide, we identify regions of spreading, compression and translation. Within the translational deposits, there are longitudinal (downslope-elongated) chutes similar to those identified at the neighbouring Storegga Slide, which have been interpreted as regions of faster motion within the slide deposits. We also identify, for the first time, longitudinal ridges within the translational body of deep water submarine landslide deposits. Such ridges have, however, previously been suggested to be an intrinsic characteristic of landslides once they exceed certain kinematic parameters.

Apart from a few erosional features, the Tampen Slide's basal glide plane is relatively smooth. This, combined with the continuity of internal deformation across the slide deposits, indicates that the majority of the slide deposits failed as one mass, in a single phase. This differs markedly from other megaslides on passive margins, whose tiered glide planes and multiple headwalls are thought to show retrogressive failure behaviour. This variation, where a single failure, rather than several tens of failures, accounts for most of the total slide volume, may have a large impact on the tsunami generation potential of the megaslide. While the Tampen Slide is the first submarine megaslide shown to have failed in this way, other (potentially as yet undiscovered) megaslides may have failed (and may fail in the future) in a similar way. Consequently, this failure mechanism should be considered when considering the hazard potential of submarine megaslides.

Acknowledgements

Data availability: The 3D multi-client seismic data (AMS17), courtesy of TGS, is part of the Atlantic Margins multi-year program, which covered more than 50,000 km^2 between 2017 and 2019. Access to the data can be gained through purchasing a licence from TGS.

Funding: R.B. is funded by the European Union's Horizon 2020 research and innovation programme under the Marie Sklodowska-Curie Actions grant agreement No. 721403. A.M. is funded by the European Research Council (ERC) under the European Union's Horizon 2020 Programme grant agreement No. 677898. S.P. acknowledges support from the Norwegian Research Council through Centre of Excellence funding to CEED (project no. 223272).

References

Antobreh, A. A. and Krastel, S. (2007). Mauritania Slide Complex: Morphology, seismic characterisation and processes of formation. *International Journal of Earth Sciences*, 96(3):451–472.

Bellwald, B., Hjelstuen, B., Sejrup, H., Stokowy, T., and Kuvås, J. (2019a). Holocene mass movements in west and mid-Norwegian fjords and lakes. *Marine Geology*, 407:192–212.

Bellwald, B., Urlaub, M., Hjelstuen, B. O., Sejrup, H. P., Sørensen, M. B., Forsberg, C. F., and Vanneste, M. (2019b). NE Atlantic continental slope stability from a numerical modeling perspective. *Quaternary Science Reviews*, 203:248–265.

Bondevik, S., Løvholt, F., Harbitz, C. B., Mangerud, J., Dawson, A., and Svendsen, J. I. (2005). The Storegga Slide tsunami – comparing field observations with numerical simulations. In *Ormen Lange – an Integrated Study for Safe Field Development in the Storegga Submarine Area*, pages 195–208. Elsevier.

Bryn, P., Berg, K., Forsberg, C. F., Solheim, A., and Kvalstad, T. J. (2005). Explaining the Storegga Slide. *Marine and Petroleum Geology*, 22(1-2):11–19.

Bugge, T., Belderson, R. H., and Kenyon, N. H. (1988). The Storegga Slide. *Royal Society of London Philosophical Transactions*, 325(A):357–388.

Bull, S., Cartwright, J., and Huuse, M. (2009). A review of kinematic indicators from mass-transport complexes using 3D seismic data. *Marine and Petroleum Geology*, 26(7):1132–1151.

Dufresne, A. and Davies, T. (2009). Longitudinal ridges in mass movement deposits. *Geomorphology*, 105:171–181.

Evans, D., King, E., Kenyon, N., Brett, C., and Wallis, D. (1996). Evidence for long-term instability in the Storegga Slide region off western Norway. *Marine Geology*, 130(3-4):281–292.

Frey-Martínez, J., Cartwright, J., and Hall, B. (2005). 3D seismic interpretation of slump complexes: Examples from the continental margin of Israel. *Basin Research*, 17(1):83–108.

Gafeira, J., Long, D., Scrutton, R., and Evans, D. (2010). 3D seismic evidence of internal structure

within Tampen Slide deposits on the North Sea Fan: are chaotic deposits that chaotic? *Journal of the Geological Society*, 167:605–616.

Georgiopoulou, A., Masson, D. G., Wynn, R. B., and Krastel, S. (2010). Sahara slide: Age, initiation, and processes of a giant submarine slide. *Geochemistry, Geophysics, Geosystems*, 11(7).

Haflidason, H., Sejrup, H. P., Nygård, A., Mienert, J., Bryn, P., Lien, R., Forsberg, C. F., Berg, K., and Masson, D. (2004). The Storegga Slide: Architecture, geometry and slide development. *Marine Geology*, 213(1-4):201–234.

Haflidason, H., Lien, R., Sejrup, H. P., Forsberg, C. F., and Bryn, P. (2005). The dating and morphometry of the Storegga Slide. *Marine and Petroleum Geology*, 22:123–136.

Harbitz, C. B., Løvholt, F., and Bungum, H. (2014). Submarine landslide tsunamis: how extreme and how likely? *Natural Hazards*, 72:1341–1374.

Hill, J. C., Brothers, D. S., Hornbach, M. J., Sawyer, D. E., Shillington, D. J., and Bécel, A. (2019). Subsurface controls on the development of the Cape Fear Slide Complex, central US Atlantic Margin. In Lintern, G., Mosher, D., Moscardelli, L., Bobrowsky, P., Campbell, C., Chaytor, J., Clague, J., Georgiopoulou, A., Lajeunesse, P., Normandeau, A., Piper, D., Scherwath, M., Stacey, C., and Turmel, D., editors, *Submarine Mass Movements and their Consequences*, pages 169–181. Geological Society of London Special Publications, London, 477 edition.

Hjelstuen, B. and Grinde, S. (2016). 3D Seismic Investigations of Pleistocene Mass Transport Deposits and Glacigenic Debris Flows on the North Sea Fan, NE Atlantic Margin. In Lamarche, G., Mountjoy, J., Bull, S., Hubble, T., Krastel, S., Lane, E., Micallef, A., Moscardelli, L., Mueller, C., Pecher, I., and Woelz, S., editors, *Submarine Mass Movements and their Consequences, Advances in Natural and Technological Hazards Research*, pages 265–272. Springer, Cham, Switzerland, 41 edition.

Hjelstuen, B. O., Sejrup, H. P., Haflidason, H., Nygård, A., Berstad, I. M., and Knorr, G. (2004). Late Quaternary seismic stratigraphy and geological development of the south Vøring margin, Norwegian Sea. *Quaternary Science Reviews*, 23(16-17):1847–1865.

King, E. L., Sejrup, H. P., Haflidason, H., Elverhøi, A., and Aarseth, I. (1996). Quaternary seismic stratigraphy of the North Sea Fan: glacially-fed gravity flow aprons, hemipelagic sediments, and large submarine slides. *Marine Geology*, 130(3-4):293–315.

Kiørboe, L. (1999). Stratigraphic relationships of the Lower Tertiary of the Faeroe Basalt Plateau and the FaeroeShetland Basin. In *Petroleum Geology Conference series*, pages 559–571. Geological Society, London.

Korup, O., Clague, J. J., Hermanns, R. L., Hewitt, K., Strom, A., and Weidinger, J. (2007). Giant landslides, topography, and erosion. *Earth and Planetary Science Letters*, 261(3-4):578–589.

Kvalstad, T. J., Andresen, L., Forsberg, C. F., Berg, K., Bryn, P., and Wangen, M. (2005). The Storegga slide: Evaluation of triggering sources and slide mechanics. *Marine and Petroleum Geology*, 22(1-2):245–256.

Laberg, J. S. and Vorren, T. O. (2000). The Trænadjupet Slide, offshore Norway - Morphology, evacuation and triggering mechanisms. *Marine Geology*, 171(1-4):95–114.

Lastras, G., Canals, M., and Urgeles, R. (2003). Lessons from sea-floor and subsea-floor imagery of

the BIG'95 debris flow scar and deposit. In Locat, J. and Mienert, J., editors, *Submarine Mass Movements and Their Consequences*, pages 425–431. Kluwer Acad., Dordrecht, Netherlands.

Lekens, W. A. H., Haflidason, H., Sejrup, H. P., Nygard, A., Richter, T., Vogt, C., and Frederichs, T. (2009). Sedimentation history of the northern North Sea Margin during the last 150 ka. *Quaternary Science Reviews*, 28(5-6):469–483.

Li, W., Alves, T. M., Urlaub, M., Georgiopoulou, A., Klaucke, I., Wynn, R. B., Gross, F., Meyer, M., Repschläger, J., Berndt, C., and Krastel, S. (2017). Morphology, age and sediment dynamics of the upper headwall of the Sahara Slide Complex, Northwest Africa: Evidence for a large Late Holocene failure. *Marine Geology*, 393:109–123.

Lintern, D., Mosher, D. C., Moscardelli, L., and al., E. (2018). *Subaqueous Mass Movements*. Geological Society of London Special Publications, London, 477 edition.

Løvholt, F., Bondevik, S., Laberg, J. S., Kim, J., and Boylan, N. (2017). Some giant submarine landslides do not produce large tsunamis. *Geophysical Research Letters*, 44(16):8463–8472.

Magnarini, G., Mitchell, T. M., Grindrod, P. M., and Schmitt, H. H. (2019). Granular Flow Mechanisms in Martian Landslides. *Nature Communications*, pages 1–7.

Masson, D. G., Hugget, Q., and Brunsden, D. (1993). The surface texture of the Saharan debris flow deposit and some speculation on submarine debris flow processes. *Sedimentology*, 40:583–598.

Masson, D. G., Wynn, R. B., and Talling, P. J. (2010). Large Landslides on Passive Continental Margins: Processes, Hypotheses and Outstanding Questions. In Mosher, D. C., Moscardelli, L., Shipp, R., Chaytor, J., Baxter, C., Lee, H., and Urgeles, R., editors, *Submarine Mass Movements and Their Consequences: Advances in Natural and Technological Hazards Research*, volume 28, pages 153–165. Springer, Dordrecht, Netherlands.

Micallef, A., Masson, D. G., Berndt, C., and Stow, D. A. (2007). Morphology and mechanics of submarine spreading: A case study from the Storegga Slide. *Journal of Geophysical Research: Earth Surface*, 112(3):1–21.

Micallef, A., Berndt, C., Masson, D. G., and Stow, D. A. (2008). Scale invariant characteristics of the Storegga Slide and implications for large-scale submarine mass movements. *Marine Geology*, 247(1-2):46–60.

Micallef, A., Masson, D. G., Berndt, C., and Stow, D. A. (2009). Development and mass movement processes of the north-eastern Storegga Slide. *Quaternary Science Reviews*, 28(5-6):433–448.

Montelli, A., Dowdeswell, J. A., Ottesen, D., and Johansen, S. (2018). 3D seismic evidence of buried iceberg ploughmarks from the mid-Norwegian continental margin reveals largely persistent North Atlantic Current through the Quaternary. *Marine Geology*, 399:66–83.

Nygård, A., Sejrup, H. P., Haflidason, H., and Bryn, P. (2005). The glacial North Sea Fan, southern Norwegian Margin: Architecture and evolution from the upper continental slope to the deep-sea basin. *Marine and Petroleum Geology*, 22(1-2):71–84.

Nygård, A., Sejrup, H. P., Haflidason, H., Lekens, W. A. H., Clark, C. D., and Bigg, G. R. (2007). Extreme sediment and ice discharge from marine-based ice streams: New evidence from the North Sea. *Geology*, 35(5):395–398.

Omosanya, K. O. and Alves, T. M. (2013). Ramps and flats of mass-transport deposits (MTDs)

as markers of seafloor strain on the flanks of rising diapirs (Espirito Santo Basin, SE Brasil). *Marine Geology*, 340:82–97.

Pope, E. L., Talling, P. J., and O Cofaigh, C. (2018). The relationship between ice sheets and submarine mass movements in the Nordic Seas during the Quaternary. *Earth science reviews*, 178:208–256.

Pouliquen, O., Delour, J., and Savage, S. (1997). Fingering in granular flows. *Nature*, 386(6627):816–817.

Prior, D. B., Wiseman, W., and Bryant, W. R. (1981). Submarine chutes on the slopes of fjord deltas. *Nature*, 290:326–328.

Smith, W. H. and Wessel, P. (1990). Gridding with continuous curvature splines in tension. *Geophysics*, 55:293–305.

Strachan, L. (2002). *From geometry to genesis: a comparative field study of slump deposits and their modes of formation*. PhD thesis, University of Cardiff.

Trincardi, F. and Argnani, A. (1990). Gela submarine slide: A major basin-wide event in the plio-quaternary foredeep of Sicily. *Geo-Marine Letters*, 10(1):13–21.

Valderrama, P., Roche, O., Samaniego, P., van Wyk des Fries, B., and Araujo, G. (2017). Granular fingering as a mechanism for ridge formation in debris avalanche deposits: Laboratory experiments and implications for Tutupaca volcano, Peru. *Journal of Volcanology and Geothermal Research*, 349:409–418.

Vanneste, M., Mienert, J., and Bünz, S. (2006). The Hinlopen Slide: A giant, submarine slope failure on the northern Svalbard margin, Arctic Ocean. *Earth and Planetary Science Letters*, 245(1-2):373–388.

Watts, M., Talling, P., Hunt, J., Xuan, C., and van Peer, T. (2016). A new date for a large pre-Holocene Storegga Slide. In *EGU General Assembly*, Vienna, Austria.

Whiteside, W., Wang, B., Bondeson, H., and Li, Z. (2013). 3D imaging from 2D seismic data, an enhanced methodology. *SEG Technical Program Expanded Abstracts*.

Zastrozhnov, D., Gernigon, L., Gogin, I., Planke, S., Abdelmalak, M. M., Polteau, S., Faleide, J. I., Manton, B., and Myklebust, R. (2020). Regional structure and polyphased Cretaceous-Paleocene rift and basin development of the mid-Norwegian volcanic passive margin. *Marine and Petroleum Geology*, 115.

Chapter 5

Quantitative morphometric analysis of ridges in subaqueous landslides

Can we use spectral analysis and principal component analysis to distinguish between extensional and compressional ridges in subaqueous landslide deposits?

Manuscript III

Rachel Barrett, Philipp Held, Aaron Micallef, Felix Gross,
Christian Berndt, and Sebastian Krastel

Draft in preparation for

Journal of Geophysical Research: Earth Surface

Abstract

Morphometric features within subaqueous landslide deposits provide critical information about the process of failure – a factor that is directly linked to the hazard potential of a landslide. However, some morphometric features, such as compressional and extensional (spreading) ridges, have similar geomorphology even though they form through very different processes. This can make it difficult to distinguish between these features, especially in areas of low data coverage, or for very large landslides that may have formed in multiple phases. Here, we use a combined spectral and principal component analysis (PCA) workflow to quantitatively distinguish between spreading, toe-compression, and lateral-margin compressional ridges in subaqueous landslide deposits. Using bathmetric and 3D seismic horizon data from the mid-Norwegian continental margin, the Malta Escarpment, and two peri-alpine lakes in Switzerland, we find a clear separation between all three types of ridges in principal component space. We also test this approach on down-sampled data, and find that the quality of this analysis depends strongly upon the resolution of the data. Our results highlight a link between the morphological signature of the ridges and their formative process that can be identified using a statistical approach with minimal interpreter input. The application of quantitative, semi-automatic methodology such as this is critical in order to move towards a less subjective interpretation of subaqueous landslide deposits.

5.1 Introduction

Subaqueous landslides are globally widespread – having been documented along both passive and active margins, at volcanic islands, and in lakes – and can have devastating consequences, including the generation of tsunami waves; damage to subaqueous infrastructure such as internet cables, oil rigs, and wind farms; damage to coastal infrastructure; and significant loss of life (e.g. Heezen and Ewing, 1952, Talling et al., 2014, Carter et al., 2014, Clare et al., 2017). Furthermore, these subaqueous landslides can be orders of magnitude larger than their terrestrial counterparts (Hampton et al., 1996, Masson et al., 2010). However, their submerged nature and frequent burial beneath subsequently deposited sediment complicates their analysis, and their geometry and lateral extent are often poorly constrained (e.g. Mountjoy and Micallef, 2018). Furthermore, there are few direct observations of subaqueous landslides in real time. Consequently, the best way to increase our understanding of the process of failure, and the associated hazard(s), is by studying the deposits of past subaqueous landslides, and using their morphology to constrain and reconstruct their failure mechanism.

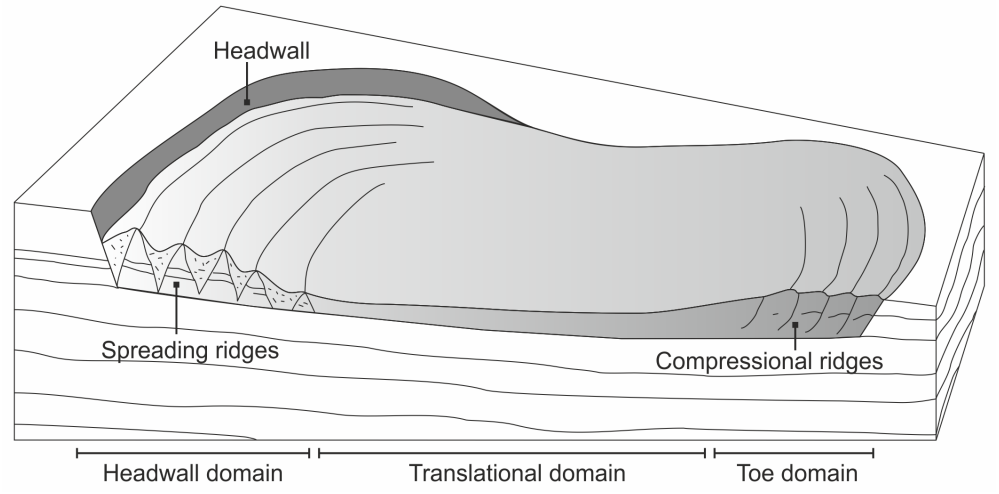

Figure 5.1: Cartoon representing the geometry of a 'typical' (simplified) subaqueous landslide. The headwall domain is dominated by extension while the toe domain is largely compressional (after Bull et al., 2009).

Landslide deposits can typically be divided into three domains - the extensional headwall region; the translational body; and the compressional toe (Figure 5.1) - each of which is characterized by different morphological features, or *kinematic indicators* (Prior et al., 1984, Bull et al., 2009, Mountjoy and Micallef, 2018). The orientation and distribution of these features plays a critical role in reconstructing the failure mechanism of a subaqueous landslide, and an accurate impact assessment depends on correctly interpreting the morphology. Within the headwall domain, the two key kinematic indicators are the headwall scarp, and extensional ridges and blocks (Figure 5.1; Bull et al., 2009). These extensional ridges (also referred to as *spreading*) are aligned perpendicular to the direction of failure (i.e. parallel to the headwall scarp), and are characterized by a repetitive 'ridge and trough' morphology (Micallef et al., 2007c). Spreading ridges are thought to result from seismic loading and loss of basal support, so that they typically occur following the formation of a headwall and the excavation of the failed mass (Lastras et al., 2003, Micallef et al., 2007c). A similarly repetitive series of ridges and troughs is also often present within the compressional toe domain of a frontally-confined subaqueous landslide (Figure 5.1; Schnellmann et al., 2005, Frey-Martínez et al., 2006). While these compressional ridges are also aligned perpendicular to the direction of motion, they are the surface expression of folding and thrusting within the landslide toe (Schnellmann et al., 2005). Compressional ridges can also be found along the lateral margins of the slide (with compression occurring along- rather than downslope), such as at the Storegga Slide, offshore Norway – arguably the best studied subaqueous landslide globally (e.g. Haflidason et al., 2004, Micallef et al., 2007a, Bull and Cartwright, 2020).

Although spreading and compressional ridges form through contrasting processes, their ge-

omorphological signatures are often similar in bathymetric data. This means that they can be difficult to distinguish where the data resolution is low or the available data does not cover the full extent of the landslide deposits. This is particularly a problem for large volume landslides, which cover an extensive area, and whose failure often involves multiple phases that can be difficult to distinguish from one another due to the scale of sliding (e.g. Antobreh and Krastel, 2007, Micallef et al., 2009, Li et al., 2017), as well as for buried subaqueous landslides (e.g. Barrett et al., in review).

The recurrent, repetitive nature of the ridges is a key feature of the ridge and trough topography. Spreading ridges tend to both become more widely spaced and decrease in height with distance from the headwall scarp (Micallef et al., 2007c). Contrastingly, the height of compressional ridges seems to vary less (e.g. Schnellmann et al., 2005, Bull et al., 2009, Barrett et al., in review). Hence, we hypothesize that height variation (and possibly spacing) between ridges may be a distinguishing factor between spreading and compressional ridges. Morphological characterization of subaqueous landslides is often performed in a more qualitative manner (e.g. Bull et al., 2009, Gafeira et al., 2010, Clare et al., 2018) but, while qualitative analysis is a powerful tool for constraining a landslide's motion, the results often depend heavily on the experience of the interpreter. However, quantitative approaches, which are less prone to subjectivity, have become more commonplace over the last couple of decades (e.g. Micallef et al., 2007a,b, Moscardelli and Wood, 2016).

Spectral analysis is a way of characterizing the wavelength and variation of the seafloor using the frequency domain, and has previously been used to characterise seafloor roughness; e.g. to study ripples (Lefebvre et al., 2011), and for habitat mapping (Schönke et al., 2017). A rough, uneven surface without any clear bedforms is generally associated with a diffuse frequency spectrum, with multiple low energy peaks. The frequency spectrum of a surface that contains repetitive, elongated bedforms such as ridges, however, is typified by a strong, high energy peak that corresponds with the wavelength of the ridges, as well as a directionality that strikes perpendicular to the bedform orientation (Lefebvre et al., 2011).

The overarching aim of this study is to characterize the spectral signature of spreading and compressional ridges in subaqueous landslide deposits in a variety of settings (both submarine and lacustrine). Specifically, we want to answer the question of whether the spectral characteristics of spreading and compressional ridges are distinct enough that they can be quantitatively distinguished from one another in areas of low data coverage or where the internal seismic character of the ridges is unclear. We begin by characterizing the bathymetric and spectral signature of spreading and compressional ridges in landslide deposits offshore Norway, on the Malta Escarpment, and in two Swiss lakes (Figure 5.2). We then use Principal Component Analysis to reduce the number of parameters and attempt to quantitatively

(and semi-automatically) distinguish between compressional and spreading ridges. We also down-sample the data from two regions which contain both spreading and compressional ridges, and consider the implications of data resolution before discussing our findings.

5.2 Geological Settings and Data

5.2.1 The Norwegian mid-continental margin

Sedimentation along the Norwegian mid-continental margin is dominated by glacial and interglacial processes, and the stratigraphy correspondingly consists of glacigenic debris flows, hemipelagic/glacimarine deposits, and megaslide deposits (King et al., 1996, Hjelstuen et al., 2004, Nygård et al., 2005). Here, we make use of data from the headwall area of two of those megaslides: the Holocene Storegga Slide, which involved a total volume of 2,400 - 3,200 km^3 and is exposed at the seafloor (Figure 5.2b, Haflidason et al., 2005, Kvalstad et al., 2005); and the older Tampen Slide, which involved >1,000 km^3 and is buried within the deposits of the North Sea Fan (Figure 5.2c, Nygård et al., 2005). Compressional and extensional ridges have previously been documented in the deposits of both of these megaslides (Sejrup et al., 2004, Micallef et al., 2007c, Hjelstuen and Grinde, 2016, Barrett et al., in review).

The giant Storegga Slide is one of the most well-known subaqueous landslides and has been widely studied over the last thirty years (e.g. Bugge et al., 1988, Solheim et al., 2005, Micallef et al., 2007a, Bull et al., 2009, Bull and Cartwright, 2020). Several regions of extensive spreading have been previously documented within the headwall area of this megaslide (Micallef et al., 2007c, 2016b), and compressional ridges are present along the western lateral margin of the headwall (Sejrup et al., 2004, Haflidason et al., 2004). These ridges are spaced between 600 - 2,000 m apart, and cover an extensive area (Table 5.1). Here, we make use of high-quality (25x25m grid cell size) bathymetric data previously published by Micallef et al. (2007a, Figure 5.2b).

The Tampen Slide is buried by up to 450 m of glacigenic debris flows, contourites, and glacimarine sediments (Barrett et al., in review), so we use high-resolution 3D seismic data (courtesy of TGS) to study extensional and compressional ridges within its deposits. Barrett et al. (in review) used this dataset to analyse the upper and lower surfaces of the Tampen Slide, as well as its interior, and constrain its morphology and emplacement mechanism. Here, we consider just the upper surface of the slide deposits, and treat it as a DEM gridded at 20 m resolution (Figure 5.2c). Similarly to those within the Storegga Slide, ridges within the Tampen Slide deposits are widely spaced and cover a large area (Table 5.1).

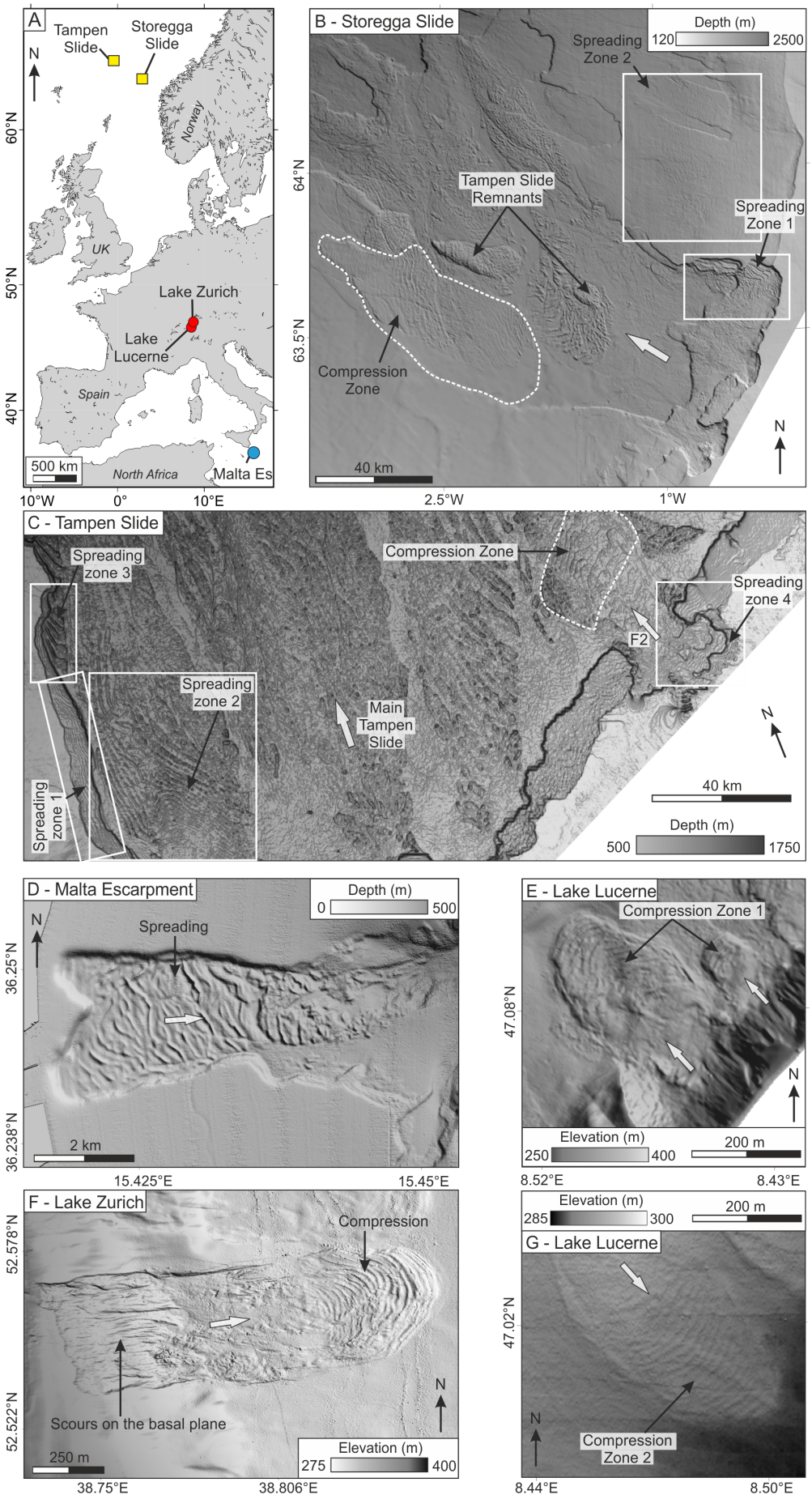
A
Tampen Slide
Storegga Slide
N
Norway
UK
Lake Zurich
Lake Lucerne
Spain
North Africa
Malta Es
500 km
60°N
50°N
40°N
10°W
0°
10°E
B - Storegga Slide
Depth (m)
120
2500
Spreading Zone 2
Tampen Slide Remnants
Spreading Zone 1
Compression Zone
40 km
64°N
63.5°N
2.5°W
1°W
C - Tampen Slide
Spreading zone 3
Compression Zone
Spreading zone 4
F2
Spreading zone 2
Main Tampen Slide
Spreading zone 1
40 km
Depth (m)
500
1750
D - Malta Escarpment
Depth (m)
0
500
Spreading
2 km
36.25°N
36.238°N
15.425°E
15.45°E
E - Lake Lucerne
Compression Zone 1
Elevation (m)
250
400
200 m
47.08°N
8.52°E
8.43°E
F - Lake Zurich
Compression
Scours on the basal plane
250 m
Elevation (m)
275
400
52.578°N
52.522°N
38.75°E
38.806°E
Elevation (m)
285
300
200 m
G - Lake Lucerne
Compression Zone 2
47.02°N
8.44°E
8.50°E

Figure 5.2 *(previous page)*: (a) Overview of DEM data used in this study. Blue circle: case study involving spreading; red circle: case study involving compression; yellow square: case study involving both spreading and compressional regions. Sun-illuminated DEMs from (b) the Storegga Slide headwall (Micallef et al., 2007a); (c) the Tampen Slide headwall (Barrett et al., in review; data courtesy of TGS); (d) the Malta Escarpment (Micallef et al., 2016a); (e) Lake Lucerne (Hilbe et al., 2011); (f) Lake Zurich (Strupler et al., 2017); and (g) Lake Lucerne (Hilbe et al., 2011). White arrows: direction of landslide motion. F2: Secondary failure of the Tampen Slide headwall.

5.2.2 The Malta Escarpment

The Malta Escarpment is a carbonate escarpment that is marked by steep slopes (>70°) and limestone and dolomite cliffs (Scandone et al., 1981, Micallef et al., 2019). The morphology of its outer continental shelf is dominated by escarpment-forming processes including mass movements, strike-slip faulting, and the flow of bottom currents both perpendicular and parallel to the escarpment (Micallef et al., 2016a). Furthermore, sedimentation along the escarpment is primarily dominated by pelagic and hemipelagic processes, but is locally influenced by bottom current activity (Micallef et al., 2016a). Here, we make use of multibeam data collected during the CUMECS (2012) and CUMECS-2 (2014) research cruises, which reveal spreading ridges on the continental shelf upslope of the Malta Escarpment (Figure 5.2d; Micallef et al., 2016a). This data is gridded at 10x10 m grid cell spacing.

5.2.3 Swiss lakes

Lake Lucerne and Lake Zurich are glacially-formed, peri-alpine lakes in Switzerland. Alpine lakes are dynamic environments, and a variety of mass transport deposits have been documented in these two lakes, including some linked to rockfall (Schnellmann et al., 2006, Hilbe et al., 2011, Sammartini et al., 2019) and delta collapse (Hilbe and Anselmetti, 2014, Sammartini et al., 2019), as well as lateral slope landslides within hemipelagic sediment units (Kelts and Hsü, 1980, Schnellmann et al., 2002, Strasser and Anselmetti, 2008, Strupler et al., 2017). Here, we use multibeam bathymetric data published by Hilbe et al. (2011, Lake Lucerne) and Strupler et al. (2017, Lake Zurich), which include clear compressional ridges at the toes of several frontally-confined landslide deposits (Figure 5.2e-g). The Lake Lucerne data is gridded at 2x2 m resolution, and the Lake Zurich data has a grid cell size of 1x1m.

Table 5.1: Parameters used for the manual selection of window size for spectral analysis for the different regions of compression and extension within the regions presented in this study. The location of the different zones within each landslide are shown in Figure 5.2.

Region	**Zone**	**Lateral data resolution (m)**		**Area covered by ridges (km^2)**	**Ridge spacing (m)**	**Spectral analysis window length (pixels)**	
		Full-resolution datset	Down-sampled dataset			Full-resolution datset	Down-sampled dataset
				Extensional ridges (spreading)			
Tampen Slide	1	20	100	148	400-800	100	20
	2	20	100	390	600-800	150	24
	3	20	100	155	1300	160	40
	4	20	100	70	400-500	75	15
Storegga Slide	1	25	200	350	2,000	250	35
	2	25	200	4760	600-800	120	25
Malta Escarpment	1	10	10	10.3	200-300	70	70
				Compressional ridges			
Tampen Slide	1	20	100	148	800-1,000	34	120
Storegga Slide	1	25	200	2012	600-1,000	15	150
Lake Lucerne	1	2	2	0.034	12-18	22	22
	2	2	2	0.053	12-20	25	25
Lake Zurich	1	1	1	0.095	11-19	50	50

5.3 Methodology

5.3.1 Fourier Analysis

The region of interest for each dataset was divided into a grid of square cells with a window length large enough to include a series of three to four ridges (Table 5.1). Linear trends were removed from each window by subtracting the mean of the elevation (in x and y directions) from the bathymetric data, before the data were normalized by subtracting the mean elevation within the window from each cell (Figure 5.3a). The 2D Fast Fourier Transform (FFT) for each window was then calculated using the standard implementation of the 2D FFT in the Python library *numpy* (Cooley and Tukey, 1965):

$$A_{kl} = \sum_{m=0}^{M-1} \sum_{n=0}^{N-1} a_{mn} exp\left\{-2\pi i \left(\frac{mk}{M} + \frac{nl}{N}\right)\right\} \tag{5.1}$$

where A_{kl} is the complex output frequency spectrum, a_{mn} is the input bathymetry signal, and k and l range between 0 and M-1/N-1, respectively.

Primary frequencies within the spectrum (long wavelengths) can have high amplitudes that often dwarf the frequencies of interest. For this reason, we suppressed frequencies within the bands f0, f1 and f2, and set them equal to the mean of the 2D FFT spectrum within that window. The logarithmic form (power spectrum) of the 2D FFT spectrum (Figure 5.3b) was calculated using the standard power law

$$PS = 10 \log_{10}(|FFT|^2) \tag{5.2}$$

Both the result of the FFT and its corresponding power spectrum are symmetrical about 0, so only half the spectrum (0-180°) is used for further analysis. The 2D power spectrum was converted to a 1D spectrum by taking the mean of radial 1° slices through the 2D spectrum (Figure 5.3c).

5.3.2 Extraction of statistical parameters from the bathymetry and spectral analysis results

We then computed widely-used statistical parameters (variance, skewness, and kurtosis) of both the 1D power spectrum and the bathymetric data for each window in order to quantitatively compare the spreading and compressional ridges from different regions. These were calculated using standard Python *numpy* and *scipy* libraries.

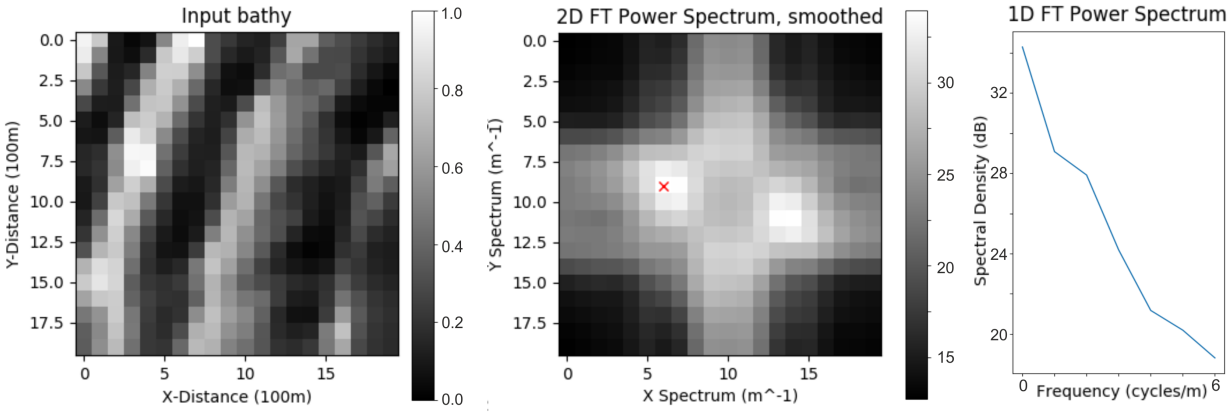

Figure 5.3: Example from spreading ridges along the western sidewall of the Tampen Slide, offshore Norway, using the down-sampled dataset. (a) Hillshaded bathymetry within an analysis window. (b) Smoothed 2D Power Spectrum. The peak of the spectrum is marked by the red cross. (c) 1D Power Spectrum.

Variance (S^2), the spread of numbers from their mean, is defined by

$$S^2 = \frac{\sum(x_i - \bar{x})^2}{n-1} \tag{5.3}$$

where x_i is the value of one observation, $\bar{x}$ is the mean of all observations, and n is the number of observations.

Skewness (a), a measure of the symmetry of the dataset (where a perfectly symmetrical dataset has a skewness of 0) is defined by

$$a = \sum \frac{(x_i - \bar{x})^3}{ns^3} \tag{5.4}$$

where x_i, $\bar{x}$, and n are as defined above, and s is the standard deviation.

Kurtosis (k), a measure of the combined weight of the tails relative to the rest of the distribution, is given by

$$k = \sum \frac{(x_i - \bar{x})^4}{ns^4} \tag{5.5}$$

where the variables are all as defined previously.

An additional way to analyse the periodicity of the frequency spectrum is to compute its *cepstrum quefrencies*. The cepstrum is calculated by taking the logarithm of the magnitude of the Fourier spectrum, and then performing the inverse Fourier transform, with the resulting values – the inverse of frequency – referred to as *quefrencies* (Bogert, 1963). This is essentially deconvolution of the frequency spectrum. We extracted and plotted the first four cepstrum quefrencies for each analysis window, again using standard *numpy* functions.

Terrain Ruggedness Index – the mean elevation difference between a cell and its neighbouring cells can be calculated using the equation

$$TRI = \left(\frac{\sum (x_{ij} - x_{00})^2}{8} \right)^{1/2} \tag{5.6}$$

where x_{ij} is the elevation of each of the cells neighbouring x_{00} (Riley et al., 1999). This technique has been found to be a useful way of differentiating between morphological features based on their surface roughness (e.g. Riley et al., 1999, Wilson et al., 2007, Lecours et al., 2017). We compute the ruggedness of cells within each analysis window.

Finally, we smoothed the 2D power spectrum by applying a Gaussian filter to the spectrum, and then extracted the peak of each 2D power spectrum and computed its strength by dividing the value of the peak by the sum of half of the smoothed spectrum (because the spectrum is symmetrical about 0). In total, we extracted twelve statistical parameters for each analysis window (e.g. Figure 5.4). Plots of these parameters for all the regions of spreading and compression analysed within the study areas are included in the Appendix.

However, when considered in isolation, the statistical parameters that we extract from the bathymetric and frequency spectrum data are difficult to interpret visually. While significant changes in morphology (such as the headwall scarp shown in Figure 5.4) are evident in several of the parameter plots (e.g. Bathymetric and 1d PSD variance, as well as Cepstrum q0 and Terrain Ruggedness Index, for the example case), the cells containing ridges cannot be manually differentiated. The best way to analyse and compare the data in order to differentiate between the different types of ridges is to reduce the number of parameters that are involved and visualize them in a single plot. We do this using Principal Component Analysis (PCA). PCA is a statistical technique that aims to reduce the number of dimensions of a dataset while maintaining its variability (Jolliffe and Cadima, 2016). The resulting variables (principal components) are eigenvectors and their eigenvalues are linearly related to the original data. Here, using PCA enables us to reduce the number of variables from twelve to three, which makes it easier to distinguish the morphology of different types of ridges from one another. Before performing PCA, we manually classified grid cells according to whether they contained spreading, lateral-margin or toe-compressional ridges, or background values using the linearly detrended bathymetry and hillshaded bathymetry data, and then ignored the background values for PCA (e.g. Figure 5.4).

In order to test the effect of data resolution on our analysis, we also performed PCA for a second database that includes down-sampled DEM data from the Storegga and Tampen Slides – the two landslides presented here that include both spreading and compressional ridges (although the type of compressional ridge differs between the two slides). For that

database, we used grid-cell sizes of 200x200 m and 100x100 m for the Storegga and Tampen Slides, respectively (Table 5.1). We refer to that dataset hereafter as 'low resolution', although the resolution of the data from the Malta Escarpment, Lake Lucerne, and Lake Zurich are not altered.

5.4 Results

The first three principal components of the analysis of the high-resolution dataset (Figure 5.6) account for ∼75% of the total variance (PC1: 42.7%; PC2: 19.9%; PC3: 12.5%). Similarly, the first three principal components of the database that includes the down-sampled data (Figure 5.5) also account for ∼75% of the total variance (PC1: 40.4%; PC2: 22.2%; PC3: 12.2%). For both the high- and low-resolution datasets, spreading ridges from the Storegga Slide, Tampen Slide, and the Malta Escarpment plot within the central region of the principal component space, while lateral-margin compressional ridges from the Storegga Slide, and toe-compressional ridges (from Lake Lucerne and Lake Zurich) plot on opposite sides of the spreading ridge points. Furthermore, the toe-compressional ridges from the mass transport deposits in Lake Lucerne and Lake Zurich plot in two separate clusters

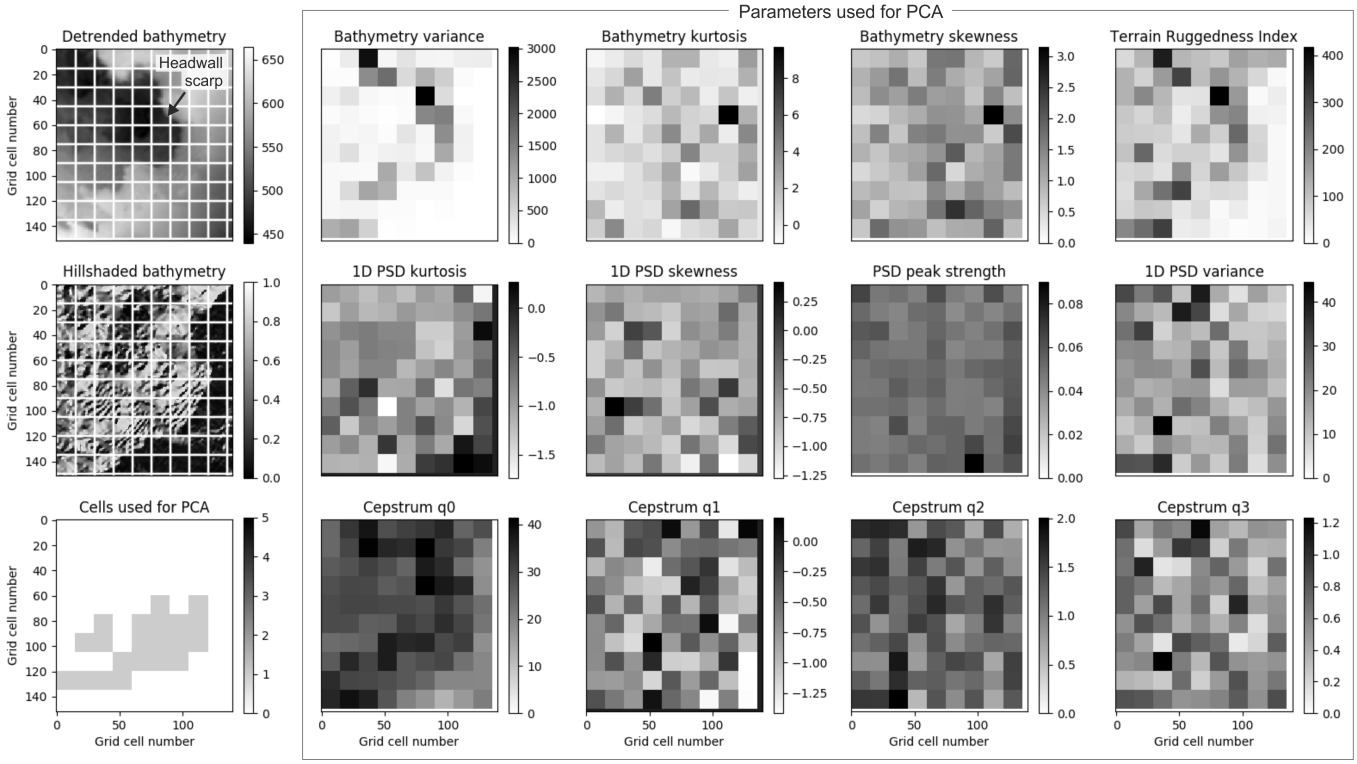

Figure 5.4: Statistical parameters extracted from the low-resolution version of the bathymetry and fourier analysis power spectrum of spreading ridges at the headwall of the Tampen Slide (Zone 4).

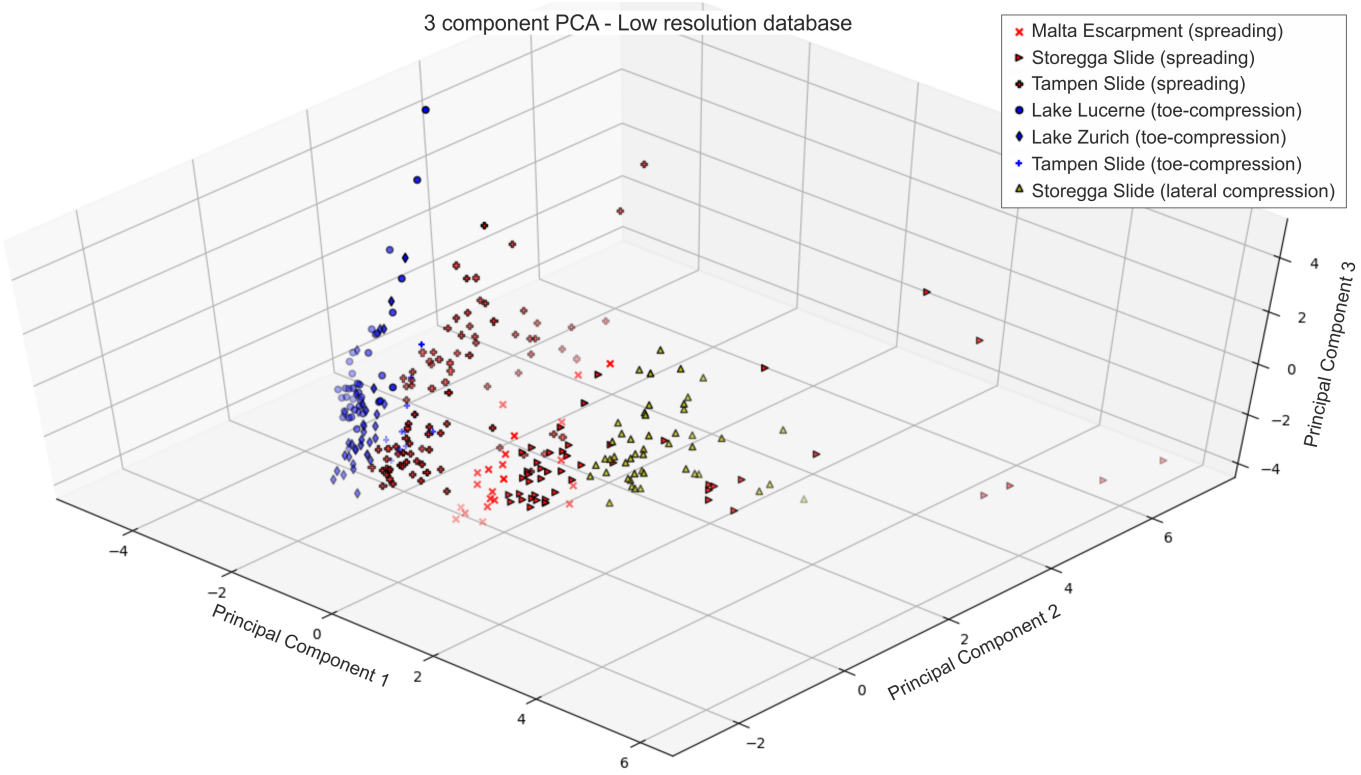

Figure 5.5: The results of Principal Component Analysis performed on the database that includes down-sampled DEMs from the Tampen and Storegga Slides.

in both the low- and high-resolution dataset PCA plots. There are, however, two significant variations in the PCA output for the two datasets. Firstly, the points related to toe-compression within the Tampen Slide plot along the boundary between spreading and toe-compressional ridges for the low-resolution PCA output, but plot fully within the principal component space of the spreading ridges in the high-resolution PCA output. Secondly, the lateral-margin compressional ridges, which also plot on the boundary of the spreading ridges in the low-resolution PCA output, plot within a distinct cluster that is separate from the spreading ridges in the high-resolution PCA plot.

5.5 Discussion

5.5.1 Varying data resolution

While lateral-margin and toe-compressional ridges can be separated from the spreading ridges in PCA of the low-resolution version of the database (Figure 5.5), this distinction and their clustering is much clearer in the PCA results of the high-resolution database (Figure 5.6). This indicates that the smoothing and simplification of morphological features through

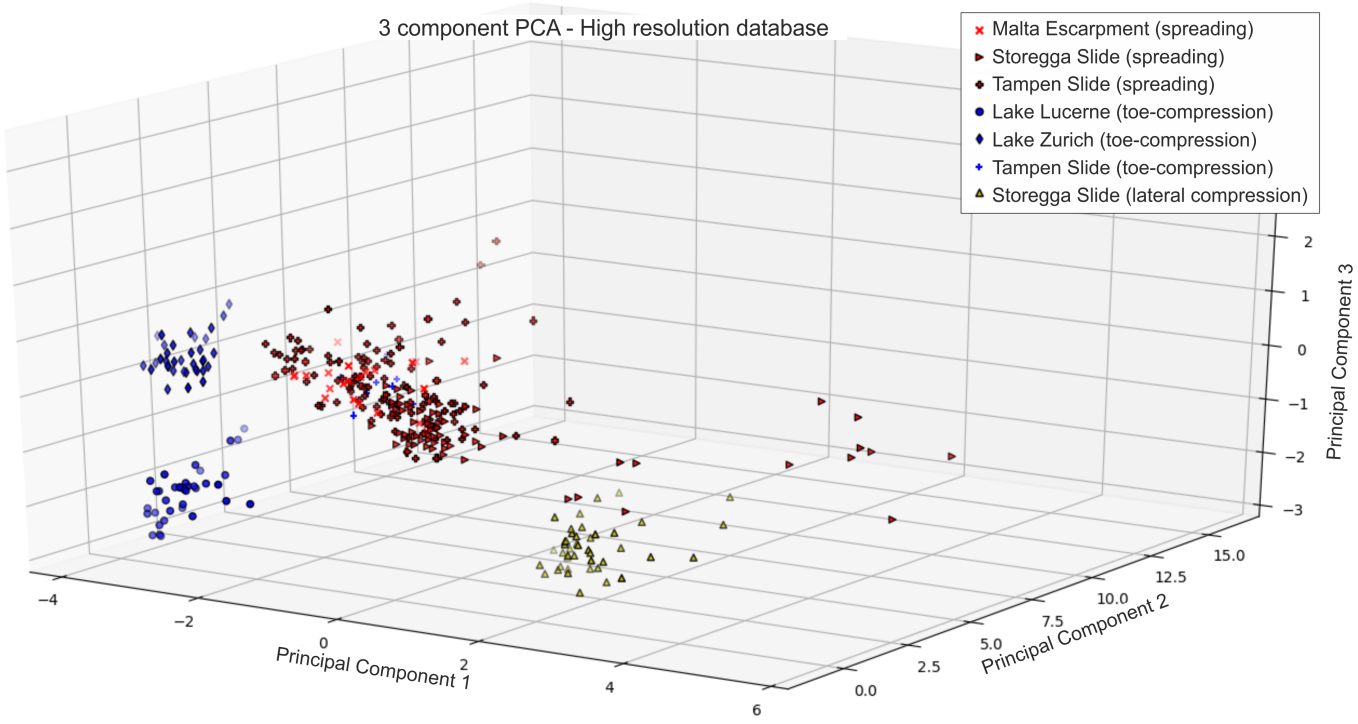

Figure 5.6: The results of Principal Component Analysis performed on the database that includes high-resolution DEMs from the Tampen and Storegga Slides.

application of a coarse grid-spacing results in the loss of key morphological information, even for features that have a much longer wavelength than the grid spacing (Table 5.1).

Furthermore, while clearly distinguished from spreading and lateral-margin compression, it is evident that the toe-compressional ridges from the mass transport deposits in Lake Lucerne and Lake Zurich plot in two distinct clusters (Figure 5.6). The type of mass transport deposit, as well as resolution of these data (1x1 m compared to 2x2 m grid cell spacing), are similar. Consequently, we suggest that the clustering of the toe-compressional ridges from these two lakes is either reflective of the slightly different settings, or of differing signal to noise ratios of the data. Nonetheless, these two clusters are clearly distinct from both spreading and lateral-margin compression in principal component space.

5.5.2 Distinguishing ridges from one another

Spreading ridges from the Malta Escarpment, Tampen Slide, and Storegga Slide plot within a central cluster in principal component space (Figure 5.6), and are clearly distinguished from lateral-margin compressional ridges and the toe-compressional ridges of the mass transport deposits within Lake Lucerne and Lake Zurich. The points related to toe-compressional ridges within the Tampen Slide, however, plot within the principal component space of

the spreading ridges. This indicates that their morphology is so similar that they cannot be distinguished using spectral analysis and PCA. Barrett et al. (in review) analysed the same high-resolution 3D dataset covering the Tampen Slide headwall area as we use, and found that the toe-compressional ridges examined here are part of a subsequent retrogressive debris flow from the main Tampen Slide headwall (Figure 5.2). Unlike other megaslides, the failed mass of which normally evacuates out of the headwall region (e.g. Korup et al., 2007, Masson et al., 2010), a large volume of the Tampen Slide deposits remain within the confines of the headwall (Barrett et al., in review). This means that the toe-compressional ridges within the Tampen Slide, which are orientated obliquely to the failure direction of the main Tampen Slide, likely over-print pre-existing morphological fabric. Furthermore, the Tampen Slide is buried beneath up to 450 m of sediment (Barrett et al., in review). This may have resulted in the flattening of the slide morphology, so that the morphology of the toe-compressional ridges no longer reflects their process of formation.

If we disregard the toe-compressional ridges of the Tampen Slide, which we consider reasonable given the above arguments, our results show a clear distinction between spreading ridges, toe-compression, and lateral-margin compression, highlighting a link between process and morphology. This suggests that a semi-automated method such as this may be able to be adapted to perform the inverse solution – and identify the process responsible for the formation of ridges based on their morphology. This would be an important step in reducing the subjectivity often inherent in the study of landslides. We are, however, aware that our study only includes a small number of examples from very different settings, and additional data are required in order to further validate this approach. This is complicated by the role that data resolution plays in the output of this analysis, as such high-resolution data are often not available.

5.6 Conclusions and Outlook

In this study, we sought to answer the question of whether compressional and spreading ridges in mass transport deposits can be quantitatively, and (semi-)automatically distinguished using spectral analysis and bathymetric statistics. For this purpose, we made use of previously published, gridded DEMs covering mass transport deposits in Lakes Zurich and Lucerne in Switzerland, the Malta Escarpment offshore Sicily, and the Storegga and Tampen megaslides on the mid-Norwegian continental margin. We analysed the spectral and bathymetric statistics of the ridges within these datasets, and used Principal Component Analysis to compare these regions. We find that the toe-compressional ridges from Lake Lucerne and Lake Zurich are clearly distinguished from both spreading ridges and

lateral-margin compressional ridges – both of which also plot distinctly from one another in principal component space. Toe-compressional ridges of the Tampen Slide, however, plot within the principal component space of the spreading ridges. We suggest that this is likely due to the over-printing of pre-existing morphological features, and the landslide's burial beneath up to 450 m of sediments – both of which may result in the present-day morphology of the Tampen Slide's compressional ridges not being reflective of their formative process.

Neglecting the points from the Tampen Slide toe-compressional ridges, our results show a strong link between process and morphology that can be recognized using a semi-automated method with minimal interpreter input. This makes it a technique that can quickly and easily be applied to other regions, which is a vital step for validating our results and improving upon the methodology. A machine learning or random forest approach would be an important step towards automatic characterization of ridges, i.e. identifying the process responsible for their formation based on the ridge morphology. Such an approach, however, requires large volumes of data. Moreover, our analysis highlights the importance of data resolution – we note that a coarse grid spacing results in smoothing of the morphology and the loss of important morphological information, even for long wavelength features. While this method shows promise, bathymetric data of high-enough resolution to perform this analysis are often not publicly available.

Acknowledgements

We thank TGS for allowing us to work with the 3D seismic data from the Tampen Slide headwall, and Michael Strasser and Flavio Anselmetti for allowing us to work with their bathymetric data from Lake Zurich (M.S.) and Lake Lucerne (F.A.). We also thank Morelia Urlaub for constructive discussions that aided the development of these ideas.

References

Antobreh, A. A. and Krastel, S. (2007). Mauritania Slide Complex: Morphology, seismic characterisation and processes of formation. *International Journal of Earth Sciences*, 96(3):451–472.

Barrett, R., Bellwald, B., Talling, P., Gross, F., Berndt, C., Micallef, A., Planke, S., Myklebust, R., and Krastel, S. (in review). Can a submarine megaslide on a passive margin fail along a single glide plane? *Journal of Geophysical Research: Solid Earth*.

Bogert, B. P. (1963). The quefrency alanysis of time series for echoes ; Cepstrum, pseudo-autocovariance, cross-cepstrum and saphe cracking. *Time Series Analysis*, pages 209–243.

Bugge, T., Belderson, R. H., and Kenyon, N. H. (1988). The Storegga Slide. *Royal Society of London Philosophical Transactions*, 325(A):357–388.

Bull, S., Cartwright, J., and Huuse, M. (2009). A review of kinematic indicators from mass-transport complexes using 3D seismic data. *Marine and Petroleum Geology*, 26(7):1132–1151.

Bull, S. and Cartwright, J. A. (2020). Line length balancing to evaluate multi-phase submarine landslide development: an example from the Storegga Slide, Norway. In Georgiopoulou, A., Amy, L., Benetti, S., Chaytor, J., Clare, M., Gamboa, D., Haughton, P., Moernaut, J., and Mountjoy, J., editors, *Subaqueous Mass Movements and Their Consequences: Advances in Process Understanding, Monitoring and Hazard Assessments*, volume 500, pages 531–549. Geological Society of London Special Publications, London.

Carter, L., Gavey, R., Talling, P. J., and Liu, J. T. (2014). Insights into submarine geohazards from breaks in subsea telecommunication cables. *Oceanography*, 24(3):58–67.

Clare, M., Chaytor, J., Dabson, O., Gamboa, D., Georgiopoulou, A., Eady, H., Hunt, J., Jackson, C., Katz, O., Krastel, S., León, R., Micallef, A., Moernaut, J., Moriconi, R., Moscardelli, L., Mueller, C., Normandeau, A., Patacci, M., Steventon, M., Urlaub, M., Völker, D., Wood, L., and Jobe, Z. (2018). A consistent global approach for the morphometric characterization of subaqueous landslides. In Lintern, G., Mosher, D., Moscardelli, L., Bobrowsky, P., Campbell, C., Chaytor, J., Clague, J., Georgiopoulou, A., Lajeunesse, P., Normandeau, A., Piper, D., Scherwath, M., Stacey, C., and Turmel, D., editors, *Subaqueous Mass Movements and Their Consequences*, pages 455–477. Geological Society of London Special Publications, London, 477 edition.

Clare, M. A., Vardy, M. E., Cartigny, M. J., Talling, P. J., Himsworth, M. D., Dix, J. K., Harris, J. M., Whitehouse, R. J., and Belal, M. (2017). Direct monitoring of active geohazards: Emerging geophysical tools for deep-water assessments. *Near Surface Geophysics*, 15(4):427–444.

Cooley, J. W. and Tukey, J. W. (1965). An algorithm for the machine calculation of complex Fourier series. *Mathematics of Computation*, 19:297–301.

Frey-Martínez, J., Cartwright, J., and James, D. (2006). Frontally confined versus frontally emergent submarine landslides: A 3D seismic characterisation. *Marine and Petroleum Geology*, 23(5):585–604.

Gafeira, J., Long, D., Scrutton, R., and Evans, D. (2010). 3D seismic evidence of internal structure within Tampen Slide deposits on the North Sea Fan: are chaotic deposits that chaotic? *Journal of the Geological Society*, 167:605–616.

Haflidason, H., Sejrup, H. P., Nygård, A., Mienert, J., Bryn, P., Lien, R., Forsberg, C. F., Berg, K., and Masson, D. (2004). The Storegga Slide: Architecture, geometry and slide development. *Marine Geology*, 213(1-4):201–234.

Haflidason, H., Lien, R., Sejrup, H. P., Forsberg, C. F., and Bryn, P. (2005). The dating and morphometry of the Storegga Slide. *Marine and Petroleum Geology*, 22:123–136.

Hampton, M., Lee, H., and Locat, J. (1996). Submarine landslides. *Reviews of Geophysics*, 34(1):33–59.

Heezen, B. C. and Ewing, M. (1952). Turbidity currents and submarine slumps, and the 1929 Grand Banks Earthquake. *American Journal of Science*, 250:849–873.

Hilbe, M., Anselmetti, F. S., Eilertsen, R. S., Hansen, L., and Wildi, W. (2011). Subaqueous

morphology of Lake Lucerne (Central Switzerland): Implications for mass movements and glacial history. *Swiss Journal of Geosciences*, 104(3):425–443.

Hilbe, M. and Anselmetti, F. S. (2014). Signatures of slope failures and riverdelta collapses in a perialpine lake (Lake Lucerne, Switzerland). *Sedimentology*, 61(7):1883–1907.

Hjelstuen, B. and Grinde, S. (2016). 3D Seismic Investigations of Pleistocene Mass Transport Deposits and Glacigenic Debris Flows on the North Sea Fan, NE Atlantic Margin. In Lamarche, G., Mountjoy, J., Bull, S., Hubble, T., Krastel, S., Lane, E., Micallef, A., Moscardelli, L., Mueller, C., Pecher, I., and Woelz, S., editors, *Submarine Mass Movements and their Consequences, Advances in Natural and Technological Hazards Research*, pages 265–272. Springer, Cham, Switzerland, 41 edition.

Hjelstuen, B. O., Sejrup, H. P., Haflidason, H., Nygård, A., Berstad, I. M., and Knorr, G. (2004). Late Quaternary seismic stratigraphy and geological development of the south Vøring margin, Norwegian Sea. *Quaternary Science Reviews*, 23(16-17):1847–1865.

Jolliffe, I. T. and Cadima, J. (2016). Principal component analysis: a review and recent developments. *Philosophical Transactions of the Royal Society A: Mathematical, Physical and Engineering Sciences*, 374(20150202).

Kelts, K. and Hsü, K. J. (1980). Resedimented facies of 1875 Horgen slumps in Lake Zurich and a process model of longitudinal transport of turbidity currents. *Eclogae Geologicae Helvetiae*, 73(1):271–281.

King, E. L., Sejrup, H. P., Haflidason, H., Elverhøi, A., and Aarseth, I. (1996). Quaternary seismic stratigraphy of the North Sea Fan: glacially-fed gravity flow aprons, hemipelagic sediments, and large submarine slides. *Marine Geology*, 130(3-4):293–315.

Korup, O., Clague, J. J., Hermanns, R. L., Hewitt, K., Strom, A., and Weidinger, J. (2007). Giant landslides, topography, and erosion. *Earth and Planetary Science Letters*, 261(3-4):578–589.

Kvalstad, T. J., Andresen, L., Forsberg, C. F., Berg, K., Bryn, P., and Wangen, M. (2005). The Storegga slide: Evaluation of triggering sources and slide mechanics. *Marine and Petroleum Geology*, 22(1-2):245–256.

Lastras, G., Canals, M., and Urgeles, R. (2003). Lessons from sea-floor and subsea-floor imagery of the BIG'95 debris flow scar and deposit. In Locat, J. and Mienert, J., editors, *Submarine Mass Movements and Their Consequences*, pages 425–431. Kluwer Acad., Dordrecht, Netherlands.

Lecours, V., Devillers, R., Simms, A. E., Lucieer, V. L., and Brown, C. J. (2017). Towards a framework for terrain attribute selection in environmental studies. *Environmental Modelling & Software*, 89:19–30.

Lefebvre, A., Ernstsen, V. B., and Winter, C. (2011). Bedform characterization through 2D spectral analysis. *Journal of Coastal Research*, 64:781–785.

Li, W., Alves, T. M., Urlaub, M., Georgiopoulou, A., Klaucke, I., Wynn, R. B., Gross, F., Meyer, M., Repschläger, J., Berndt, C., and Krastel, S. (2017). Morphology, age and sediment dynamics of the upper headwall of the Sahara Slide Complex, Northwest Africa: Evidence for a large Late Holocene failure. *Marine Geology*, 393:109–123.

Masson, D. G., Wynn, R. B., and Talling, P. J. (2010). Large Landslides on Passive Continental Margins: Processes, Hypotheses and Outstanding Questions. In Mosher, D. C., Moscardelli, L., Shipp, R., Chaytor, J., Baxter, C., Lee, H., and Urgeles, R., editors, *Submarine Mass Movements*

and Their Consequences: Advances in Natural and Technological Hazards Research, volume 28, pages 153–165. Springer, Dordrecht, Netherlands.

Micallef, A., Berndt, C., Masson, D. G., and Stow, D. A. V. (2007a). A technique for the morphological characterization of submarine landscapes as exemplified by debris flows of the Storegga Slide. *Journal of Geophysical Research: Earth Surface*, 112(2):1–15.

Micallef, A., Berndt, C., Masson, D. G., and Stow, D. A. V. (2007b). Fractal statistics of the Storegga Slide. In Lykousis, V., Sakellariou, D., and Locat, J., editors, *Submarine Mass Movements and Their Consequences: Advances in Natural and Technological Hazards Research*, pages 3–10. Springer, Dordrecht, Netherlands, 27 edition.

Micallef, A., Masson, D. G., Berndt, C., and Stow, D. A. (2007c). Morphology and mechanics of submarine spreading: A case study from the Storegga Slide. *Journal of Geophysical Research: Earth Surface*, 112(3):1–21.

Micallef, A., Masson, D. G., Berndt, C., and Stow, D. A. (2009). Development and mass movement processes of the north-eastern Storegga Slide. *Quaternary Science Reviews*, 28(5-6):433–448.

Micallef, A., Georgiopoulou, A., Mountjoy, J., Huvenne, V. A., Iacono, C. L., Le Bas, T. P., Del Carlo, P., and Otero, D. C. (2016a). Outer shelf seafloor geomorphology along a carbonate escarpment: The eastern Malta Plateau, Mediterranean Sea. *Continental Shelf Research*, 131(October):12–27.

Micallef, A., Masson, D. G., Berndt, C., and Stow, D. A. (2016b). Submarine spreading in the Storegga Slide, Norwegian Sea. In Dowdeswell, J. A., Canals, M., Jakobsson, M., Todd, B. J., Dowdeswell, E., and Hogan, K. A., editors, *Atlas of Submarine Glacial Landforms: Modern, Quaternary and Ancient*, pages 411–412. Geological Society of London, Memoirs, London, 46 edition.

Micallef, A., Camerlenghi, A., Georgiopoulou, A., Garcia-Castellanos, D., Gutscher, M. A., Lo Iacono, C., Huvenne, V. A., Mountjoy, J. J., Paull, C. K., Le Bas, T., Spatola, D., Facchin, L., and Accettella, D. (2019). Geomorphic evolution of the Malta Escarpment and implications for the Messinian evaporative drawdown in the eastern Mediterranean Sea. *Geomorphology*, 327:264–283.

Moscardelli, L. and Wood, L. (2016). Morphometry of mass-transport deposits as a predictive tool. *Bulletin of the Geological Society of America*, 128(1-2):47–80.

Mountjoy, J. and Micallef, A. (2018). Submarine Landslides. In Micallef, A., Krastel, S., and Savini, A., editors, *Submarine Geomorphology*, pages 235–250. Springer Geology, Cham, Switzerland.

Nygård, A., Sejrup, H. P., Haflidason, H., and Bryn, P. (2005). The glacial North Sea Fan, southern Norwegian Margin: Architecture and evolution from the upper continental slope to the deep-sea basin. *Marine and Petroleum Geology*, 22(1-2):71–84.

Prior, D. B., Bornhold, B., and Johns, M. (1984). Depositional characteristics of a submarine debris flow. *Journal of Geology*, 92:707–727.

Riley, S. J., DeGloria, S. D., and Elliot, R. (1999). A Terrain Ruggedness Index that Quantifies Topographic Heterogeneity. *Intermountain Journal of Sciences*, 5(1-4):23–27.

Sammartini, M., Moernaut, J., Anselmetti, F. S., Hilbe, M., Lindhorst, K., Praet, N., and Strasser, M. (2019). An atlas of mass transport deposits in lakes. *Geophysical Monograph Series*, 246:201–226.

Scandone, P., Patacca, E., Radoicic, R., Ryan, W. B., Cita, M. B., Rawson, M., Chezar, H., Miller, E., McKenzie, J., and Rossi, S. (1981). Mesozoic and Cenozoic rocks from Malta Escarpment (central Mediterranean). *Bulletin of the American Association of Petroleum Geology*, 65(7).

Schnellmann, M., Anselmetti, F. S., Giardini, D., McKenzie, J. A., and Ward, S. N. (2002). Prehistoric earthquake history revealed by lacustrine slump deposits. *Geology*, 30(12):1131–1134.

Schnellmann, M., Anselmetti, F. S., Giardini, D., and McKenzie, J. A. (2005). Mass movement-induced fold-and-thrust belt structures in unconsolidated sediments in Lake Lucerne (Switzerland). *Sedimentology*, 52(2):271–289.

Schnellmann, M., Anselmetti, F. S., Giardini, D., and Mckenzie, J. A. (2006). 15,000 Years of massmovement history in Lake Lucerne: Implications for seismic and tsunami hazards. *Eclogae Geologicae Helvetiae*, 99(3):409–428.

Schönke, M., Feldens, P., Wilken, D., Papenmeier, S., Heinrich, C., Schneider von Deimling, J., Held, P., and Krastel, S. (2017). Impact of Lanice conchilega on seafloor microtopography off the island of Sylt (German Bight, SE North Sea). *Geo-Marine Letters*, 37(3):305–318.

Sejrup, H. P., Haflidason, H., Hjelstuen, B. O., Nygård, A., Bryn, P., and Lien, R. (2004). Pleistocene development of the SE Nordic Seas margin. *Marine Geology*, 213(1-4):169–200.

Solheim, A., Berg, K., Forsberg, C. F., and Bryn, P. (2005). The Storegga Slide complex: Repetitive large scale sliding with similar cause and development. *Marine and Petroleum Geology*, 22(1-2 SPEC. ISS.):97–107.

Strasser, M. and Anselmetti, F. S. (2008). Massmovement event stratigraphy in Lake Zurich; A record of varying seismic and environmental impacts. *Beiträge zur Geologie der Schweiz, Geotechnische Serie*, 95:23–41.

Strupler, M., Hilbe, M., Anselmetti, F. S., Kopf, A. J., Fleischmann, T., and Strasser, M. (2017). Probabilistic stability evaluation and seismic triggering scenarios of submerged slopes in Lake Zurich (Switzerland). *Geo-Marine Letters*, 37(3):241–258.

Talling, P., Clare, M., Urlaub, M., Pope, E., Hunt, J., and Watt, S. (2014). Large Submarine Landslides on Continental Slopes: Geohazards, Methane Release, and Climate Change. *Oceanography*, 27(2):32–45.

Wilson, M. F., O'Connell, B., Brown, C., Guinan, J. C., and Grehan, A. J. (2007). Multiscale terrain analysis of multibeam bathymetry data for habitat mapping on the continental slope. *Marine Geodesy*, 30:3–35.

Chapter 6

Conclusion and Outlook

6.1 Conclusion

Subaqueous landslides can be prodigious in size and can have devastating consequences across the scale of ocean basins, but their inaccessibility and significant differences compared to terrestrial landslides mean that there are still many open questions about how they fail. Furthermore, there are few direct observations of subaqueous landslides and so understanding how past subaqueous landslides were emplaced is a critical step in constraining the hazard associated with similar landslides. The geometry and morphology of a landslide play a key role in putting together the puzzle of their failure mechanism; however, our understanding of these factors depends heavily on data coverage and resolution. This poses a particular problem for subaqueous landslides that have a large lateral and volumetric extent, and/or are buried, as it means that our understanding of the process of the landslide's emplacement is often based on widely-spaced data that do not cover the full extent of the landslide deposit.

Such is the case for the Monte Amarelo flank-collapse of the island of Fogo in the Cape Verdes (Chapter 3), whose offshore distribution had previously only been constrained by medium resolution (100x100 m grid cell size) multibeam bathymetric data. Using new, higher resolution (50x50 m grid) bathymetric data, together with decimeter-resolution parametric echo sounder data, we found that the lateral extent of the Monte Amarelo volcanic debris avalanche deposits is more than double that of the previous estimate. Furthermore, we found evidence (both in the parametric echo-sounder data and in sediment gravity cores) that suggests that the emplacement of the debris avalanche deposits triggered the contemporaneous, multi-phase failure of pre-existing seafloor sediments, and identify, for the first time, multiple tectonic-related mass-transport deposits on the submerged volcaniclastic

apron south of Fogo. The triggering of the failure of pre-existing seafloor sediments by the emplacement of volcanic debris avalanche deposits has previously been identified offshore of the islands of Martinique and Monserrat in the Lesser Antilles. Our results highlight that such secondarily-triggered failures may be even more widespread than previously thought, and should be considered when analysing and modelling volcanic flank-collapse scenarios.

While these findings present a step forward in our understanding of the Monte Amarelo flank-collapse, which, in turn, adds to our understanding of how other flank-collapses might occur, this analysis is largely qualitative. As such, the effects of subjectivity (interpreter bias) and data coverage cannot be ignored. While the lateral extent of the Monte Amarelo debris avalanche deposits is now better constrained by densely spaced parametric echo sounder profiles and high-resolution bathymetric data proximal to the island of Fogo, characterization of those deposits is limited by the penetration of the data, which is reduced due to the volcanic and hummocky nature of the deposits. Contrastingly, south of these hummocky debris avalanche deposits, the transparent/chaotic nature of the deposits, as well their base and intra-debris reflector(s), is clearly imaged. Here, however, the spacing between profiles is large, and morphological features are qualitatively described based on their appearance on, and variation between, single profiles. This means that features may not be fully characterized, or may be missed altogether. Furthermore, the lateral extent of the secondarily-triggered failure of the seafloor sediments, as well as that of the numerous mass transport deposits imaged on the slopes south of Fogo, remains poorly constrained. While qualitative studies such as this are a rich source of information that helps us to better understand landslides and the process of failure, they also leave many questions unanswered.

High-resolution, 3D seismic datasets, such as that presented in Chapter 4, are a valuable resource that enable the morphology of the landslide deposits to be studied at a high level of detail, both qualitatively and quantitatively. Similarly to the Monte Amarelo flank-collapse deposits, whose lateral extent and geometry were previously only constrained by sparse data, previous analysis of the Tampen Slide was based on regional seismic profiles and smaller 3D seismic cubes that do not encompass the full extent of the headwall. Such large submarine landslides (also called megaslides) were previously thought to develop retrogressively, with numerous small volume failures over multiple glide planes accounting for their prodigious volumes. Our findings show, however, that submarine megaslides can also develop during a single phase, and along a single glide plane. Furthermore, unlike other megaslides on passive margins, a large volume of the Tampen Slide deposits (>720 km^3) remains within the confines of the headwall. We suggest that this is likely a result of the Møre Marginal High, a volcanic basement high that runs parallel to the western sidewall of the Tampen Slide and prevented the landslide deposits from running out downslope. The high resolution and extensive lateral coverage of the 3D data enables us to study the morphology of the

Tampen Slide at a high level of detail, and we document regions of extension (spreading) and compression, as well as longitudinal chutes, and large-scale (>40 m high) longitudinal ridges within the slide deposits. These morphological features provide critical information about the process of emplacement of the Tampen Slide.

However, high-resolution, 3D seismic datasets that encompass landslide deposits, such as that in Chapter 4, are uncommon and often not widely accessible. Consequently, studies that aim to compare and contrast the morphology and geometry of landslide deposits must make use of data of varying resolution and extent and, therefore, tend to be more qualitative rather than quantitative and are prone to interpreter bias. As landslide morphology is often inferred to be indicative of the formative process (either for the whole landslide, or for a region within the slide deposits), it is particularly important that the morphology is correctly interpreted. In Chapter 5, I make use of a quantitative, semi-automatic approach in order to distinguish between three types of elongated ridges that are found within subaqueous landslide deposits – spreading ridges within the headwall domain; compressional ridges within the landslide toe; and lateral margin compression. These ridges develop during different processes, but have strikingly similar geomorphology in map-view. This means that they can be difficult to interpret in areas of low bathymetric data coverage, or where seismic profiles are not available, or do not enable a cross-sectional view of the ridges. This is particularly a problem for landslide complexes, which have a large lateral extent and total volume. Moreover, such landslides often involve many smaller failures that can be difficult to distinguish from one other. The method presented in Chapter 5 – a combined approach involving largely automated, spectral, bathymetric and principal component analysis of digital elevation models – successfully distinguishes between spreading, lateral-margin compression and toe-compressional ridges in a variety of settings. While our results should be validated using additional data, they demonstrate that morphometric statistics of ridges can be quantitatively linked to their formational process. This suggests that we may be able to use a machine learning approach to work backwards and identify the process responsible for the formation of particular ridges based on their morphometric statistics. The application of quantitative, semi-automatic methodology such as this is critical in order to move towards a less subjective interpretation of subaqueous landslide deposits. While qualitative analysis of landslides continues to be a powerful tool to investigate individual landslides and learn about their dynamics, it remains subjective. Quantitative analysis should result in a more systematic, consistent, and automatic classification of landslide morphology, and the methodology presented in Chapter 5 acts as a starting point for this that can be adapted and expanded upon in future work. Both quantitative and qualitative analyses, however, are still limited by data availability and resolution.

6.2 Ongoing and future work

Quantitative methods have been increasingly used in the analysis of the morphology and geometry of subaqueous landslides over the last twenty years (e.g. Prior et al., 1984, Frey-Martínez et al., 2006, Bull et al., 2009, Moscardelli and Wood, 2016). Furthermore, the landslide community has also worked to adopt standardized approaches for characterizing landslide morphology (e.g. Clare et al., 2018). These have both helped to reduce problems of interpreter subjectivity. Subaqueous landslides, however, are complex and non-unique, and a consistent characterization is made more challenging by their post-depositional burial, erosion, or subsequent remobilization. Furthermore, landslide characterization depends on data coverage and resolution, and many landslides remain undiscovered or are not well constrained. To constrain a landslide's morphology and its emplacement thoroughly requires a variety of data – both geophysical (high-resolution, closely spaced 2D or 3D seismic profiles), petrological (sediment cores), and geotechnical (including measurements of *in situ* sediment properties), and this variety of data is only rarely available for a particular landslide. The complicated morphology of a landslide, together with the effect of post-depositional processes, and data availability and resolution can make it difficult to reconstruct the landslide's original morphology and geometry. This, in turn, can make it difficult to constrain how a similar landslide might fail in the future – information that is critical for quantifying the associated hazards, including the potential displacement of the water column and the development of tsunami waves (e.g. Harbitz et al., 2014, Grilli et al., 2019).

Understanding parts of the landslide, and their relationship to each other, enables the whole landslide to be better constrained. Consequently, quantitatively parameterizing landslide morphology at a smaller scale, such as in Chapter 5 of this thesis, could prove to be an effective way to constrain the geometry and emplacement of the overall landslide. The minimal user input that this method requires (just the selection of analysis window size and window cells that contain ridges) means that it is highly adaptable to different settings and data resolutions. However, large amounts of data are required in order to automate such a process, i.e. to automatically classify ridges according to their geomorphology. Moreover, such analysis is only possible when the data resolution is high and the ridges can be distinguished from the surrounding slide morphology. Such data (where they exist) are often not publicly available. The next step is to refine this methodology and to test the benefit of further parameters, such as planar shape (convex vs concave) and slope gradient, for the classification of the different types of ridges. The aim is that this should help to better distinguish the ridges from one another, so that an automatic clustering approach would correctly classify the ridges into their different groups. If successful, this would enable ridges from regions with low data coverage and within large slide complexes to be distinguished, while ensuring

that the morphological features are correctly linked to their formative process. Furthermore, a similar approach – comparing the spectral analysis and bathymetric statistics of one region to another – could also help to distinguish slide deposits from the adjacent unfailed material, and semi-automatically delineate the landslide extent. Similar work is also underway to extract landslide deposits from 2D seismic data by using statistical and diffraction analysis to exploit their chaotic character (Ford and Camerlenghi, 2020). Combining these two approaches – to extract subaqueous landslides both from bathymetric and seismic data – would be a powerful way to detect landslides non-subjectively. Nonetheless, qualitative analysis still remains a powerful and necessary tool for investigating landslide morphology and dynamics.

Work is also ongoing and planned for the two end-member landslides that were investigated in Chapters 3 and 4 of this thesis (the Monte Amarelo flank-collapse of the island of Fogo in the Cape Verdes, and the Tampen megaslide offshore Norway, respectively). While the lateral extent and character of the Monte Amarelo flank-collapse and the secondarily-triggered, multi-phase failure of seafloor sediments are now better constrained, the full lateral extent, as well as the relative timing of the seafloor sediment failures that were triggered by the emplacement of the debris avalanche deposits remains unknown. Analysis of the seismic data and detailed petrological analysis of sediment gravity cores that were collected during the research cruise M155 of RV Meteor (Figures 3.1 and 3.4) is still ongoing, but will hopefully be able to answer questions regarding the number and relative timing of flank-collapse events and turbidites. This information is critical for building a complete picture of the processes responsible for failure, which will support tsunami modelling and help us to understand how the risks posed by a future flank-collapse could be mitigated. The Monte Amarelo flank-collapse triggered one of the largest mega-tsunamis preserved in the geological record (Ramalho et al., 2015). Being able to characterize the deposits at a high level of detail and understand the sequence of events that occurred during the flank collapse will enable volcanogenic tsunami modelling to be integrated with physical evidence, which will result in the development of a much-improved tsunami impact model.

Similarly, despite the step forward in our understanding of the morphology and emplacement of the Tampen Slide (and the implication that other megaslides could also fail as a single mass, rather than as multiple smaller failures within a short amount of time; Chapter 4), there are still open questions about the Tampen Slide – its full lateral extent, volume and age remain poorly constrained. The age of the Tampen Slide, previously suggested to be ca. 130 ka, is constrained by regional 2D seismic profiles (Nygård et al., 2005), and the upper part of a single piston core (MD99-2283) proximal to the headwall (Lekens et al., 2009). The radiocarbon dates of that core, however, only extend to 40.2 ka, and the Tampen Slide may, in fact, be ca. 60 ka if sedimentation rates in the upper part of the core continue further

down (Lekens et al., 2009). Furthermore, minor sidewall collapses and spreading along the headwall also complicate identification of the youngest reflector cut by the Tampen Slide. Cores collected in 2014 in the Aegir Ridge, north of the Tampen Slide headwall, penetrated through two turbidites – a younger one that has an age of 8.2 ka, which correlates with the Storegga Slide, and another, which occurs immediately below the Storegga turbidite and is dated at 55-60 ka (Watts et al., 2016, Watts, 2019). That second turbidite is even thicker than the Storegga turbidite on some sub-bottom profiles, implying either that it is linked to an even larger slide, or that its headwall is closer to the Aegir Ridge. Such a headwall, however, is not evident from the bathymetry, and Watts et al. (2016) suggested that that second turbidite may be linked to the Tampen Slide. If this is the case, it implies that the Tampen Slide is much younger than previously thought, which means that large megaslides on the Norwegian continental margin (which can result in devastating tsunami as demonstrated by the Storegga Slide; Bondevik et al., 2005) occur more frequently than once per glacial cycle as suggested by the current model. This would have a significant impact on hazard assessment across the North Sea and its abutting countries. In collaboration with Pete Talling (Durham University, UK), and Haflidi Haflidason (University of Bergen, Norway), we submitted a ship-time proposal to investigate the turbidites in the Aegir Ridge. Our primary objectives are constrain (i) whether the turbidite within the Aegir Ridge is linked to the Tampen Slide (thereby better constraining the full extent, volume, and age of the Tampen Slide); (ii) confirming the age of that turbidite and constraining its regional distribution; and (iii) constraining the distribution of large volume, seismically opaque units beneath the two turbidites within the Aegir Ridge. The proposal has been accepted, and the cruise is scheduled for late January 2021.

References

Bondevik, S., Løvholt, F., Harbitz, C. B., Mangerud, J., Dawson, A., and Svendsen, J. I. (2005). The Storegga Slide tsunami – comparing field observations with numerical simulations. In *Ormen Lange – an Integrated Study for Safe Field Development in the Storegga Submarine Area*, pages 195–208. Elsevier.

Bull, S., Cartwright, J., and Huuse, M. (2009). A review of kinematic indicators from mass-transport complexes using 3D seismic data. *Marine and Petroleum Geology*, 26(7):1132–1151.

Clare, M., Chaytor, J., Dabson, O., Gamboa, D., Georgiopoulou, A., Eady, H., Hunt, J., Jackson, C., Katz, O., Krastel, S., León, R., Micallef, A., Moernaut, J., Moriconi, R., Moscardelli, L., Mueller, C., Normandeau, A., Patacci, M., Steventon, M., Urlaub, M., Völker, D., Wood, L., and Jobe, Z. (2018). A consistent global approach for the morphometric characterization of subaqueous landslides. In Lintern, G., Mosher, D., Moscardelli, L., Bobrowsky, P., Campbell, C., Chaytor, J., Clague, J., Georgiopoulou, A., Lajeunesse, P., Normandeau, A., Piper, D., Scherwath, M., Stacey, C., and Turmel, D., editors, *Subaqueous Mass Movements and Their Consequences*, pages 455–477. Geological Society of London Special Publications, London, 477 edition.

Ford, J. and Camerlenghi, A. (2020). Geostatistical characterization of internal structure of mass-transport deposits from seismic reflection images and borehole logs. *Geophysical Journal International*, 221(1):318–333.

Frey-Martínez, J., Cartwright, J., and James, D. (2006). Frontally confined versus frontally emergent submarine landslides: A 3D seismic characterisation. *Marine and Petroleum Geology*, 23(5):585–604.

Grilli, S. T., Tappin, D. R., Carey, S., Watt, S. F., Ward, S. N., Grilli, A. R., Engwell, S. L., Zhang, C., Kirby, J. T., Schambach, L., and Muin, M. (2019). Modelling of the tsunami from the December 22, 2018 lateral collapse of Anak Krakatau volcano in the Sunda Straits, Indonesia. *Scientific Reports*, 9(1):1–13.

Harbitz, C. B., Løvholt, F., and Bungum, H. (2014). Submarine landslide tsunamis: how extreme and how likely? *Natural Hazards*, 72:1341–1374.

Lekens, W. A. H., Haflidason, H., Sejrup, H. P., Nygard, A., Richter, T., Vogt, C., and Frederichs, T. (2009). Sedimentation history of the northern North Sea Margin during the last 150 ka. *Quaternary Science Reviews*, 28(5-6):469–483.

Moscardelli, L. and Wood, L. (2016). Morphometry of mass-transport deposits as a predictive tool. *Bulletin of the Geological Society of America*, 128(1-2):47–80.

Nygård, A., Sejrup, H. P., Haflidason, H., and Bryn, P. (2005). The glacial North Sea Fan, southern Norwegian Margin: Architecture and evolution from the upper continental slope to the deep-sea basin. *Marine and Petroleum Geology*, 22(1-2):71–84.

Prior, D. B., Bornhold, B., and Johns, M. (1984). Depositional characteristics of a submarine debris flow. *Journal of Geology*, 92:707–727.

Ramalho, R. S., Winckler, G., Madeira, J., Helffrich, G. R., Hipólito, A., Quartau, R., Adena, K., and Schaefer, J. M. (2015). Hazard potential of volcanic flank collapses raised by new megatsunami evidence. *Science Advances*, 1(9):1–11.

Watts, M., Talling, P., Hunt, J., Xuan, C., and van Peer, T. (2016). A new date for a large pre-Holocene Storegga Slide. In *EGU General Assembly*, Vienna, Austria.

Watts, M. (2019). *Submarine mega-slides from the Norwegian Continental margin and their relationship to periods of climatic change*. Doctoral thesis, University of Southampton.

Acknowledgments

"In Africa there is a concept known as Ubuntu – the profound sense that we are human only through the humanity of others; that if we are to accomplish anything in this world it will in equal measure be due to the work and achievement of others." – Nelson Mandela

To my primary supervisor, Sebastian Krastel, I owe a debt of gratitude. Sebastian, thank you for believing in me, for supporting me, and for challenging me to think critically and to challenge myself. Thank you for always being generous with your time, and for giving me opportunities to collaborate and broaden my mind, and the freedom to follow my curiosity. I have learnt so much from you, and it has been an honour to work with you over these last three years.

Thanks are also due to my secondary supervisors – Christian Berndt and Peter Talling. Thank you for asking challenging questions and for encouraging me to think more broadly. You both took pains to stress the importance of good writing that appeals to a more general audience, and my writing style will forever benefit from that. Further thanks to Pete, as well as to Aaron Micallef, Benjamin Bellwald, and Sverre Planke, for hosting me during research stays at your institutes over the last three years. Thank you for offering up your time and knowledge, and for making sure that I got as much as possible out of those visits. I look forward to ongoing and future collaborations with you.

I am also grateful to the many people who have been part of the working group here in Kiel over the last few years – thank you for the many lunches shared in the Mensa, and for spontaneous coffee breaks. I am especially grateful to Frederik Lenz, Arne Lohrberg, and Felix Gross, who shared the office with me. Thank you for being not just colleagues, but friends.

Thank you to Felix and Sandra Gross, Florian Petersen, Felix Wolf, Frederik Lenz and Tatjana Allers for always being there to lend a listening ear and for being patient with me as I learnt German. Thank you for the walks/runs, the meals, the card games, and the

many cups of coffee that we have shared. Thank you for making Kiel feel like home.

Thanks to Ricarda Gatter, Kate Heerema, and Maddalena Sammartini for the spontaneous video calls and mental health breaks over the last few years, and especially during the last phase of this PhD. It has been a privilege to walk this journey alongside you (although scattered across Europe). I am already looking forward to our next mountain holiday.

To Pippa, Derek, and Jenni Barrett – Mum, Dad, and little sis – thank you for always encouraging my crazy dreams even when they involve me moving to the opposite side of the world. Your unwavering support makes me feel brave and confident to step out into the unknown. I am so grateful to know that I can always depend on you, that you are always only ever a phone call away.

The work that led to this thesis would not have been possible without the support and encouragement of many people spread out over the globe. Writing a thesis during a global pandemic meant losing a lot of the structures and routines that I had built into my life. Thanks to the many people who texted, video-called, or just extended extra support to me during this time – you ensured that I kept my sanity (or, as my Mum would argue, what I had of it).

My work over the last three years was funded by the European Union's Horizon 2020 research and innovation programme under the Marie Sklodowska-Curie grant agreement No 721403, as part of project SLATE – 'Submarine LAndslides and Their impact on European continental margins'. Thank you to all the PIs, and especially to Katrin Huhn who led the project, for your work in initiating and obtaining funding for this project. The opportunities that we, as PhD students, have been exposed to over the course of the project will surely shape the course of our careers in the years to come.

Curriculum Vitae

Removed according to data protection regulations.

Aus datenschutzrechtlichen Gründen entfernt.

Publications

Peer-reviewed publications

- Riefstahl, F., Gohl, K., Davy, B., and **Barrett, R.** (2020). Extent and cessation of the mid-Cretaceous Hikurangi Plateau underthrusting: Impact on global plate tectonics and the submarine Chatham Rise. JGR Solid Earth, https://doi.org/10.1029/2020JB-019681
- **Barrett, R.**, Lebas, E., Ramalho, R., Klaucke, I., Kutterolf, S., Klügel, A., Lindhorst, K., Gross, F., and Krastel, S. (2019). Revisiting the tsunamigenic volcanic flank-collapse of Fogo Island in the Cape Verdes, offshore West Africa. Geological Society, London, Special Publications, n. 500, https://doi.org/10.1144/SP500-2019-187
- **Barrett, R.**, Davy, B., Stern, T., and Gohl, K. (2018). The strike-slip West Wishbone Ridge and the eastern margin of the Hikurangi Plateau. Geochemistry, Geophysics, Geosystems, 19, https://doi.org/10.1002/2017GC007372

Scientific communications

- Lenz, K-F., Gross, F., Klügel, A., **Barrett, R.**, Held, P., Lindhorst, K., Wintersteller, P., and Krastel, S. (2020). New insights into the magmatic system southeast of El Hierro from high-resolution 2D seismic data. EGU General Assembly 2020, EGU2020-15205, https://doi.org/10.5194/egusphere-egu2020-15205
- Klein, E., Lebas, E., Ramalho, R., **Barrett, R.**, Kutterolf, S., and Krastel, S. (2020). Evidence for the multi-phase nature of the Monte Amarelo flank collapse based on reflection seismic data offshore Fogo, Cape Verde. 80. DGG Jahrestagung, March 2020.
- **Barrett, R.**, Bellwald, B., Berndt, C., Micallef, A., Planke, S., Talling, P., Gross, F., Myklebust, R., and Krastel, S. (2020). Decameter-scale, flow-parallel ridges in a submarine megaslide: Tampen Slide, North Sea [Talk]. Nordic Geological Winter Meeting, Oslo, Norway, 8-10 January 2020.
- **Barrett, R.**, Bellwald, B., Krastel, S., Gross, F., Micallef, A., Planke, S., Berndt, C., Talling, P., and Myklebust, R. (2019). New Constraints on the Failure Mechanism and Kinematics of the Tampen Slide (North Sea) from 3D Seismic Data [Talk]. Geophysical Research Abstracts, Vol. 21, EGU2019-8050.
- Bellwald, B., Planke, S., **Barrett, R.**, Batchelor, C., and Myklebust, R. (2019). Characterization of Glacigenic Debris Flows, Megaslides and Contourites of the North Sea Fan from 3D Seismic Data [Talk]. Geophysical Research Abstracts Vol. 21, EGU2019-8130.
- Bellwald, B., Planke, S., **Barrett, R.**, Berndt, C., Manton. B., and Myklebust, R. (2019). Characterization of Glacigenic Debris Flows and Megaslides of the North Sea

Trough Mouth Fan from 3D Seismic Data [Talk]. NGF Winter Conference, Bergen, Norway.

- **Barrett, R. S.**, Krastel, S., Micallef, A., Berndt, C., and Gross, F. (2018). Towards Semi-Automatic Delineation of Submarine Landslides [Poster]. 8th International Symposium on Submarine Mass Movements and Their Consequences, Victoria, British Columbia, Canada, 7 - 9 May 2018.
- Davy, B., Gohl, K., Werner, R., **Barrett, R. S.**, and Riefstahl, F. (2017). The crustal structure of the eastern Chatham Rise region - Results of the 2016 geophysical survey SO246 by the R/V Sonne [Talk]. Annual Conference of the Geoscience Society of New Zealand, Auckland, 28 November 2017 - 1 December 2017.
- **Barrett, R. S.**, Davy, B., Stern, T. and Gohl, K. (2016). The Wishbone Ridge at the Chatham Rise intersection: fault characteristics and tectonic implications [Poster], Geosciences 2016, Wanaka, New Zealand.

Appendix

Chapter 5

Quantitative morphometric analysis of ridges in sub-aqueous landslides

This section includes parameter plots for both the high- and low-resolution datasets analysed in Chapter 5. In the low-resolution dataset, the data from the Tampen and Storegga Slides, which contain both extensional and one type of compressional ridge, are down-sampled while the data from the Malta Escarpment, Lake Lucerne, and Lake Zurich have the same resolution in both datasets. Areas for which both resolutions are considered are plotted on the same page in the following figures.

- Figures 1 and 2 show the parameters from the lateral-margin compression zone of the Storegga Slide.
- Figures 3 - 7 show the parameters calculated for the toe-compressional ridges in mass transport deposits within the Tampen Slide, Lake Lucerne, and Lake Zurich.
- Figures 8 - 20 show the parameters calculated for the spreading ridges on the Malta Escarpment, and in the headwalls of the Storegga and Tampen Slides.

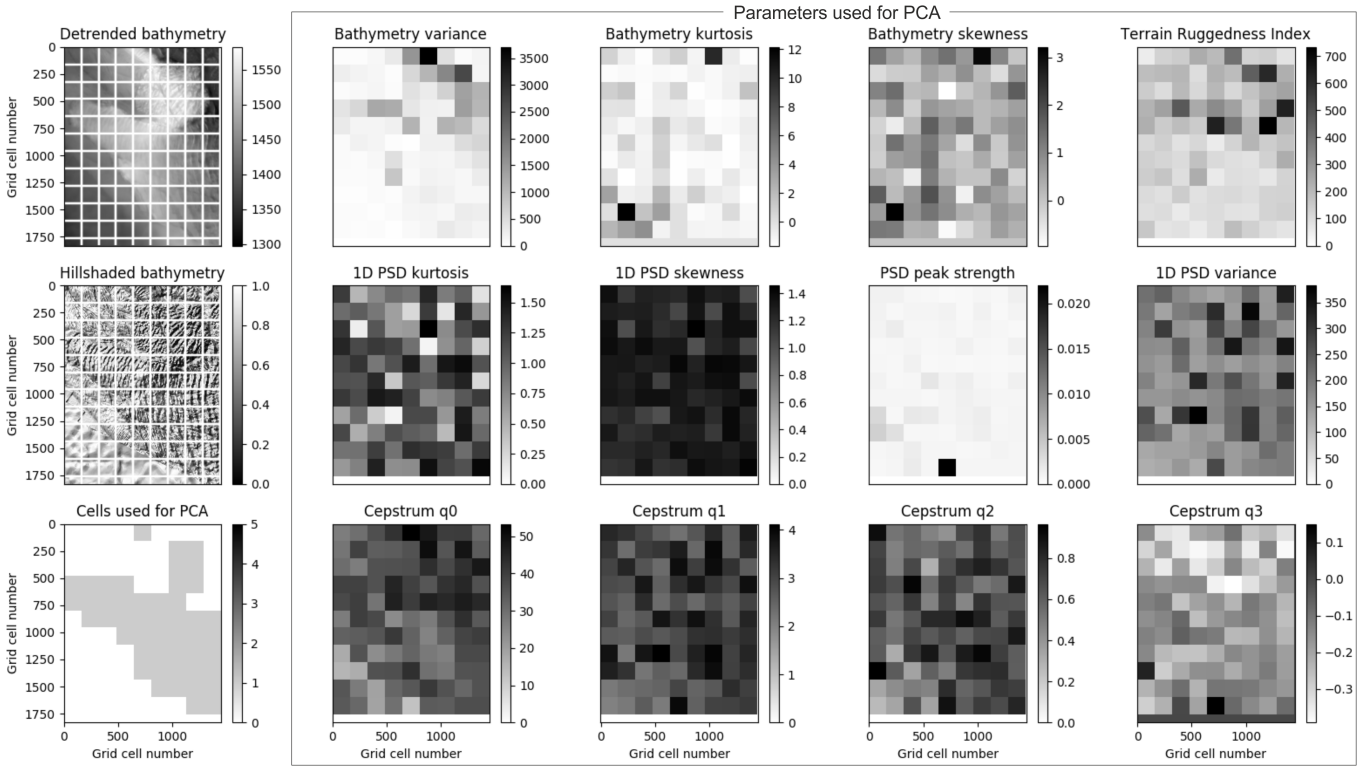

Figure 1: Statistical parameters extracted from the low-resolution version of the bathymetry and fourier analysis power spectrum of lateral-margin compression along the western headwall of the Storegga Slide (widely referred to as 'The Compression Zone').

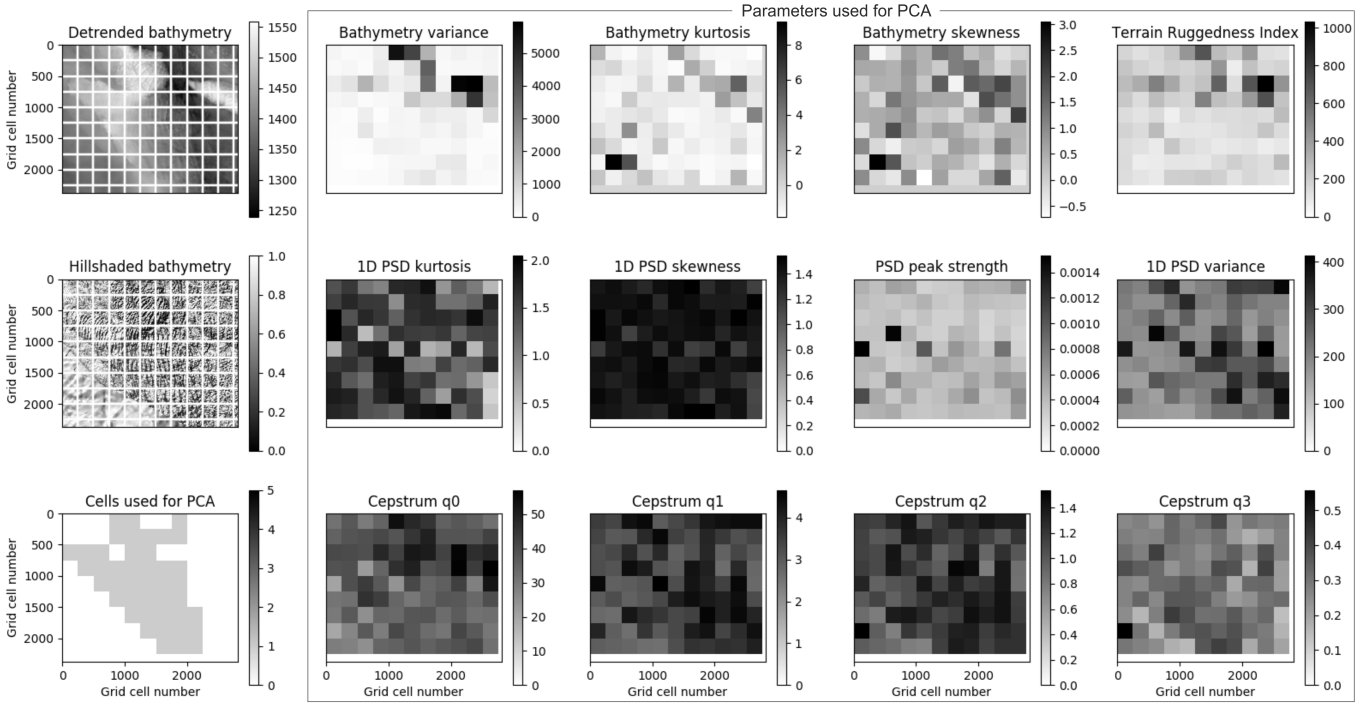

Figure 2: Statistical parameters extracted from the high-resolution version of the bathymetry and fourier analysis power spectrum of lateral-margin compression along the western headwall of the Storegga Slide (widely referred to as 'The Compression Zone').

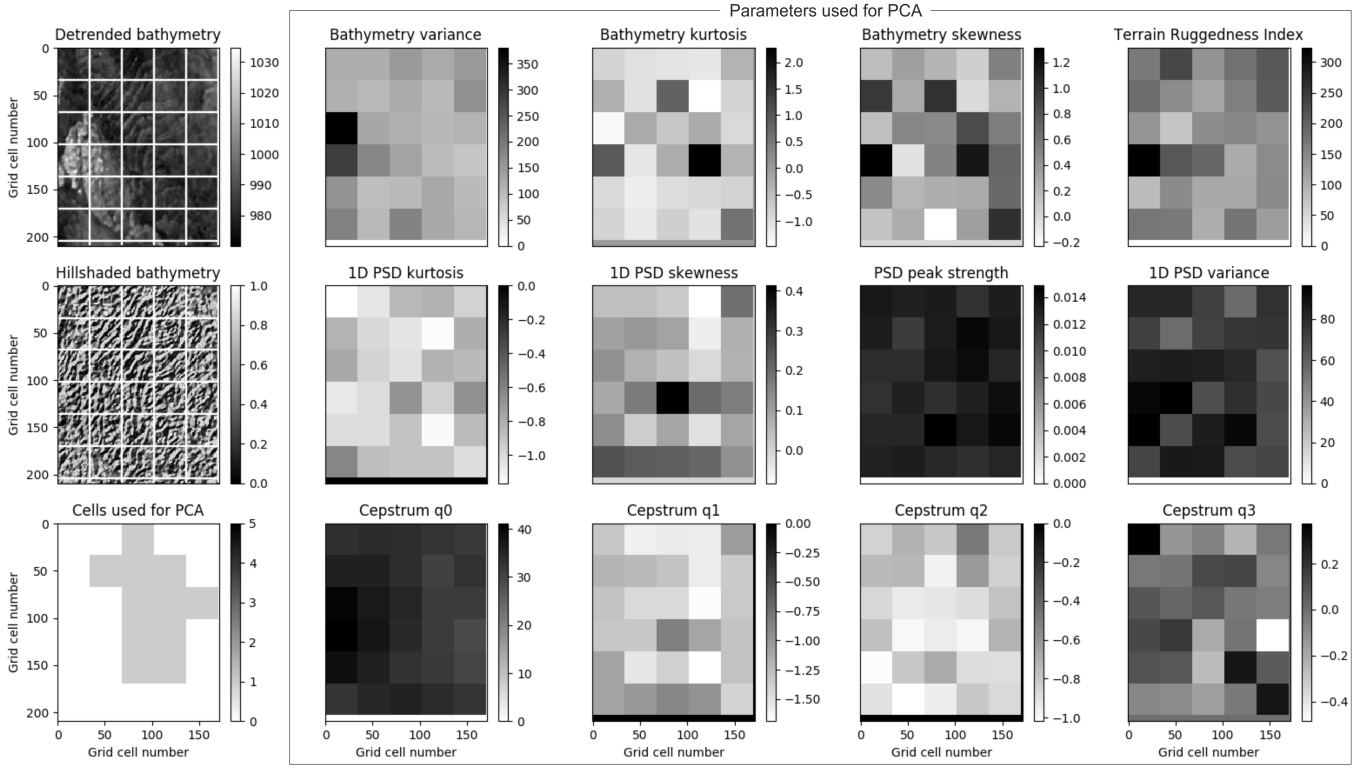

Figure 3: Statistical parameters extracted from the low-resolution version of the bathymetry and fourier analysis power spectrum of toe-compressional ridges at the toe of a subsequent retrogressive debris flow within the Tampen Slide headwall. Data courtesy of TGS.

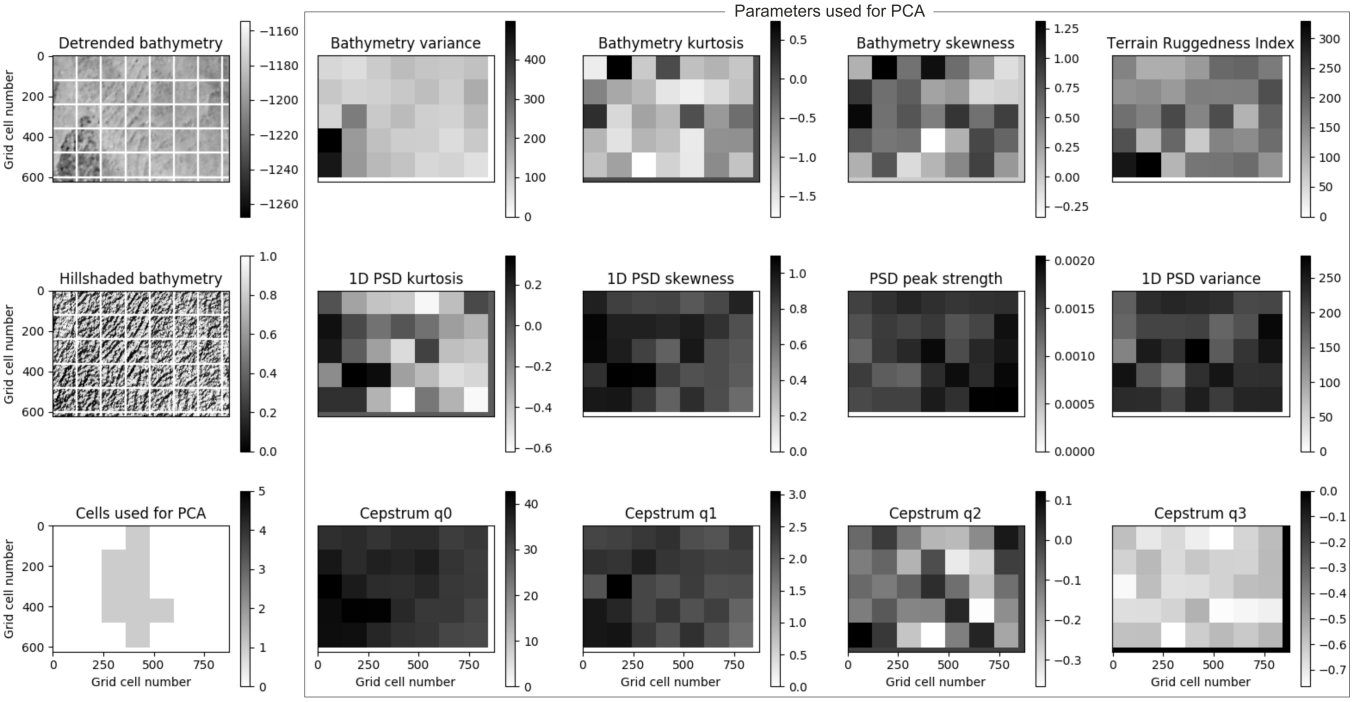

Figure 4: Statistical parameters extracted from the high-resolution version of the bathymetry and fourier analysis power spectrum of toe-compressional ridges at the toe of a subsequent retrogressive debris flow within the Tampen Slide headwall. Data courtesy of TGS.

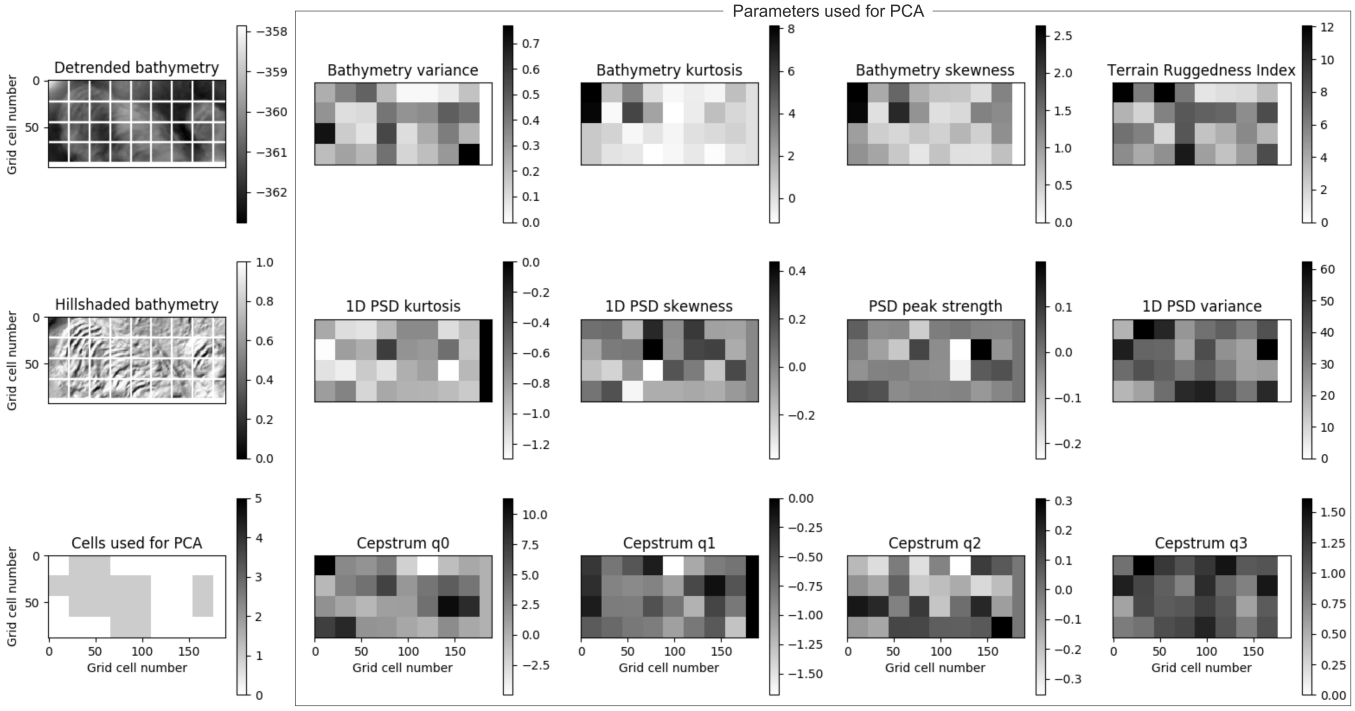

Figure 5: Statistical parameters extracted from the bathymetry and fourier analysis power spectrum of toe-compressional ridges of mass transport deposits within Lake Lucerne (Zone 1).

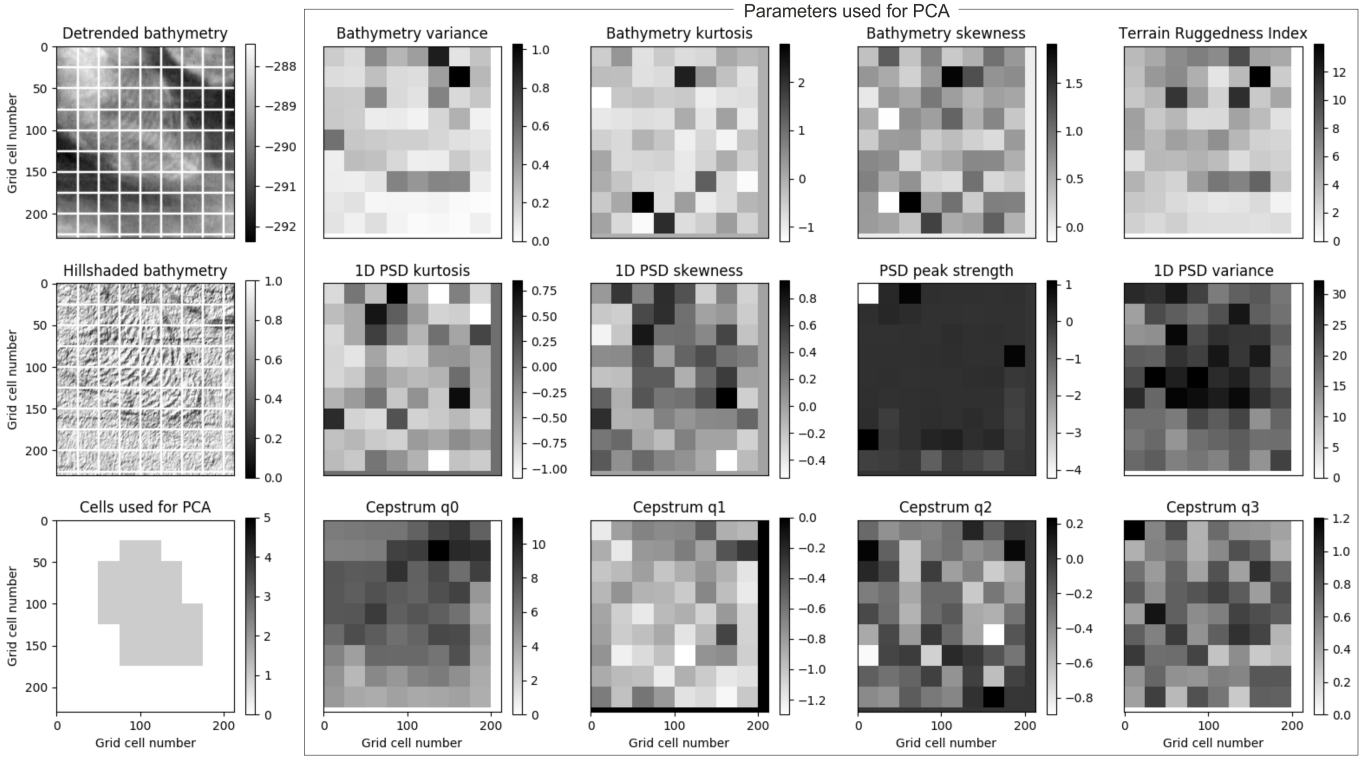

Figure 6: Statistical parameters extracted from the bathymetry and fourier analysis power spectrum of toe-compressional ridges of mass transport deposits within Lake Lucerne (Zone 2).

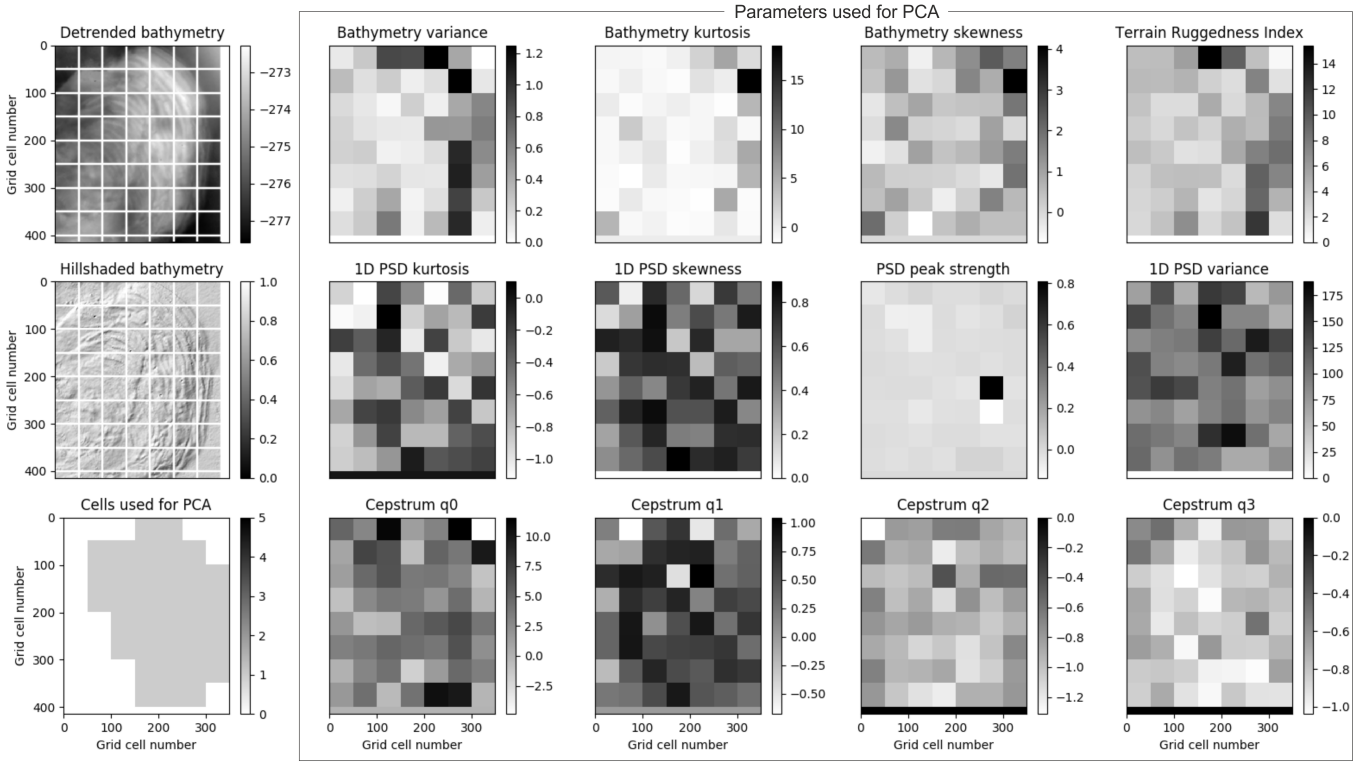

Figure 7: Statistical parameters extracted from the bathymetry and fourier analysis power spectrum of toe-compressional ridges of mass transport deposits within Lake Zurich (Zone 1).

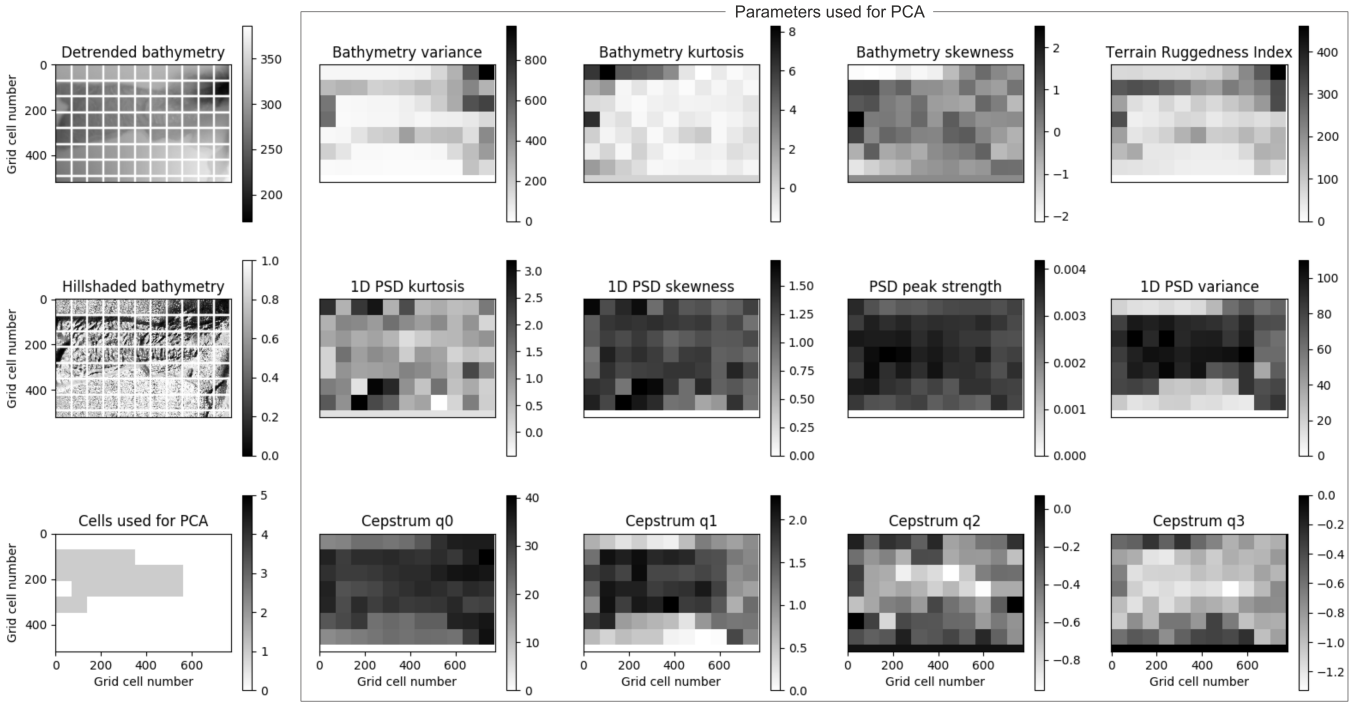

Figure 8: Statistical parameters extracted from the bathymetry and fourier analysis power spectrum of spreading ridges on the Malta Escarpment.

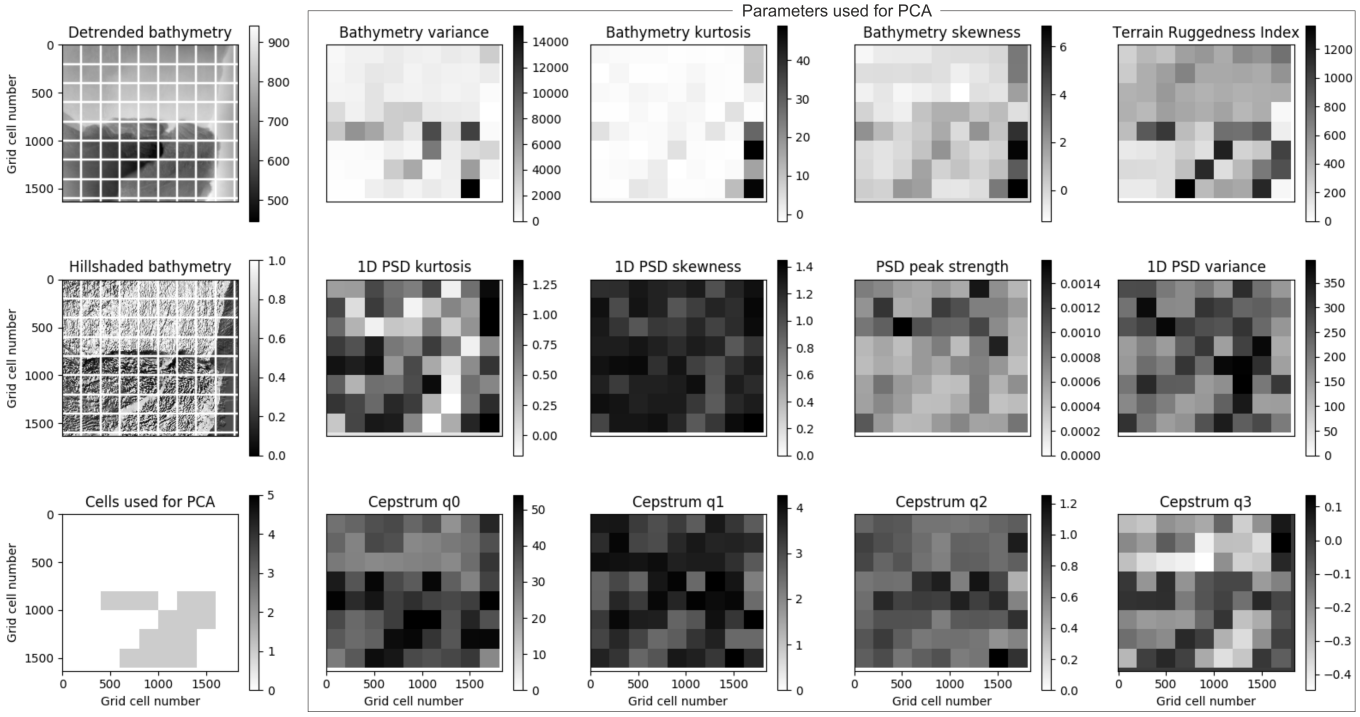

Figure 9: Statistical parameters extracted from the low-resolution version of the bathymetry and fourier analysis power spectrum of spreading ridges within the Storegga Slide headwall (Spreading Zone 1).

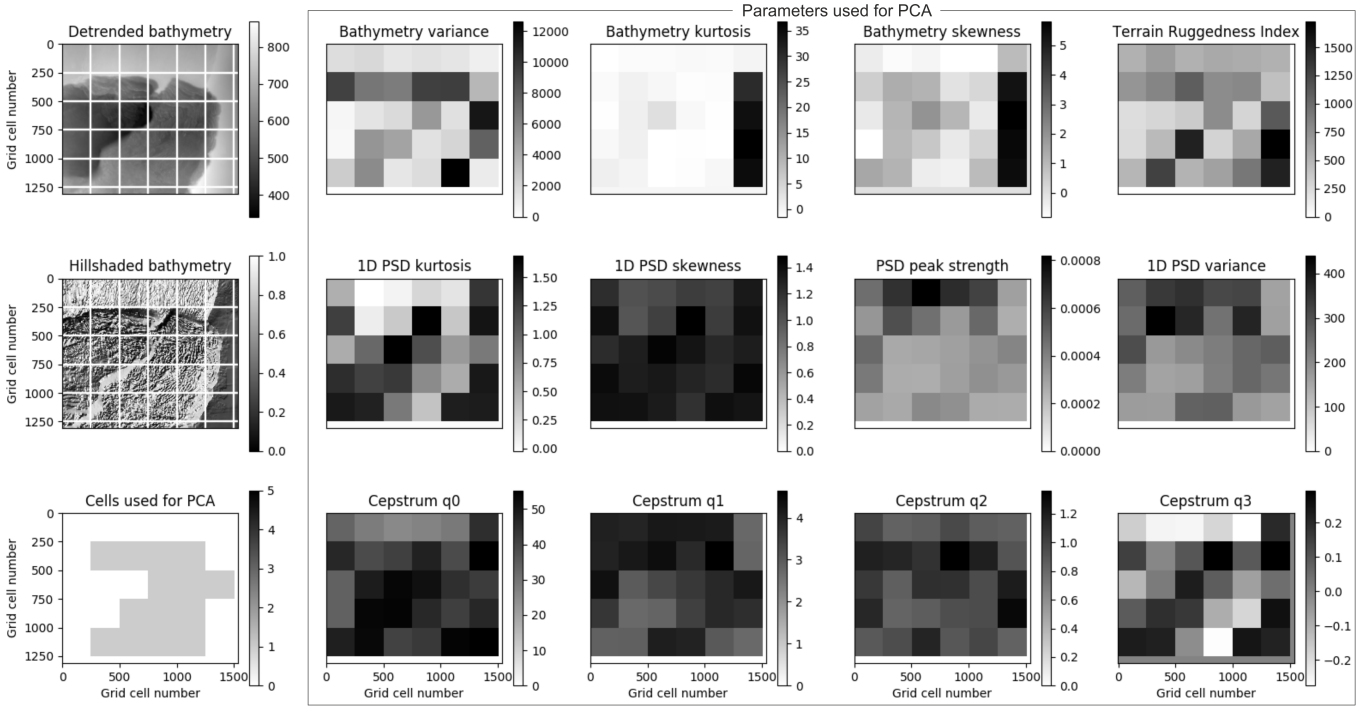

Figure 10: Statistical parameters extracted from the high-resolution version of the bathymetry and fourier analysis power spectrum of spreading ridges within the Storegga Slide headwall (Spreading Zone 1).

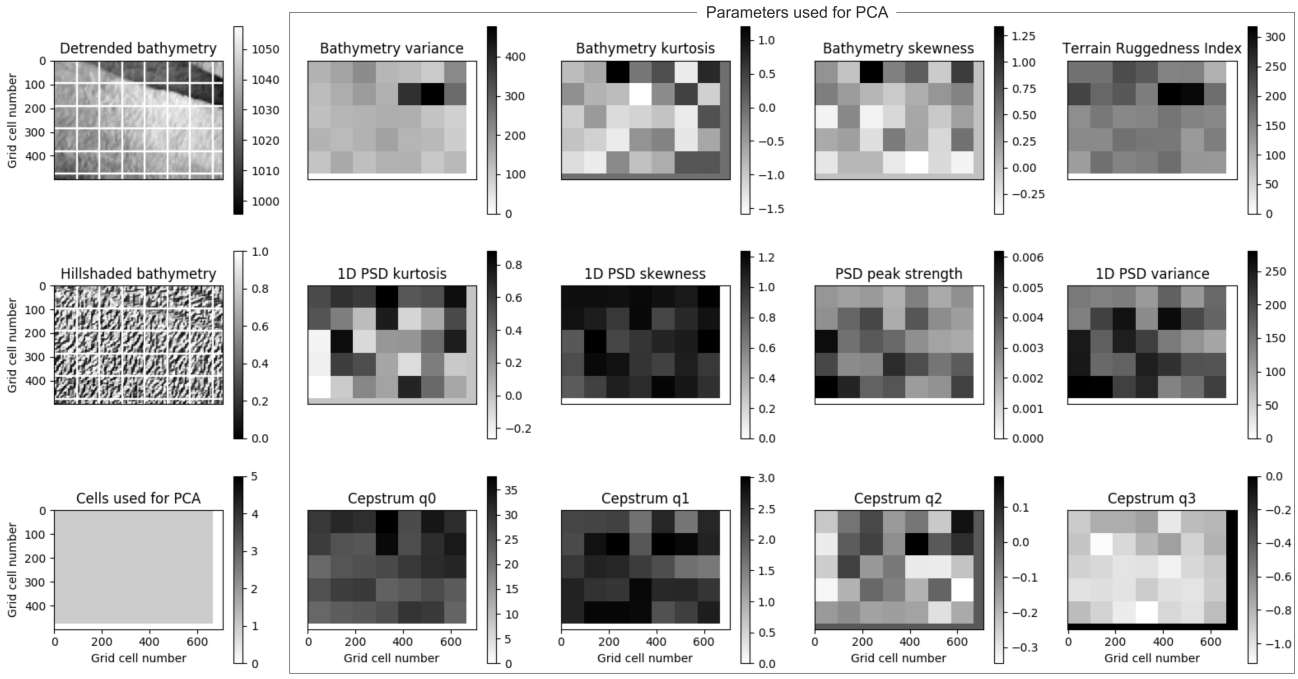

Figure 11: Statistical parameters extracted from the low-resolution version of the bathymetry and fourier analysis power spectrum of spreading ridges within the Storegga Slide headwall (Spreading Zone 2).

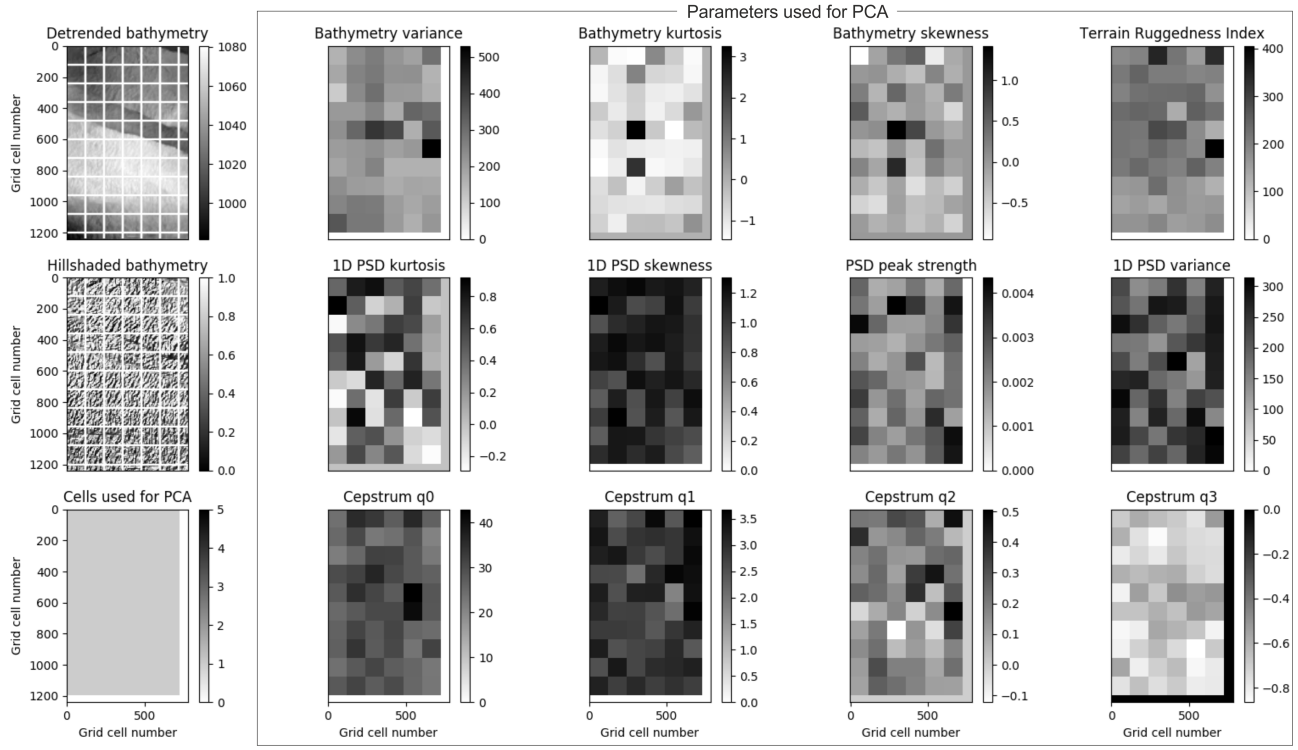

Figure 12: Statistical parameters extracted from the high-resolution version of the bathymetry and fourier analysis power spectrum of spreading ridges within the Storegga Slide headwall (Spreading Zone 2).

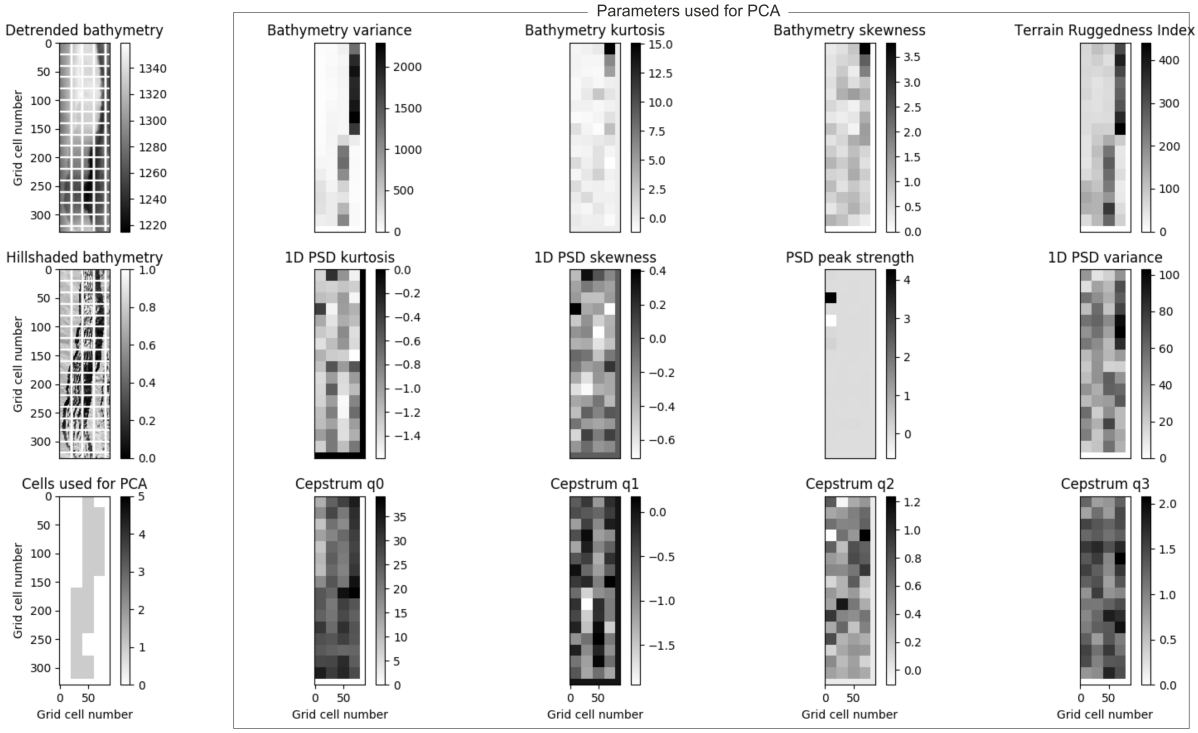

Figure 13: Statistical parameters extracted from the low-resolution version of the bathymetry and fourier analysis power spectrum of spreading ridges within the Tampen Slide headwall (Spreading Zone 1). Data courtesy of TGS.

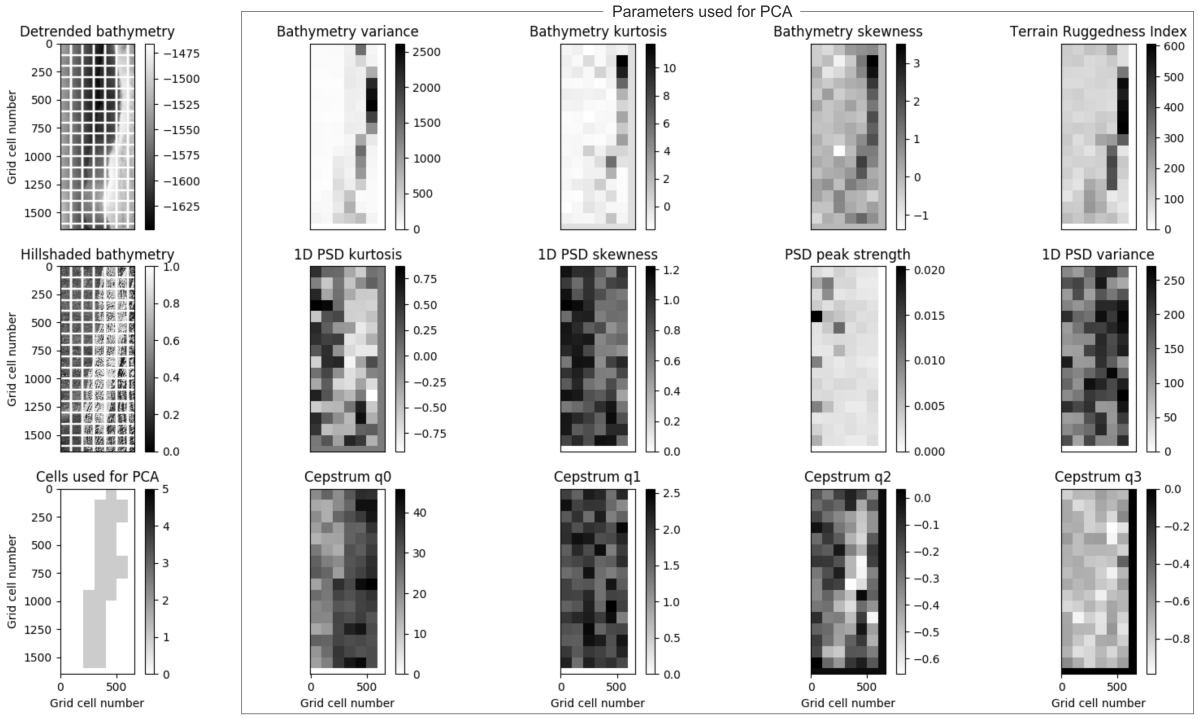

Figure 14: Statistical parameters extracted from the high-resolution version of the bathymetry and fourier analysis power spectrum of spreading ridges within the Tampen Slide headwall (Spreading Zone 1). Data courtesy of TGS.

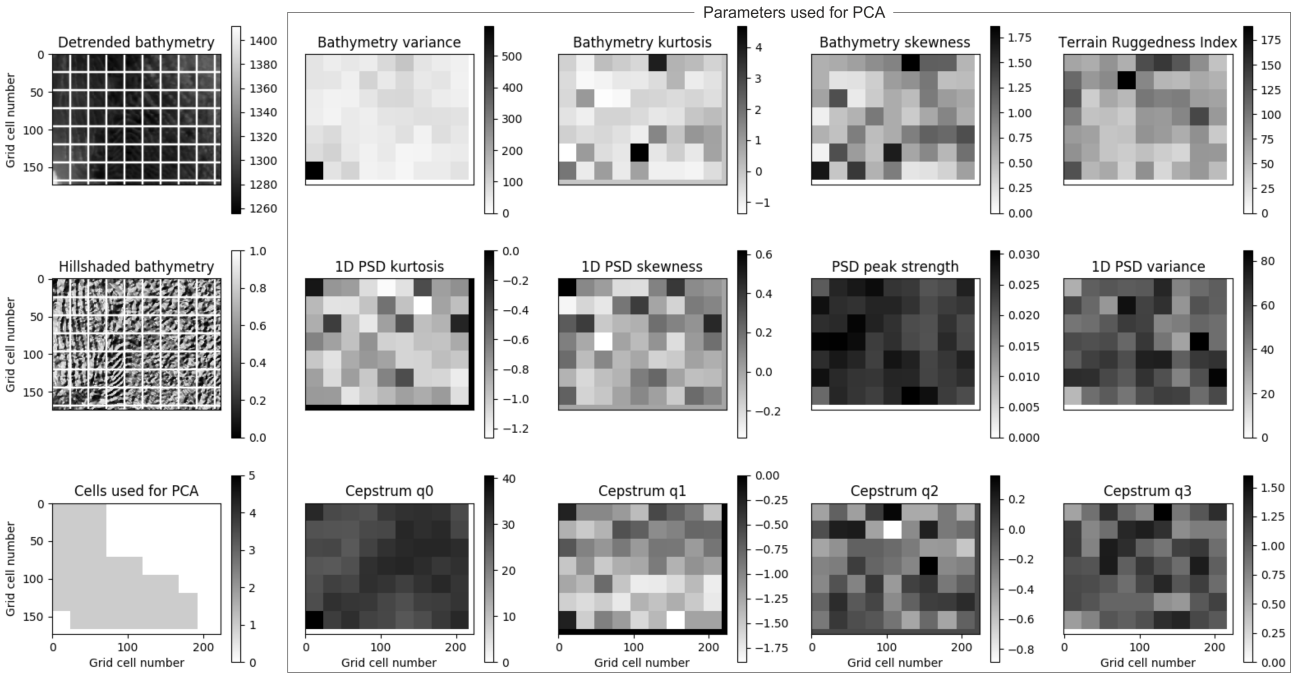

Figure 15: Statistical parameters extracted from the low-resolution version of the bathymetry and fourier analysis power spectrum of spreading ridges within the Tampen Slide headwall (Spreading Zone 2). Data courtesy of TGS.

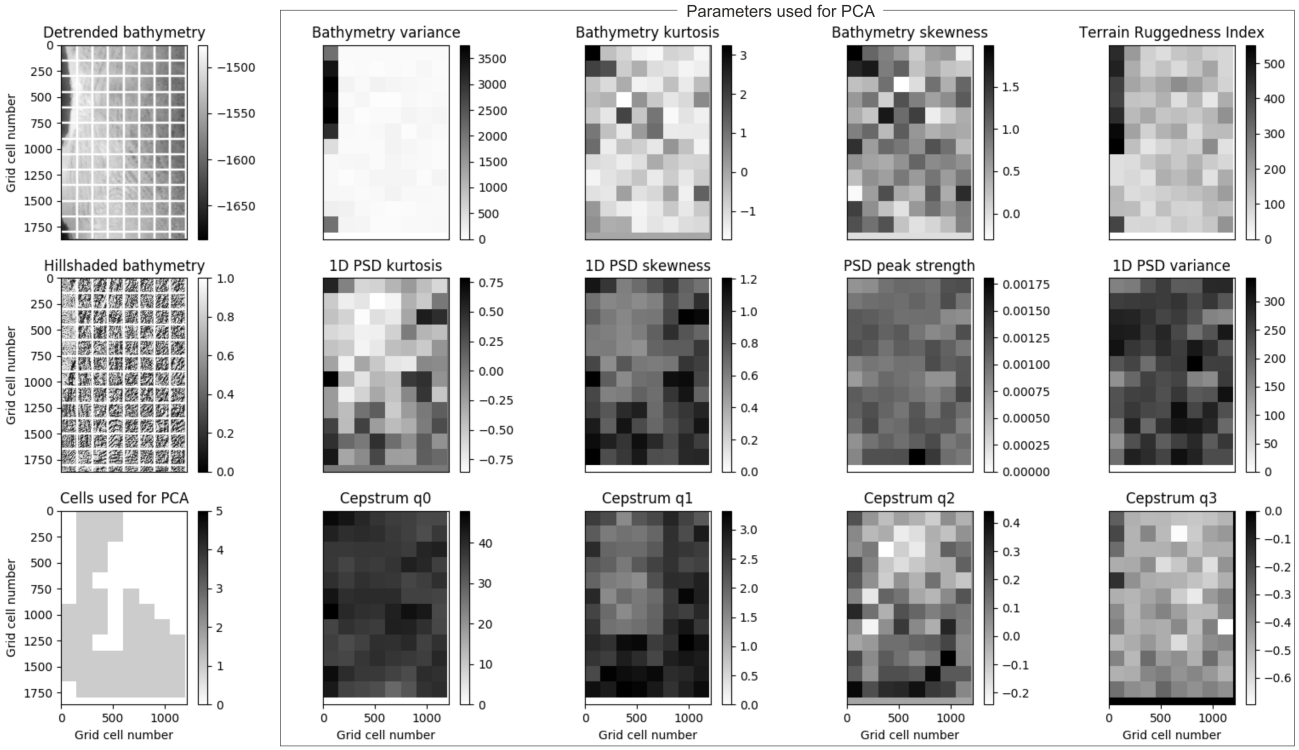

Figure 16: Statistical parameters extracted from the high-resolution version of the bathymetry and fourier analysis power spectrum of spreading ridges within the Tampen Slide headwall (Spreading Zone 2). Data courtesy of TGS.

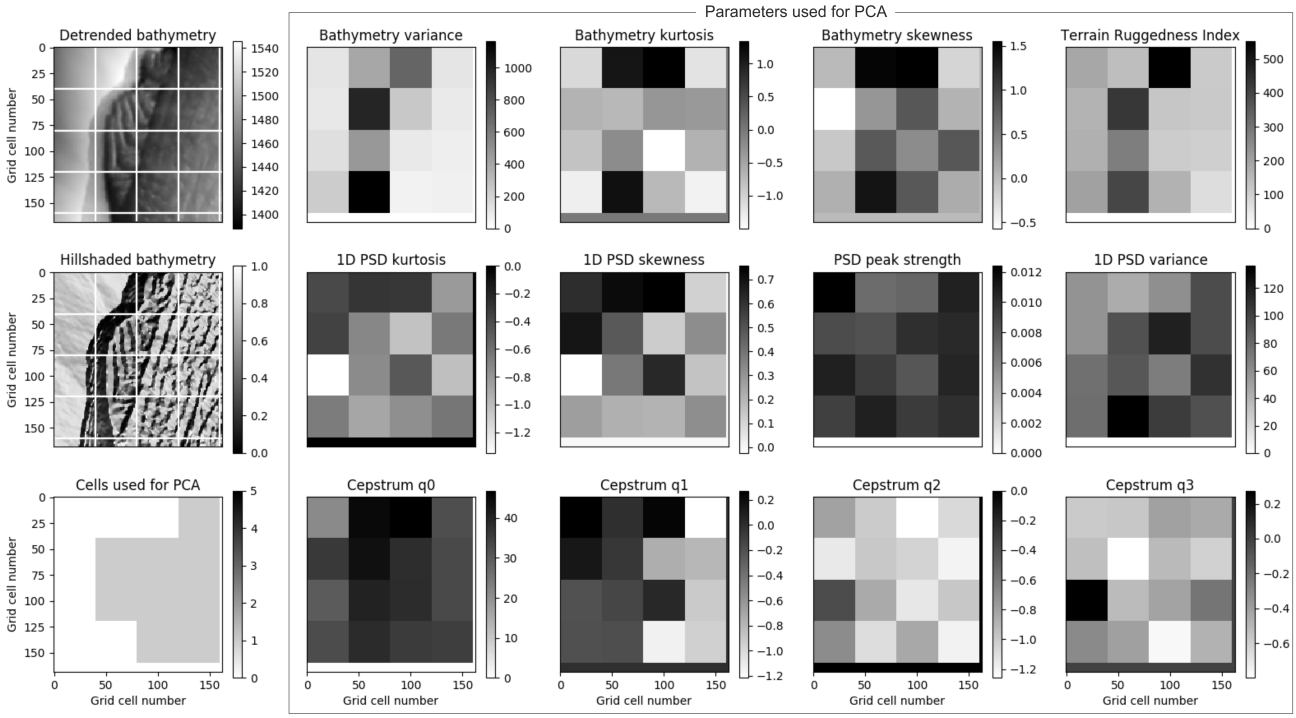

Figure 17: Statistical parameters extracted from the low-resolution version of the bathymetry and fourier analysis power spectrum of spreading ridges within the Tampen Slide headwall (Spreading Zone 3). Data courtesy of TGS.

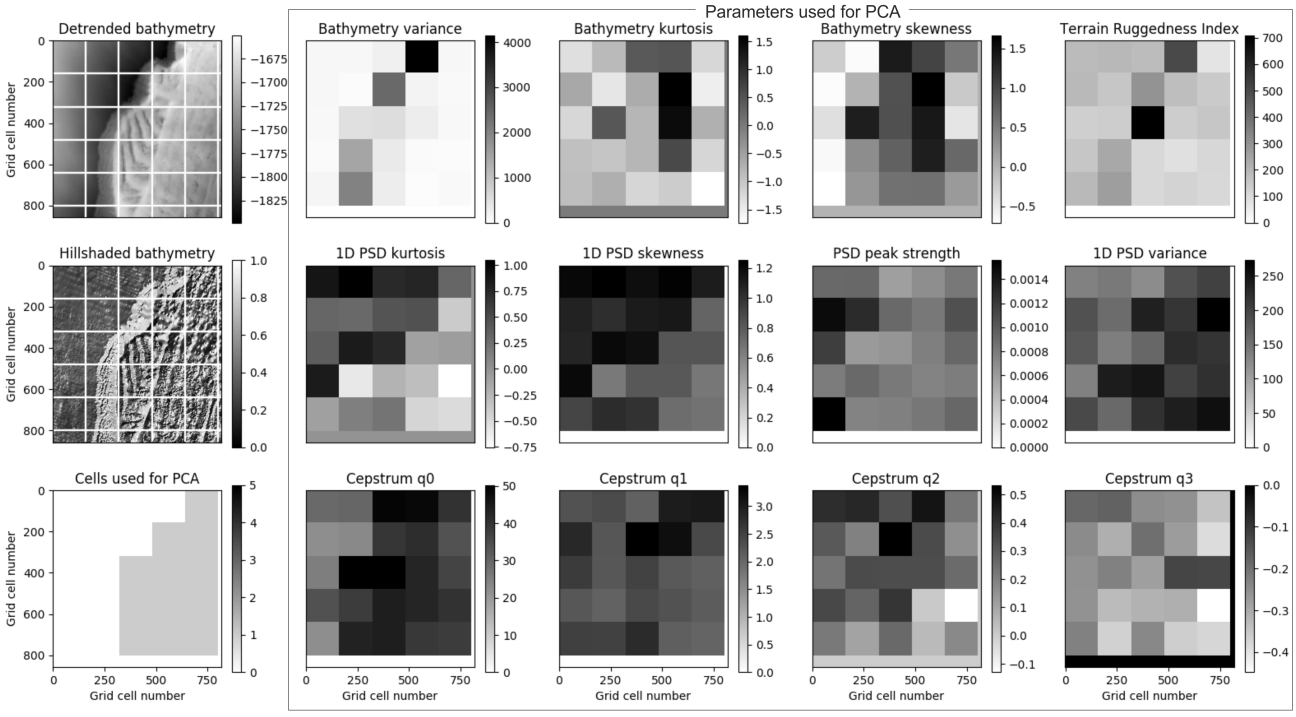

Figure 18: Statistical parameters extracted from the high-resolution version of the bathymetry and fourier analysis power spectrum of spreading ridges within the Tampen Slide headwall (Spreading Zone 3). Data courtesy of TGS.

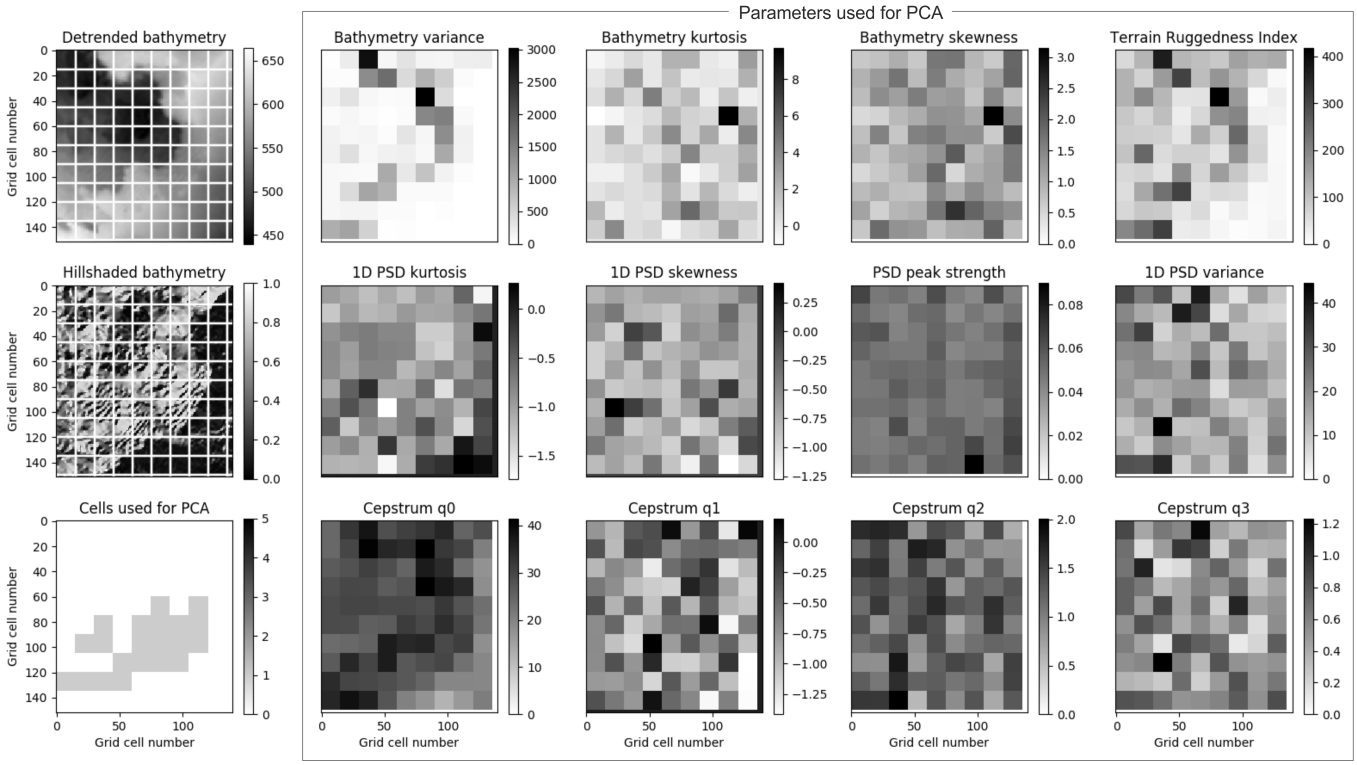

Figure 19: Statistical parameters extracted from the low-resolution version of the bathymetry and fourier analysis power spectrum of spreading ridges on the eastern side of the Tampen Slide headwall (Spreading Zone 4). Data courtesy of TGS.

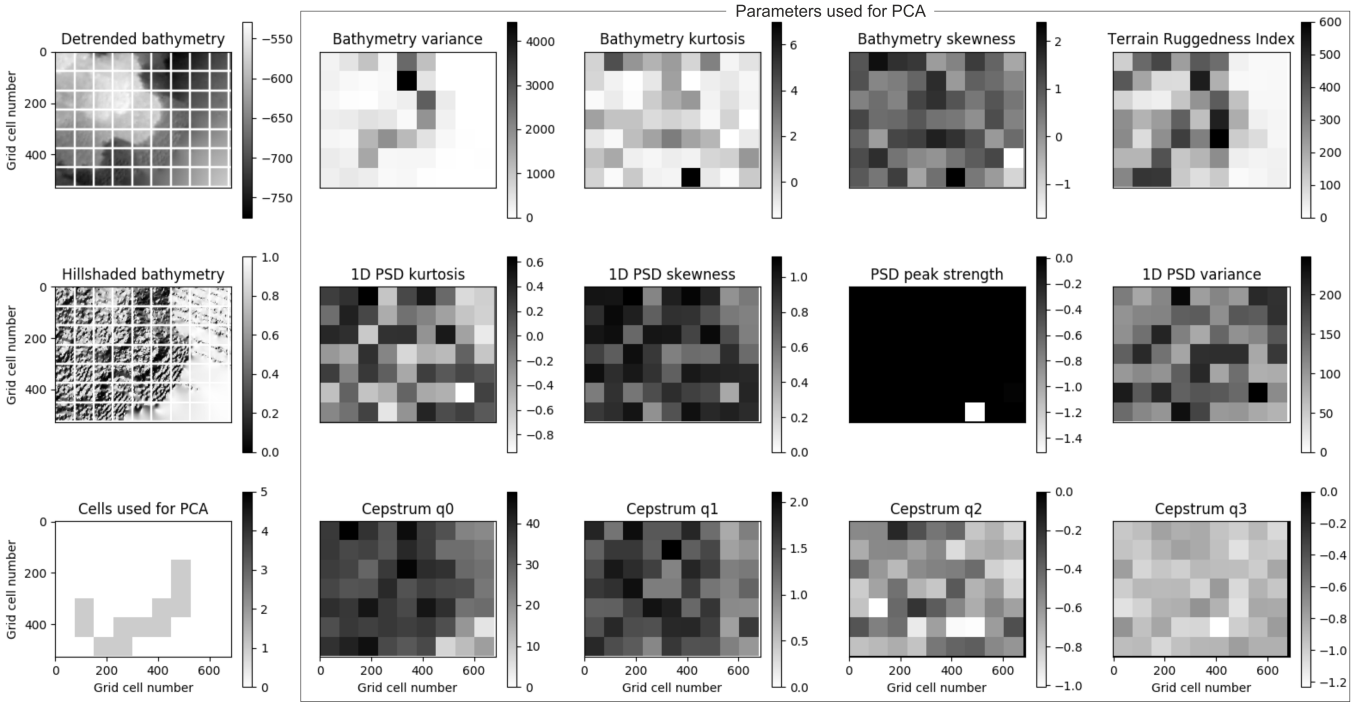

Figure 20: Statistical parameters extracted from the high-resolution version of the bathymetry and fourier analysis power spectrum of spreading ridges on the eastern side of the Tampen Slide headwall (Spreading Zone 4). Data courtesy of TGS.